TECHNISCHE UNIVERSITÄT MÜNCHEN

Professur für Hydromechanik

Single Pixel Particle Image Velocimetry for Measurements of Two-Dimensional Joint Velocity Distributions

Claudia Strobl

Vollständiger Abdruck der von der Ingenieurfakultät Bau Geo Umwelt der Technischen Universität zur Erlangung des akademischen Grades eines

Doktor-Ingenieurs

genehmigten Dissertation.

Vorsitzender:	Prof. Dr.-Ing. M. Disse
Prüfer der Dissertation:	
	1. Prof. Dr.-Ing. M. Manhart
	2. Prof. Dr. rer. nat. C.J. Kähler

Die Dissertation wurde am 07.03.2017 bei der Technischen Universität München eingereicht und durch die Ingenieurfakultät Bau Geo Umwelt am 25.07.2017 angenommen.

Abstract

To increase the spatial resolution of experimental measurements, a new method to approximate velocity joint probability density functions (JPDF) from single pixel ensemble correlation (SPE) functions is introduced. In contrast to the classical Particle Image Velocimetry (PIV) approach, which correlates subregions of a consecutive image pair, SPE determines an ensemble averaged correlation function at each pixel of the image. This increases the spatial resolution, however initially removes all time-dependent information. Since the JPDF of velocity is trapped in the correlation function by a convolution with the autocorrelation function, time-dependent velocity parameters, i.e. Reynolds stresses, which are represented by the JPDF variance, can be recovered only if the velocity JPDF can be retrieved from the correlation function.

This work demonstrates that the statistical moments of the velocity JPDF can be determined by a combination of the statistical moments of the correlation and the autocorrelation function. In contrast to the methods found in the literature the new method is able to approximate the statistical moments of velocity JPDFs of arbitrary shape and size. The capacities of the new method are analyzed using synthetic data. Furthermore, the method is applied to a PIV dataset of a flow in front of a cylinder mounted vertically on a flat plate. The comparison of the SPE results to a classical $16 \times 16\,px$ PIV evaluation and a Large Eddy Simulation of the same flow case reveal the high resolution capacities of the new method, especially in the near-wall region and the regions of the vortexes in front of the cylinder.

Zusammenfassung

Im Rahmen dieser Arbeit wird ein neues Verfahrung zur Approximation von Geschwindigkeitsverteilungsfunktionen (JPDF) aus Single-Pixel-Ensemble (SPE) Korrelationsfunktionen entwickelt. Im Gegensatz zur klassischen Particle-Image-Velocimetry (PIV) Auswertung, welche auf der Korrelation von Teilbereichen eines aufeinanderfolgenden Bildpaares basiert, werden im Rahmen der SPE-Auswertung einzelne Pixel des Bildpaares korreliert und über das Datenensemble gemittelt. Auf diese Weise wird die räumliche Auflösung deutlich erhöht, allerdings sind anfangs alle zeitabhängigen Informationen verloren. Da jedoch die JPDF in der Korrelationsfunktion enthalten ist - die Korrelationsfunktion kann als die Faltung der JPDF mit der Autokorrelationsfunktion beschrieben werden - können zeitabhängige Informationen, zum Beispiel die Reynoldsschen Spannungen aus der JPDF gewonnen werden, sofern diese rekonstruiert werden kann.

Die vorliegende Arbeit zeigt eine Methode auf, die die statistischen Momente der JPDF über eine Kombination der Momente der Korrelations- und Autokorrelationsfunktion bestimmt. Im Gegensatz zu den in der Literatur vorgestellten Verfahren, ist diese Methode dazu in der Lage die statistischen Parameter von JPDFs unabhängig derer Verteilungsform und Größe abzuschätzen. Die Eigenschaften der Methode werden mit Hilfe synthetischer Daten analysiert. Außerdem wird das Verfahren auf einen PIV Datensatz einer Strömung vor einem vertikalen Zylinder auf einer ebenen Platte angewandt. Die Ergebnisse werden mit einer klassischen $16 \times 16\,px$ PIV-Auswertung und den Ergebnissen einer Large Eddy Simulation des gleichen Strömungsfalls verglichen. Im Rahmen dessen wird der Detailreichtum des neuen Auswerteverfahrens insbesondere im wandnahen Bereich und im Bereich des Hufeisenwirbels deutlich.

Acknowledgments

My doctoral thesis would have never been finished or have even started without the support and care of many different persons. I want to use this page to thank at least some of them personally.

Thank you, Prof. Dr.-Ing. Michael Manhart, for your constant believe in my abilities, for always answering my questions, and for giving me the chance to do the research presented here. Furthermore, I have to thank you that you allowed me to do this at my own pace, such that I was able to also do some teaching and start the students lab, which I really enjoyed.

Thank you, Prof. Dr. Christian Kähler, for acting as the second referee and for the discussions I had with you and your group, which made me reconsider my thoughts and let me gain a deeper understanding of the topic.

Thank you, my dear colleagues, for the ideas we shared on so many different topics in the past few years. They all added an extra bit to my knowledge. In particular I want to thank Ulrich Jenssen and Wolfgang Schanderl for the discussions we had on flow structures in front of the vertical cylinder, for providing data I could compare my results to, and for proof-reading a draft of this work.

Here, I also want to thank Dr Stephen Starck from the TUM Language Center for his support to improve my written English and for removing all my German commas in front of the word *that*.

Thank you, Isabella Schmidt, for helping me with the figures, the first figure would have never been there without you.

And finally, thank you, my dear family, especially my parents and Johannes Strobl, for your never ending support, love and care.

Contents

List of Tables

List of Figures

Nomenclature

List of Latin Symbols

A	cross-section of a flume.
$A(\mathbf{x})$	autocorrelation function.
D	diameter of the cylinder.
D_a	diameter of aperture.
F_{drag}	drag force.
$F_{inertia}$	inertia force.
$I_1(\mathbf{x})$, $I_2(\mathbf{x})$	image intensity matrix of either the first I_1 or the second I_2 image of a consecutive image pair.
$I(\mathbf{x})$	intensity matrix of an image of particles.
$I_{PSF}(\mathbf{x})$	point spread function of the aperture.
$I_{part}(\mathbf{x})$	intensity matrix of a single particle.
M_{lens}	magnification factor.
N_{images}	number of images a dataset consists of.
N_{ppp}	seeding density in particles per pixel.
$N_{samples}$	number of samples, either in time or space.
N_s	source density in particles per pixel.
Q	flow rate.
$R(\mathbf{r})$	correlation function.
$R_C(\mathbf{r})$	correlation of the mean intensities.
$R_D(\mathbf{r})$	correlation of the fluctuations of both images.
Re	Reynolds number $Re = \frac{vD}{\nu_{fluid}}$.
$R_F(\mathbf{r})$	correlation of a fluctuating part of one image and the mean of the other.
St	Stokes number $St = \frac{t_r}{t_\eta}$.
$W(\mathbf{x})$	matrix of particle positions.
$\mathbf{a}$	acceleration vector of a particle $\mathbf{a} = \frac{d\mathbf{v}_{part}}{dt}$.
a	arbitrary variable.
c_f	friction coefficient.
$\mathbf{d}$	displacement vector.
$d_v(\mathbf{x}, t)$	function describing the displacement between the first and the second image $d(\mathbf{x}) = \mathbf{x} + \mathbf{d}(\mathbf{x}, t)$.
d_{beam}	diameter of laser beam.
d_e	effective particle image diameter.

$d_{e,corrected}$	corrected effective particle image diameter.
d_{geom}	diameter of the particle image due to magnification by the optical system.
d_{part}	physical diameter of a particle.
d_s	diffraction limited diameter of a particle image.
$f'(\mathbf{v};\mathbf{x})$	fine grained probability density function of the velocity.
$f(\mathbf{v};\mathbf{x})$	probability density function of the velocity.
$f(a;\mathbf{x})$	probability density function of an arbitrary parameter a.
f	focal length.
$f^{\#}$	aperture number $f^{\#} = \frac{f}{D_a}$.
r_{XY}	correlation coefficient of two random variables X and Y.
t	time.
t_η	Kolmogorov time scale.
t_r	particle relaxation time.
u	velocity component in streamwise direction.
u_{bulk}	bulk velocity $u_{bulk} = \frac{Q}{A}$.
u_τ	friction velocity.
$\mathbf{v}$	velocity vector.
v	velocity in general and velocity component in wall-normal direction.
v_{part}	velocity of a particle.
x	streamwise coordinate.
$\mathbf{x}_{part}$	position vector of a particle in space.
y	water level and wall-normal coordinate.
z_1	distance between the object plane and the focal lens.
z_2	distance between the focal lens and the image plane.
z_r	Rayleigh length.

List of Greek Symbols

Δt	time between two recordings.
Δx, Δy	spatial resolution of a pixel grid.
Δz	depth of the light sheet.
$\alpha(\mathbf{s})$	Fourier transformed autocorrelation function $A(\mathbf{x})$.
$\delta(a-b)$	Dirac delta function.
δ_v	Dirac delta function including the displacement function $d_v(\mathbf{x},t)$.
δ_ν	inner length scale.
δ_t	exposure time of the camera sensor to light.
ϵ_{abs}	absolute error.
ϵ	dissipation rate.
$\phi(\mathbf{s})$	Fourier transformed velocity JPDF.
κ	flatness/kurtosis.

λ	wavelength of laser light.
μ	mean value.
μ_{fluid}	dynamic viscosity of a fluid.
ν	skewness.
ν_{fluid}	kinematic viscosity of a fluid.
ρ	density of the fluid.
ρ_{part}	density of the particles.
σ	standard deviation.
σ^2	variance.
τ_w	wall-shear stress.
$\xi(\mathbf{s})$	characteristic function of a probability distribution.

List of Mathematical Operators

$X^\star$	complex conjugate of function X.
$*$	convolution operator.
$\star$	cross-correlation operator.
$\langle X \rangle$	ensemble averaged mean value of random variable X $\langle X \rangle = \frac{1}{N_{samples}} \sum_{i=1}^{N_{samples}} (X)_i$.
M^k	k-th raw moment.
m^k	k-th central moment.
$\mathring{m}^k$	k-th normalized central moment.
X'	fluctuation part of random variable X $X' = X_i - \langle X \rangle$.
$\tilde{X}$	Fourier transform of function X.

Acronyms

CCD	Charge Coupled Device.
CMOS	Complementary Metal Oxide Semiconductor.
FOV	Field of View.
JPDF	Joint Probability Density Function.
LDA	Laser Doppler Anemometry.
LES	Large Eddy Simulation.
PDF	Probability Density Function.
PIV	Particle Image Velocimetry.
PSF	Point Spread Function.
PTV	Particle Tracking Velocimetry.
RMSD	Root Mean Square Deviation.
sCMOS	Scientific Complementary Metal Oxide Semiconductor.
SPE	Single Pixel Ensemble Correlation.

1 Introduction

Humans tend to strive for a deeper understanding of their surroundings. We all once threw a stick into a creek and watched it float away. Some of us might have even measured the time it took the stick to pass under a bridge and determined the floating velocity to estimate how long it would take the stick to reach the next town, the next larger river, and so on. Thus, it is natural for us to apply measurement techniques to describe our surroundings.

One state of the art measurement technique to determine instantaneous flow fields non-intrusively is Particle Image Velocimetry (PIV). The technique utilizes the correlation of two subsequent images of particles moving in a flow field to estimate the mean displacement of the particles within the recording time of the two images. Assuming that the particles perfectly follow the fluid's motion, their velocities describe the velocity of the fluid. In standard systems a thin plane within the flow field is illuminated by a laser beam, the light sheet, such that on the images only particles within this thin plane are visible, and the velocities for that measurement plane can be estimated.

The correlation of subregions of an image of particles results in a velocity vector, which describes the spatial average of the particle motion in this subregion. As a number of particles within the correlated regions is needed to gain reliable results, the smallest distance between the resulting velocity vectors is in the range of 8 to 16 pixels, such that the spatial resolution of an image is never fully restored. Therefore, small details of the flow structures are often lost or cannot be measured, e.g. close to walls. Single Pixel Ensemble Correlation (SPE), an extension of PIV, increases the spatial resolution to a single pixel. As SPE evaluates time-averaged correlation functions all instantaneous information is initially lost. In this work and extension of the SPE evaluation routine is presented, such that not only time-averaged mean velocities can be determined but also Reynolds stresses and higher order moments.

In the next section the historical development of PIV and the path that led to SPE are described. Then the drawbacks of the state of the art SPE evaluation routines to determine flow parameters beyond mean velocities are discussed and the contributions of this work are addressed.

1.1 Development of Particle Image Velocimetry

Since its introduction in the 1980s, PIV has developed rapidly and is now the state of the art technique when two- or even three-dimensional flow fields need to be measured. The main advantages of the PIV technique over other measurement techniques are that the method is non-intrusive and returns instantaneous flow fields. This makes it easy to access two- or three-dimensional flow structures and to compare the outcomes to numerical results, which are also usually two- or three-dimensional fields. Two drawbacks of PIV are that the technique is restricted in the measurement frequency due to the equipment used and that it is an indirect measurement technique, which measures the velocity of particles in the fluid, and therefore relies on the capacity of the particles to resemble the fluid's motion.

The general principle of PIV can be explained as follows: particles, which act as markers of a fluid's motion, are illuminated for short instances of time by laser light. To freeze the motion an image is recorded during the illumination and stored for further processing. In general a consecutive image pair is recorded at a known time delay Δt. In the classical approach the images are then divided into subregions, so-called interrogation windows, which are then correlated. The position of the correlation peak indicates the most probable mean displacement of all particles inside of the evaluated subregion within the time delay Δt (Adrian, 1991). To be able to distinguish the correlation peak from surrounding noise, the interrogation window has to be sufficiently large to contain at least seven particle images (Keane and Adrian, 1990, 1992). The usual size of an interrogation window lies in the range of $32 \times 32 - 16 \times 16\,px$. Assuming an image of $2048 \times 2048\,px$, this results in $64 \times 64 - 128 \times 128$ velocity vectors.

The spatial position of the correlation peak can be transformed into a velocity vector, because the time delay and the scale of one pixel are known. To increase the accuracy to sub-pixel values, usually a function, often a Gaussian curve, is fitted into the correlation peak (Raffel et al., 2007, Adrian and Westerweel, 2010). The Reynolds stresses of the flow can be determined after a set of image pairs has been evaluated in this manner. Therefore, the mean and fluctuating components of the velocity are determined once the velocity fields have been filtered and spurious vectors have been removed (Raffel et al., 2007, Adrian and Westerweel, 2010).

Due to the spatial averaging effect of the interrogation window cross-correlation, there is a large loss in spatial resolution. Considering again the examples from above, an image of $2048 \times 2048\,px$ results at best in 128×128 velocity vectors, so the spatial resolution is 16 times lower than the input data. This can be problematic for two reasons: first of all, there is a lack of detail since the information is filtered by the interrogation window, such that structures smaller than the interrogation window are neglected. Second, in regions of strong gradients, a velocity gradient crosses the interrogation window and smears the correlation peak, which makes it difficult to detect and results in biased velocity values (Keane and Adrian, 1990). However, especially in complex turbulent flows, close to boundaries and in vortexes, these phenomena occur and need to be resolved as experimental data is often used to validate or improve numerical methods.

Two techniques have been developed in the past few years to overcome this problem: Single Pixel Ensemble Correlation (SPE) and Particle Tracking Velocimetry (PTV). While PTV tracks the motion of single particles between consecutive recordings, SPE follows up the classic PIV evaluation routine but reduces the interrogation window size to one pixel and averages the ensemble of all correlation functions of the time series. SPE is based on the ensemble correlation method introduced by Meinhart et al. (2000), who suggested ensemble averaging before determining the peak's location as it increases the Signal-To-Noise (SNR) ratio of correlation functions. Westerweel et al. (2004) were the first to use this technique to increase the spatial resolution to a single pixel in a micro-PIV set-up of a stationary laminar flow. Afterwards Wereley et al. (2005a) also applied this technique to a micro-PIV set-up and performed a study on bias and random errors of this method (Wereley et al., 2005b).

Although it was first thought that SPE is only applicable to laminar flows due to time-averaging, Kähler et al. (2006) showed, applying the method to a fully turbulent flow above an airfoil, that the mean velocity of an unsteady turbulent flow can also be resolved at a high spatial resolution, especially close to the boundary. To determine time-dependent flow parameters, e.g. Reynolds stresses, the correlation function has to be scrutinized. According to several authors, Adrian (1988), Westerweel (1993), Adrian (1994), Soria and Willert (2012), the Joint Probability Density Function (JPDF) of the velocity is trapped within the correlation function. It is stored there by a convolution with the autocorrelation function of the images. Therefore, techniques are needed to recover the velocity JPDF from the correlation function.

Following up a publication of Kähler and Scholz (2006), Scharnowski et al. (2012) proposed fitting two-dimensional Gaussian curves into the correlation and autocorrelation functions to determine the width of the JPDF and thus the Reynolds stresses. This method has been used by several researchers e.g. Scharnowski et al. (2012), Kähler et al. (2012b), Huisman et al. (2013) and Karchevskiy et al. (2015) to determine Reynolds stresses at single pixel resolution, although it is only able to recover the parameters of Gaussian shaped JPDFs. Thus, Scharnowski and Kähler (2013) introduced a second method to determine the velocity JPDF using an iterative deconvolution of the correlation function by the autocorrelation function. In contrast to the Gaussian fit, this method is independent of the shape of the distribution function, but depends on the smoothness of the functions. Therefore, Scharnowski and Kähler (2013) had to use $8 \times 8\,px$ ensemble averaged correlation functions to evaluate a flow over periodically arranged hills. Avallone et al. (2015) applied this method to determine Reynolds stresses in an upward directed jet at single pixel accuracy using an algorithm, which increases the number of samples contributing to the correlation functions by symmetric double correlation.

1.2 Motivation

Both methods mentioned in the previous section to determine the velocity JPDF entrapped in the correlation function are accompanied by severe problems:

The first method, fitting a two-dimensional Gaussian curve into the correlation and autocorrelation function, is only able to recover Gaussian shaped functions. If a gradient occurs, such that the correlation peak is stretched and rotated, a correction when determining the Reynolds stresses needs to be applied. Skewed or bimodal velocity distributions cannot be resolved without changing the fitting function. Furthermore, artificial turbulence occurs at turbulence levels below $0.25\,px$ (Scharnowski et al., 2012).

The second method, deconvolving the correlation function using the autocorrelation function, requires an iterative procedure as direct deconvolution is not possible due to the noise contained in the correlation function (Starck et al., 2002). Scharnowski and Kähler (2013) identify three restrictions for the use of this method: (1) sufficiently smooth correlation and autocorrelation functions; (2) identical window weighing function for the calculation of the correlation and autocorrelation function; (3) a correlation plane large enough to cover the full correlation function. While the latter two can be provided, the question arises what is a sufficiently smooth correlation function? Furthermore, deconvolution is unable to resolve a signal at a resolution higher than the input signals, such that velocity JPDFs narrower than a pixel cannot be resolved well.

1.3 Contributions

The aim of this work is to introduce a method that overcomes the problems of the two methods discussed above. This method is based on the fact that the statistical moments of a function, which is the result of the convolution of two other functions, can be calculated using the statistical moments of the functions convolved. The principle can also be flipped, such that the statistical moments of the correlation and autocorrelation functions can be used to determine the moments of the velocity JPDF. Due to this simple mathematical principle, the statistics of any velocity JPDF can be restored independently of the size and shape of the distribution function.

Furthermore, as statistical moments of a distribution function are determined by integration, methods to pre-process the correlation functions to reduce the influence of noise are discussed and tested. This improves not only the method developed within this work but also the deconvolution method described above. In the application chapter the new method is applied to a PIV dataset of a highly turbulent flow in front of a vertical cylinder mounted on a flat plate. There the results of the SPE evaluation are compared to results of a classical PIV evaluation and a Large Eddy Simulation (LES), revealing the advantages of the new high resolution evaluation technique.

1.4 Overview

The rest of this work consists of five more chapters: Chapter 2 provides an overview of the PIV method, its general working principle and the evaluation strategies that led to SPE; Chapter 3 describes PIV in a mathematical sense and develops the new method.

In Chapter 4 the method is tested on synthetic datasets and compared to two methods found in the literature. Chapter 5 discusses the results of the application of the new SPE evaluation routine on a PIV dataset of a flow field in front of a vertical cylinder. The flow case is characterized by differently shaped velocity distributions and a large dynamic range. The final chapter summarizes this work and presents a brief description of prospective research.

2 Basics of Particle Image Velocimetry

Particle Image Velocimetry (PIV) is a non-intrusive measurement technique that is able to determine two- or even three-dimensional instantaneous velocity fields. It uses tracer particles, added to a flow and illuminated for a short period of time, as markers of a fluid's motion. To determine the velocity field, images of illuminated particles in the flow are recorded, and a correlation of a consecutive image pair of known time difference is performed. The mean displacement of the particles then corresponds to the position of the correlation peak, which can be transformed into a velocity vector, since the time delay as well as the spatial resolution of the image are known.

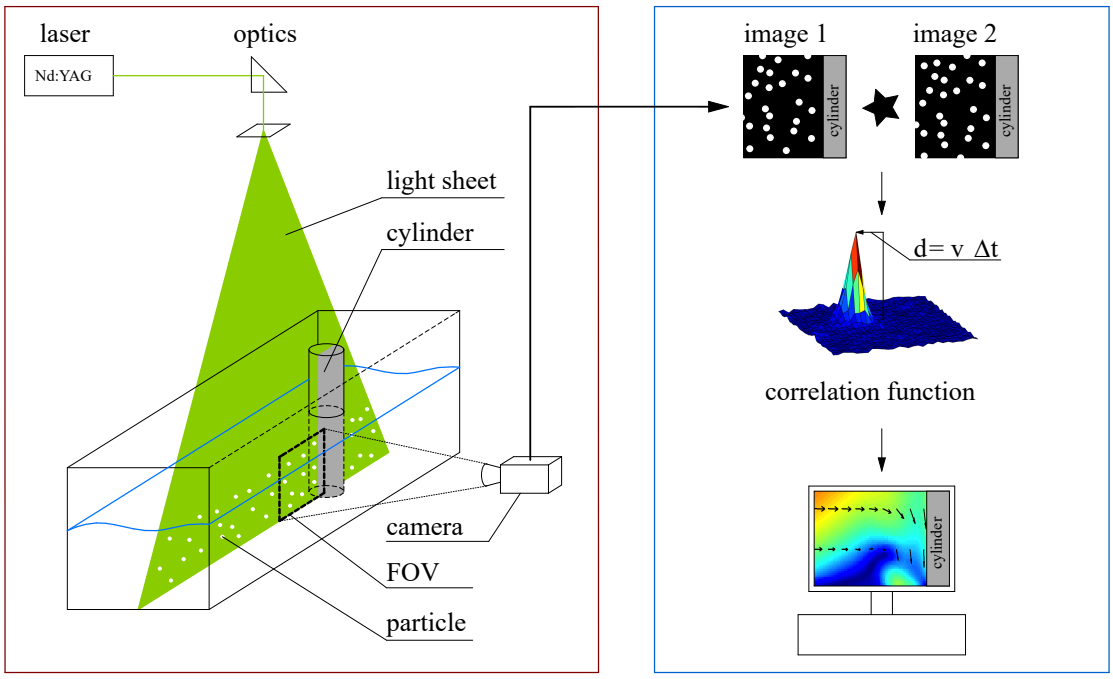

Figure 2.1: Basic PIV set-up and components.

Fig. 2.1 shows a simplified model of a PIV measurement set-up installed at a flow around a vertical cylinder. The basic components are: seeding particles, a light source to illuminate the scene, a camera to record the images and a computer program with algorithms to evaluate particle images. These components can be assigned to two working steps:

1. Image Acquisition (red rectangle in Fig. 2.1);
2. Image Evaluation (blue rectangle in Fig. 2.1).

In the following both steps are discussed. First the focus lays on the interaction and the properties of the physical components of the measurement set-up, then the underlying eval-

uation strategies are described. In this part the basics of PIV data evaluation and two techniques, which led to Single Pixel Ensemble Correlation (SPE) are explained and then the SPE technique is discussed.

2.1 Image Acquisition

The elementary components of PIV are photographs of particles, which I will refer to as images of particles in the following. The recording of the images consists of several steps:

1. The fluid is seeded using particles, which act as markers of the fluid's motion;
2. A light source illuminates a certain region of the fluid to make the particles visible;
3. An optical system focuses the illuminated region onto the imaging material, such that a sharp image can be recorded;
4. A camera records the illuminated scene and stores this information on a photograph.

Each of these steps influences the final quality of a PIV dataset. Therefore, the main characteristics of each are explained in the next paragraphs.

2.1.1 Seeding Particles

The seeding particles added to the flow and used as markers of fluid's motion have to fulfill two main conditions:

- They have to scatter light, such that the contrast in the image is sufficiently large and the particles are clearly distinguishable from their surrounding;
- They have to follow the flow as if they were the fluid itself to accurately represent the fluid's motion.

Scattering Properties

The scattering properties of particles define the amount of light available for an image recording and therefore the amount of contrast possible. The scattering depends on the particle size d_{part} the wavelength of the illuminating light λ and the observation position. The scattering furthermore depends on the ratio between the refractive indexes of the particles and the fluid. A large ratio between the refractive indexes results in stronger reflections and thus a greater visibility[1].

The intensity of scattered light also differs with respect to the angle between the incoming light and the observation position. According to Mie's scattering theory, there are several maxima and minima of scattered light intensities around a reflecting sphere. They depend on the size of the particle d_{part} and the wavelength of the illuminating light λ (Adrian and Westerweel, 2010, Raffel et al., 2007, Tropea et al., 2007). The largest intensity maximum is reached on the opposite side of the light source. Eventually, this position is rarely possible

[1]The opposite effect, refractive index matching, is sometimes used when the flow around an obstacle is studied. Here the ratio between the material of the obstacle and the fluid is kept small, as the object will reflect less or even no light (Hassan and Dominguez-Ontiveros, 2008)

for PIV measurements, where usually the light source and the observation position are at right angles to each other, such that the scattered light intensity is lower. Thus, particularly if the ratio between the refractive indexes is also low, this results in the need of a higher intensity of the incoming light or the usage of larger particles. As the particle size has to be kept within a certain limit, see the following paragraph, this is one reason why commonly laser light is used as light source.

Particle Dynamics

The ability of a particle to follow a fluid's motion depends on the density ratio between fluid and particle, the size of the particle, the viscosity of the fluid and the characteristics of the flow. The characteristics of the flow describe the scales appearing in the examined flow situation: large scales, which are the governing scales of the flow, e.g. the height of the channel, the diameter of the obstacle, and small scales, which are, according to Kolmogorov's similarity hypothesis, only influenced by the viscosity of the fluid ν_{fluid} and the dissipation rate ϵ (Frisch, 1995). A particle, which is supposed to accurately represent a fluid's motion, has to be sufficiently small to track these small scale motions. This capacity is described by the Stokes number, Eq. (2.1), the ratio between the particle relaxation time t_r and the Kolmogorov time scale t_η.

$$St = \frac{t_r}{t_\eta} \tag{2.1}$$

While the Kolmogorov time scale, Eq. (2.2), solely depends on the fluid's viscosity ν_{fluid} and the dissipation rate ϵ, the relaxation time t_r depends on the forces acting on the particle and describes its ability to react on velocity changes in the flow.

$$t_\eta = \left(\frac{\nu_{fluid}}{\epsilon}\right)^{1/2} \tag{2.2}$$

The main forces acting on a particle in a fluid are drag F_{drag} and inertia $F_{inertia}$. Assuming the particle as a perfect sphere, the drag force at a small particle based Reynolds number can be described by the following equation,

$$F_{drag} = 3\pi\mu_{fluid} d_{part} \phi \left(\mathbf{v}_{part} - \mathbf{v}\right) \tag{2.3}$$

with μ_{fluid} being the dynamic viscosity of the fluid, d_{part} the physical diameter of the particle, and $\mathbf{v}_{part} - \mathbf{v}$ the velocity difference between the particle and the fluid (Adrian and Westerweel, 2010). A factor $\phi = 1$ sets Eq. (2.3) equal to Stokes's law, which describes the drag on a motionless solid sphere in a steady flow at a low particle based Reynolds number $Re_{part} = \frac{d_{part}|\mathbf{v}_{part}-\mathbf{v}|}{\nu_{fluid}}$. Values of $\phi > 1$ account for the drag increase if the flow surrounding the particle is unsteady and the particle based Reynolds number is larger (Clift et al., 2005).

The inertia force is defined as

$$F_{inertia} = \frac{1}{6}\pi d_{part}^3 \mathbf{a} \left(\rho_{part} - \rho\right) \tag{2.4}$$

with the acceleration of the particle $\mathbf{a} = \frac{d\mathbf{v}_{part}}{dt}$ and the density difference between particle and fluid $\rho_{part} - \rho$ (Clift et al., 2005).

To estimate the velocity lag between the particle and the surrounding fluid, assuming a constant acceleration of the fluid $\mathbf{a}$, Eq. (2.3) and Eq. (2.4) can be set equal, and solved for the velocity difference $\mathbf{v}_{part} - \mathbf{v}$.

$$\mathbf{v}_{slip} = d_{part}^2 \frac{\rho_{part} - \rho}{18\mu_{fluid}} \mathbf{a} \tag{2.5}$$

Eq. (2.5) can be transformed into a time scale, the particles relaxation time, t_r (Raffel et al., 2007, Adrian and Westerweel, 2010).

$$t_r = \frac{\rho_{part}}{\rho} \frac{d_{part}^2}{18\nu_{fluid}} \tag{2.6}$$

To ensure small relaxation times and therefore a good following behavior a particle needs to be small with a density close to the fluid's density. On the other hand, the second property a particle has to fulfill - the light scattering - strongly reduces with the size of the particle, as introduced in the paragraph above. So a trade-off between these two properties has to be made, considering the flow examined, the available light source and the capacities of the camera used. A list of different seeding particles and their properties can be found in Raffel et al. (2007), Adrian and Westerweel (2010). The optimal range of the particle image diameter for PIV evaluations was found to be in the range of 2-3 pixels (Prasad et al., 1992, Westerweel et al., 1997).

2.1.2 Illumination

In order to make the particles visible in a thin measurement plane the flow is illuminated by a light source, which is formed into a thin sheet of light using a set of lenses (cf. Fig. 2.1). The light source used is usually monochromatic laser light, often produced by a dual cavity ND:YAG laser[2] (Adrian and Westerweel, 2010). Laser light is the preferred light source due to its high energy density and the compact light beam emitted, which can easily be formed into a thin light sheet.

ND:YAG lasers

ND:YAG lasers are pulsed solid state lasers with an emitting wavelength of $\lambda = 1064\,nm$, corresponding to infrared light. As this wavelength is not visible to human eye, and is highly absorbed by water, the wavelength is shifted to green light[3] with a wavelength of $\lambda = 532\,nm$ using a non-linear optical crystal. The energy of a pulse of a current ND:YAG laser is in the range of 20 to $400\,mJ$, such that it harms skin and eye retina (Adrian and Westerweel,

[2]ND:YAG stands for neodymium-doped yttrium aluminum garnet.

[3]The green color has an additional, positive effect as many monochromatic camera sensors are the most sensitive in the range of green light (Raffel et al., 2007).

2010). ND:YAG lasers are therefore classified in the highest laser safety class - class 4.

The energy emitted in a laser pulse is created during the so called pumping process of one of the two laser cavities. This process employs the fact that atoms of certain materials can be stimulated to emit photons by raising their energy level. As the amplification of the energy level takes a certain amount of time, dual cavity lasers are built. They consist of two laser cavities, which are pumped separately, such that almost any user-defined time delay between two light pulses is possible. The time duration between two light pulses of a dual cavity ND:YAG laser is in the range of 0.005 to 0.001 μs (Adrian and Westerweel, 2010).

Light Sheet

The light sheet defines a measurement plane, or better to say a measurement volume, since it has a finite thickness Δz (cf. Fig. 2.2). This thickness is to be kept small, to reduce ambiguities caused by particles moving perpendicular to the light sheet, since this motion cannot be resolved. Therefore, the thickness of a light sheet is in the range of mm or even below. It is formed by a cylindrical lens, which expands the laser beam in one direction, to result in a triangular sheet of light and a focal lens, which focuses the light in the other direction, such that the sheet of light is thin.

When dealing with the properties of a light sheet, one has to consider that the light intensity is not uniform across the laser beam's cross-section, but follows a Gaussian distribution, whose diameter increases as the beam propagates. For every propagation distance z_r, Eq. (2.7), the diameter of the beam increases by $\sqrt{2}$. The distance z_r is called Rayleigh length and often referred to as the characteristic length scale of the laser beam (Löffler-Mang, 2012).

$$z_r = \frac{\pi d_{beam}^2}{\lambda} \tag{2.7}$$

Assuming a 532 nm-laser beam with an original diameter of $d_{beam} = 5\,mm$, the beam diameter increases to $\sqrt{2} \cdot d_{beam} = 7.07\,mm$ over a distance of $z_r = 147\,m$. This is negligibly small assuming a Field of View (FOV) in the range of dm, but it becomes problematic if the diameter of the laser beam, or the corresponding thickness of the light sheet, is reduced, as the Rayleigh length is proportional to the square of the beam diameter, Eq. (2.7), and a motion of particles perpendicular to the light sheet cannot be resolved. Further details on the effects of a not constant or too wide light sheet on the measurement results can be found e.g. in Raffel et al. (2007), Adrian and Westerweel (2010).

2.1.3 Mapping an Object onto an Image

The illuminated scene of particles is stored in an image for further processing. To explain this mapping process several terms have to be defined. In Fig. 2.2 a basic imaging system is shown, assuming that the media on both sides of the imaging lens are the same.

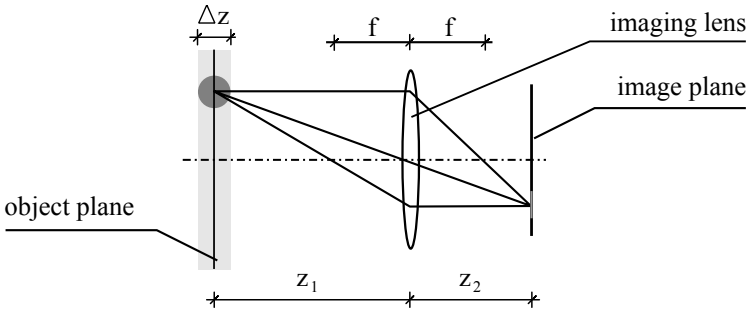

Figure 2.2: Basic imaging system

Starting from the left to the right, the object plane, the imaging lens and the image plane can be defined. The object plane and the light sheet usually form one plane, such that all particles in the light sheet are mapped via the imaging lens as focused particle images onto the image plane. The ratio between the distance of the object plane to the lens z_1 and the distance between the lens and the image plane z_2 defines the magnification factor M_{lens}.

$$M_{lens} = \frac{z_2}{z_1} \tag{2.8}$$

2.1.4 Cameras and Digital Images

To store images of particles for future evaluation they are recorded onto an image medium. In the early times of PIV this was photographic film material, today images are recorded by a digital camera sensor, either a Charge Coupled Device (CCD)- or a Complementary Metal Oxide Semiconductor (CMOS)-chip array. A PIV camera has to fulfill several criteria: (1) Record two images within a short time interval Δt; (2) at a short exposure time δ_t to freeze the motion at (3) a high spatial resolution Δx and (4) a low noise level.

The two digital camera sensors, CCD and CMOS, are either able to record in very short time intervals or at high spatial resolution. While the size of a CCD-chip, $\approx 6\,\mu m^2$, is about half the size of a CMOS-chip, the number of frames that can be recorded in one second by CMOS sensors is much larger (several kHz) than of CCD sensors (several Hz) (Hain et al., 2007). In the last years a new type of digital camera sensor has been developed the scientific CMOS sensor (sCMOS). This chip has about the same size as a CCD-chip, but is able to record at $30 - 100$ frames per second. In the next paragraph the basic principle of a CCD camera is explained, as the dataset analyzed in Chapter 5 was recorded by such a camera.

Principle CCD camera sensor A CCD camera sensor consists of an array of several lines of CCD-chips. Each chip corresponds to one pixel of the final digital image and has two functionalities: (1) It is an optoelectronic converter, transferring the impinging light into voltage. (2) It acts as shift register, which transfers the voltage of the neighboring chip either to the next or off the array to an analog digital converter, to create the final digital image (Löffler-Mang, 2012). As the transfer process takes significantly longer than the time

delay between two PIV recordings the commonly used sensor architecture splits the chip into an optoelectronic sensor and a shift register. This configuration is called progressive scan interline transfer CCD (Raffel et al., 2007, Adrian and Westerweel, 2010, Löffler-Mang, 2012). It reduces the transfer time, such that a consecutive image pair, single exposure double frame images, can be recorded. To further reduce the read-out time, the CCD array can be split into several sub-arrays, either line wise or rectangular, which are then read out separately. A drawback of this method is that each array has its own analog digital converter, which can result in slightly different conversions, such that the final image has brighter and darker regions or lines of pixels. This can e.g. be observed in the images used in Chapter 5, where the left side is brighter than the right side (cf. Fig. 5.4). An additional drawback of the progressive scan interline transfer architecture is that only half of the pixel's area is sensitive to light, such that less light is collected by the sensor, and the dynamic range of the image is lower. This can be overcome by installing a micro-lens above each chip, which focuses the light impinging on the pixel to the optoelectronic sensor of the pixel (Adrian and Westerweel, 2010, Raffel et al., 2007).

Pixelization A digital camera sensor consists of several thousands of light sensitive chips[4] with each chip corresponding to one pixel of the digital image. The gray value of each pixel is a result of the number of photons that hit the corresponding chip within the exposure time δ_t of the recording. Moreover, the gray level depends on the transfer function of the analog signal to the digital signal, which relates the voltage of each pixel to a gray level value. The gray levels are integer values, depending on the data range of the camera 255 gray levels ($8\,bit$) or 4095 gray levels ($12\,bit$) are possible. The largest integer value always corresponds to white, while zero corresponds to black. Due to the integer spacing of the gray level bins, the voltage signal cannot be transferred one to one, but is interpolated in between. The resulting gray value of each pixel is therefore on the one hand a time and spatial average of photons hitting the pixel's area within the exposure time δ_t and on the other hand a value rounded to fit in one of the gray level bins. Thus, particle images that are not centered within one pixel are mapped in a non-even way onto the neighboring pixels (cf. Section 4.1.1).

2.2 Evaluation of Image Data

As the seeding density of the images is so high that a corresponding single particle pair cannot be distinguished, PIV images are evaluated using a concept often applied in statistics to define the relation between two random variables X and Y. To determine if there is a systematic relation between both variables, often the correlation coefficient r_{XY}, Eq. (2.9), is calculated (Fahrmeir et al., 2004). A result close to 1 indicates that both variables have a linear relationship, while a result close to 0 indicates that both variables are completely independent of each other.

$$r_{XY} = \frac{\sum_{i=1}^{N}(X_i - \mu_X)(Y_i - \mu_Y)}{\sigma_X \sigma_Y} \tag{2.9}$$

[4] A common size of a current PIV camera chip array is in the range of $1024 \times 1024\,px$ to $2048 \times 2048\,px$.

In PIV two particle images, recorded a time delay Δt apart, are compared to determine the displacement of the particles $\mathbf{d}$ between the two images. Since the images are two-dimensional the correlation, Eq. (2.9), will also result in a multi-dimensional function rather than a single value. If the particle pattern is similar a so-called correlation peak at the most probable displacement will occur (cf. Fig. 2.1). The spatial position of this maximum then indicates the mean displacement $\mathbf{d}$ of the particles within the images correlated. As the time delay Δt between the images and the magnification factor of the set-up M_{lens} are known, the displacement can be transferred into a mean velocity $\mathbf{v}$.

$$\mathbf{v} = \frac{\mathbf{d}}{\Delta t M_{lens}} \tag{2.10}$$

Based on this principle several evaluation strategies have been developed over the past thirty years (cf. Section 1.1). In the next sections two methods are explained which led to the development of SPE. Then the evaluation routine of SPE is discussed.

2.2.1 Interrogation Window Correlation

This evaluation strategy is the most simple and also the most common evaluation method. It divides the image into a number of subregions of size $l_x \times l_y$, also called interrogation windows. These regions are correlated between the two recordings; the position of the maximum of the resulting correlation function defines the most probable displacement $\mathbf{d}$ within this interrogation window, compare Fig. 2.3. Common sizes of interrogation areas are in the range of $64 \times 64\,px$ to $16 \times 16\,px$. So an image of $2048 \times 2048\,px$ results in a rather low number of 32×32 to 128×128 velocity vectors. Considering digital images, the correlation function $R(x, y, r_x, r_y)$ of two consecutive images, I_1 and I_2 recorded at a time delay of Δt, can be determined as follows:

$$R(x, y, r_x, r_y) = \frac{1}{l_x l_y} \sum_{x=1}^{l_x} \sum_{y=1}^{l_y} I_1(x, y) I_2(x + r_x, y + r_y) \tag{2.11}$$

Consequently, the vector of each interrogation window represents the spatially averaged flow velocity of this area. To determine the correct displacement, the correlation peak has to be identified in the correlation function. Its amplitude depends on the number of particle image pairs correlated between the two consecutive interrogation areas. Therefore, the interrogation window size not only influences the number of velocity vectors gained, but also their quality. A smaller interrogation area contains less particles, such that the possibility of none or fewer correlation partners in the consecutive interrogation area increases. Using synthetic images, Keane and Adrian (1990, 1992) showed that a displacement of 25% of the interrogation window length and a number of at least seven particles per interrogation window lead to well pronounced and easy detectable correlation peaks if the out-off-plane displacement in the direction normal to the object plane and a possible velocity gradient in the interrogation area are small. As these restrictions are not always fulfilled, several strategies have been introduced in the past years to increase the detectability of the correlation peak.

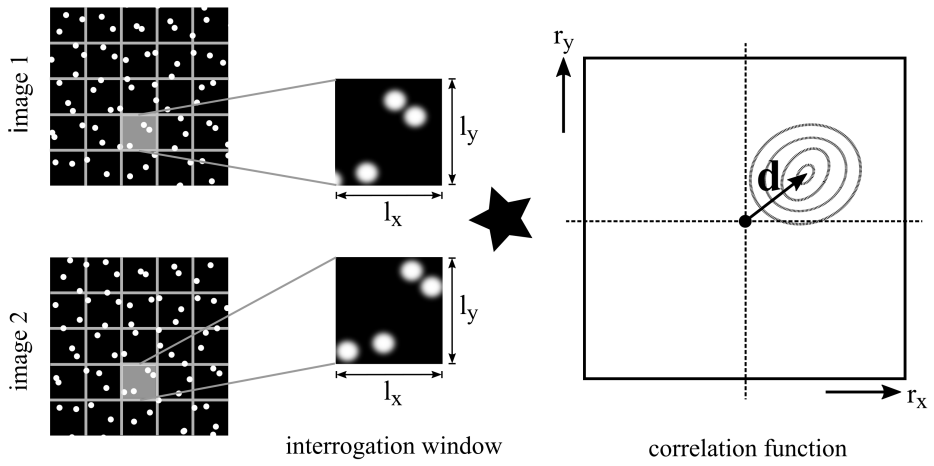

Figure 2.3: Schematic description of the standard PIV evaluation algorithm. The $\star$ symbolizes the cross-correlation operation.

Multi-Pass Method The multi-pass method was introduced by Westerweel et al. (1997) to increase the number of particle image pairs by shifting the position of the interrogation area in the second frame according to the estimated displacement. This can be performed in two or more steps: Starting with the standard approach and zero off-set a first estimate of the flow velocities is determined. This estimate is then filtered to remove spurious vectors, before it is used in the next step to reposition the interrogation window in the second image. Wereley and Meinhart (2001) further improved this method to increase its accuracy by shifting not only the interrogation area of the second image, but also of the first. They propose to shift the position of both areas by half of the displacement, the first against and the second in the direction of the displacement. This raises the spatial accuracy from first to second order.

Multi-Grid Method Willert (1997) proposed to iteratively decrease the size of the interrogation windows. Starting off with a rather rough spacing of interrogation areas, to determine a first estimate of the window off-set, the size of the interrogation areas is reduced from iteration step to iteration step. Thus, this method is able to cover many different velocity scales, as long as the variations in a close-by region are not too large. Since then the iteration process would not converge. The size of the smallest interrogation area is limited, such that at least four particle image pairs contribute to the correlation peak. Otherwise the peak is not distinguishable from the surrounding noise.

Window Deformation Method This method increases the number of correlated particle image pairs if there is a strong velocity gradient in the flow. The standard evaluation assumes that the velocity in an interrogation area is uniform, as otherwise the correlation peak would be smeared and result in biased velocity values. The window deformation method therefore deforms the second interrogation window according to the estimated displacement

gradient. If combined with the techniques above, it results in a strong increase of the number of valid vectors especially in regions of vortices and boundary layers. A possible algorithm is explained in detail by Scarano (2002).

Besides the above described adjustments, another approach to increase the number of samples contributing to the correlation peak has been proposed - averaging correlation functions either in space or in time. The later has been introduced independently by Delnoij et al. (1999) and Meinhart et al. (1999). This time-averaging of correlation functions is the topic of the next section. In contrast to the methods described so far, it removes all time-depended information of the flow, and is consequently only capable of determining time-averaged quantities.

2.2.2 Ensemble Average Correlation

In microscopic PIV applications the particle density of the images recorded is especially low, which increases the faultiness of the velocities estimated by the standard evaluation approach. As the flows examined in microscopic applications are usually laminar and steady or periodic, there is no need for instantaneous information. Therefore, Meinhart et al. (2000) compared three different averaging approaches to increase the signal to noise ratio of the correlation function:

- time-averaging of filtered instantaneous velocity data (Santiago et al., 1998);
- time-averaging of particle images ahead of correlation (Meinhart et al., 1999);
- time-averaging of correlation functions (Meinhart et al., 1999, Delnoij et al., 1999).

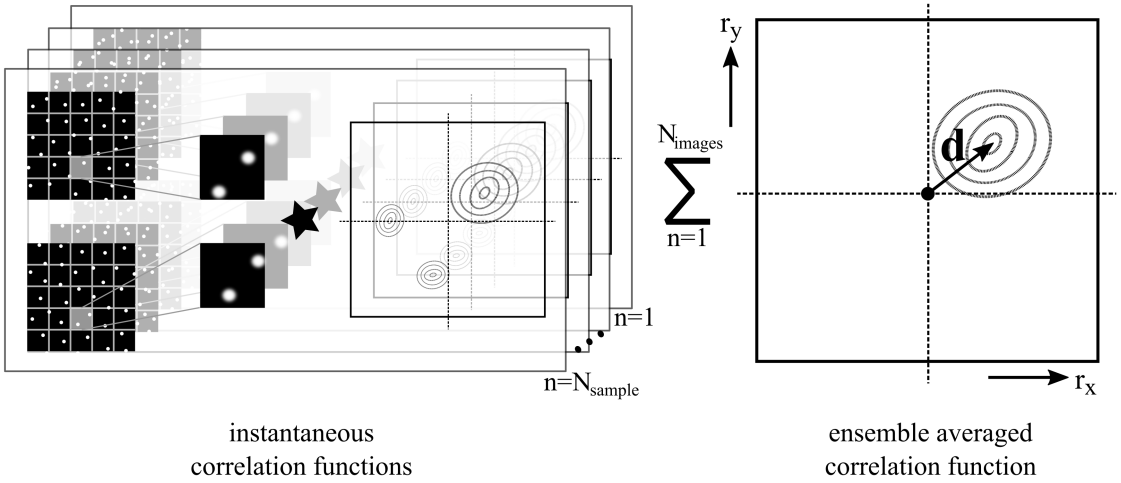

Figure 2.4: Schematic description of ensemble PIV evaluation. The $\star$ symbolizes the cross-correlation operation.

While the first depends on the accuracy of the computed velocity values and therefore on the filters applied before averaging, the second increases the accuracy as well as the computation speed since the correlation process has to be performed only once. On the other hand

time-averaging of images strongly depends on the seeding density and particle size, as due to the averaging the particle images will overlap and at some point cover the whole image. Then the computation of correlation functions becomes useless.

The last averaging strategy, time-averaging correlation functions, has been shown to be the most efficient. It computes the correlation functions of each image pair, as in the standard approach, compare Eq. (2.11), and then averages the correlation functions in time, see Eq. (2.12). Afterwards the position of the correlation peak and the corresponding mean displacement are determined as in the standard approach, see Fig. 2.4. So the results are not only averaged in space but also in time.

$$R(x, y, r_x, r_y) = \frac{1}{N_{images}} \sum_{n=1}^{N_{images}} \frac{1}{l_x l_y} \sum_{x=1}^{l_x} \sum_{y=1}^{l_y} I_1(x, y) I_2(x + r_x, y + r_y) \tag{2.12}$$

Willert (2008) proposed moreover to include this method into the multi-pass, grid-refinement and image deformation methods as it converges faster due to the ensemble averaging. Following the work of Hohreiter et al. (2002), Kähler et al. (2006), he suggests to determine a first estimate of the Reynolds stresses by fitting a two-dimensional Gaussian curve into the correlation and autocorrelation peak.

2.2.3 Single Pixel Ensemble Correlation

The ensemble average method showed that the signal to noise ratio of the correlation function can not only be improved by increasing the number of particle images within one interrogation area but also by accumulating particle samples in time due to the averaging of correlation functions. Westerweel et al. (2004) demonstrated that this technique can be used to increase the spatial resolution. They proposed that the number of samples contributing to a correlation peak of a $32 \times 32\,px$ interrogation area can also be obtained if the correlation is performed between single pixels, ensemble averaged over 1024 image pairs. This time-averaged correlation process is illustrated in Fig. 2.5 and can be expressed using the following relation:

$$R(x, y, r_x, r_y) = \frac{1}{N_{images}} \sum_{n=1}^{N_{images}} I_1(x, y) I_2(x + r_x, y + r_y) \tag{2.13}$$

The main difference between this approach and the standard correlation method lays in the fact that SPE is a two point correlation averaged in time, while the former method determined a spatial average, which was considered equal to this two-point time-averaged correlation, assuming a velocity field uniform across the interrogation area.

The SPE approach has the drawback that instantaneous information is not available at first glance. Therefore, it was first only applicable for quasi-stationary flows, as they are observed e.g. in microscopic PIV set-ups or images recorded by high speed cameras (Westerweel et al.,

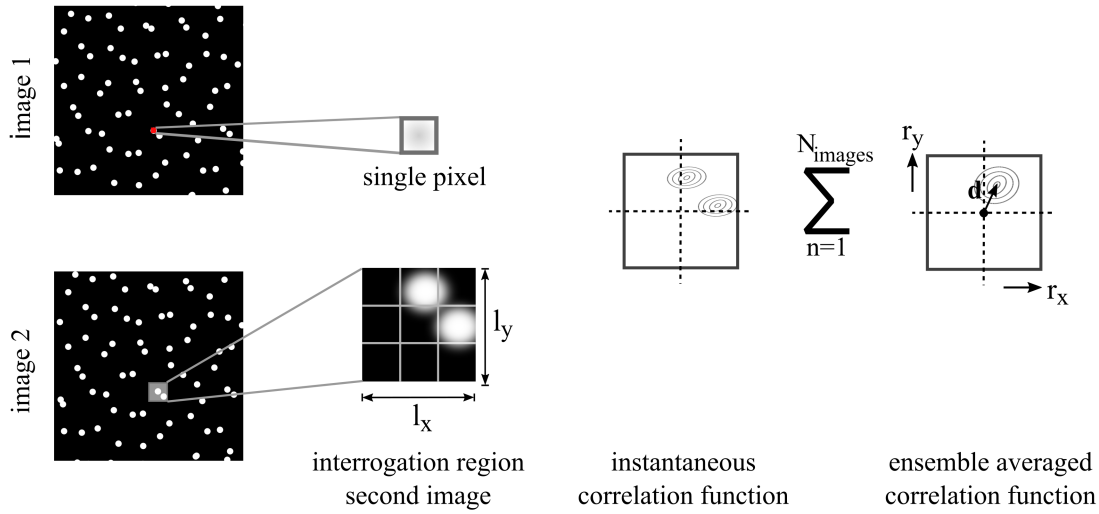

Figure 2.5: Schematic description of Single Pixel Ensemble PIV evaluation.

2004, Wereley et al., 2005a).

Billy et al. (2004) showed that also periodic laminar flows can be examined, while Kähler et al. (2006) demonstrated that even turbulent flows can be evaluated using this concept. Recently, Avallone et al. (2015) proposed a method to increase the number of samples without recording further images. They suggest to not only correlate the first image with the second image, but also vice versa, which doubles the number of samples and, thus, increases the accuracy. In the past few years two methods have been introduced, which extended the SPE technique to determine also Reynolds stresses and higher order moments.

Gaussian Fit Considering the theory of Adrian (1988), the correlation function is the convolution of the particle image and the velocity Joint Probability Density Function. As the convolution of two Gaussian functions (a) and (b) will be again a Gaussian function with diameter $d_{conv} = \sqrt{d^2_{gauss,a} + d^2_{gauss,b}}$, Scharnowski et al. (2012), Kähler and Scholz (2006) proposed to fit two-dimensional Gaussian curves into the correlation and the autocorrelation peak[5] to retrieve the statistical parameters of the velocity JPDF and therefore the Reynolds stresses, which are equivalent to the variances and the covariance of the velocity components. Scharnowski et al. (2012) further tested the reliability of this technique with respect to particle image diameter, the number of image pairs evaluated and the shape of the correlation function. They found that the best particle image diameters are in the range of 1.5-5 px and that the number of image pairs evaluated strongly influences the result. Furthermore, they concluded that as long as the functions are Gaussian shaped their parameters can be recovered at sufficient accuracy.

[5]The autocorrelation function contains the particle image (cf. Section 3.1.1)

Deconvolution Scharnowski and Kähler (2013) introduced a second method, based on the fact that the correlation function can be considered the convolution of the velocity JPDF and the autocorrelation function (Adrian, 1988, Soria and Willert, 2012). They proposed to determine the velocity JPDF directly by deconvolution. As direct deconvolution is not possible due to the finite size of the images and the noise contained - a problem well known to astronomers - they apply an iterative algorithm to deconvolve the correlation function by the autocorrelation function. There are several different deconvolution algorithms, which have been developed in astronomy, to remove the PSF of the telescope from star images; an overview of common deconvolution methods and their advantages and disadvantages can be found in Starck et al. (2002). Although, each deconvolution algorithm faces its own challenges depending on the underlying evaluation strategy, there is one problem they all encounter: their resolution cannot be finer than the resolution of the input signal, which in SPE is the size of one pixel. That this limitation is problematic can for example be seen in the findings of Avallone et al. (2015), who applied the method onto SPE results of a vertical jet. They observed Reynolds normal stresses in regions off the jet which are significantly larger than the stresses observed by the standard approach, which are almost zero - as physically expected. They justify this difference with the small deviation between the autocorrelation and the cross-correlation function and the resulting strong dependency on the correct estimation of the autocorrelation function used in the deconvolution process. However, this is not the main reason for the error. As a signal recovered by deconvolution cannot be sampled more accurately than the original signals, deconvolution cannot recover JPDFs narrower than one pixel.

2.3 Summary

This chapter introduced the basics of PIV. The first part defined all terms connected to image acquisition, which included the properties of seeding particles, the illumination and the recording cameras. The second part focused on the evaluation routines leading to SPE. The main challenge for SPE is to recover further statistical parameters of the flow besides mean velocities. Two methods found in the literature were introduced in the past section, Gaussian fit and deconvolution. While the first method, fitting a Gaussian curve into the correlation and autocorrelation functions is restricted to Gaussian shaped JPDFs, the second method depends on an iterative deconvolution procedure and is not able to restore JPDFs smaller than the pixel spacing of the image. Thus, there is a need for a method capable of recovering the statistical parameters of a velocity JPDF of arbitrary shape and size.

3 Estimating Statistical Moments of Velocity Probability Density Functions

In the previous chapter the basic components of PIV and the evaluation methods that led to SPE were introduced. Furthermore, the limitations of the different SPE evaluation routines found in the literature were explained. As the evaluation of the peak position of SPE correlation functions only leads to time-averaged velocity values, evaluation strategies to recover further informations on the flow have been introduced in the literature, based on the fact that the velocity JPDF is stored in the correlation function: (1) determining the mean and variance of the JPDFs by fitting Gaussian curves in the correlation and autocorrelation function (Kähler and Scholz, 2006, Scharnowski et al., 2012); (2) deconvolving the correlation function using the autocorrelation function and determining the moments of the resulting function (Scharnowski and Kähler, 2013). The first strategy is able to recover the statistical moments of the JPDF as long as it is Gaussian shaped. The second is capable of recovering statistical moments of JPDFs of various shapes but is restricted on the pixel grid spacing due to the deconvolution process.

In the following chapter a third method will be derived, which is capable of estimating the statistical moments of the velocity JPDF independent of its shape and width. The method uses the statistical parameters of the correlation and the autocorrelation functions to determine the moments of the JPDF. The chapter starts with a description of PIV in a mathematical sense as needed to develop the new method. Then the new evaluation method is derived and definitions of different statistical moments are recalled. Afterwards, the physical meaning of the first four statistical moments in of a turbulent velocity signal is explained briefly. In a last section the influence of noise on the evaluation of correlation functions is addressed and several methods to lower this effect are discussed.

3.1 Mathematical Description of PIV

The following sections define several terms introduced in Chapter 2 in a mathematical sense. The model used assumes an ideal situation to keep the formulas as simple as possible. This includes that all particles have the same size, are perfect spheres, and are in focus within an infinitely thin light sheet. Furthermore, the illumination and the seeding are homogeneous, there are no errors in the lenses or due to the recording system and all particles follow the flow perfectly and do not disturb the flow. Under these conditions, first an image of particles is defined, then the central part of PIV - the correlation function - is discussed.

3.1.1 Image of Particles

The intensity pattern $I(\mathbf{x})$ of an image of particles can be described by the convolution of the positions of the particles in space $W(\mathbf{x})$ with the imaging function of an ideal particle $I_{part}(\mathbf{x})$,

$$I(\mathbf{x}) = \int W(\zeta)\, I_{part}(\mathbf{x} - \zeta)\, d\zeta. \tag{3.1}$$

The particle positions $W(\mathbf{x})$ can be described by Dirac delta peaks, $\delta(\mathbf{x} - \mathbf{x}_{part})$, distributed at random positions, $\mathbf{x}_{part}$, in the object plane. The imaging function of a particle, $I_{part}(\mathbf{x})$, describes the image of a single particle, as it can be seen in a photograph. It consists of two parts[1]:

1. the geometric image of the particle, d_{geom};
2. the Point Spread Function (PSF) of the optical aperture, d_s.

Geometric Image The geometric image describes the mapping of the particle from the object plane onto the image plane (cf. Fig. 2.2). Assuming that the particle shape is a perfect sphere the geometric imaging function can be approximated by a Gaussian curve. The diameter of the curve, d_{geom}, can be expressed as the physical diameter of the particle, d_{part}, multiplied by the magnification factor of the optical system M_{lens}, Eq. (3.2).

$$d_{geom} = d_{part} M_{lens} \tag{3.2}$$

Point Spread Function (PSF) The PSF considers that light passing a lens is diffracted, such that the image of an infinitely small point is represented by a point of finite diameter in the image plane. The diameter of this point is called *diffraction limited diameter* d_s (Raffel et al., 2007). The PSF of a circular aperture, as in general used in cameras, is described by the Airy function. This function produces the so called Airy disc pattern (cf. Fig. 3.1) :

Figure 3.1: Airy disk pattern produced by light passing a circular aperture. The gray level scale has been adjusted to the maximum of the first ring, to make the outer rings visible.

[1] In this simplified model neither the influence of lens aberrations nor of particles positioned off the object plane are considered, which also contribute to I_{part}. A detailed description of these impacts can be found in Adrian and Westerweel (2010).

A bright circular spot in the center surrounded by several dark and bright rings, corresponding to minima and maxima of the Airy function. The diameter of the first dark ring defines the diffraction limited diameter, d_s, Eq. (3.3). It depends on the wavelength, λ, of the light illuminating the point source the focal length, f, and the diameter of the aperture, D_a.

$$d_s = 2.44\lambda \frac{f}{D_a}\,(1 + M_{lens}) \tag{3.3}$$

As the error made is small, the Airy function is usually approximated by a Gaussian curve with diameter d_s to simplify calculations (Adrian and Yao, 1985).
The PSF, convolved with the geometric image of a particle, forms the imaging function of a particle, $I_{part}\,(\mathbf{x})$. Since both functions, the geometric image and the PSF are assumed to be Gaussian shaped and the convolution of two Gaussian functions (a) and (b) leads to a Gaussian function with diameter $d_{conv} = \sqrt{d_{gauss,a}^2 + d_{gauss,b}^2}$, the final diameter of a particle image can be estimated by Eq.(3.4).

$$d_e = \sqrt{d_{geom}^2 + d_s^2} \tag{3.4}$$

This diameter is in many cases referred to as the *effective particle image diameter* d_e. Consequently, the particle imaging function can be expressed by a normal distribution function with mean, $\mu = 0$ and standard deviation $\sigma = 0.5\,d_e$.

$$I_{part}(\mathbf{x}) = \frac{1}{\sqrt{0.5\pi d_e^2}}\, e^{-\frac{x^2}{0.5 d_e^2}} \tag{3.5}$$

The pre-factor $1/\sqrt{0.5\pi d_e^2}$, which normalizes the area under the curve to one, controls the brightness of the particle image, because it defines the maximum of the normal distribution (Gui and Seiner, 2004).

As always two consecutive images are correlated to determine the flow velocity, a nomenclature for all variables related to the first or second image has to be defined. Throughout this work all variables with subscript 1 will correspond to the first image and all variables with a subscript 2 to the second image. Accordingly, the final definitions for the first and second image are:

$$I_1(\mathbf{x}, t) = I(\mathbf{x}, t) = \int W_1(\zeta) I_{part}(\mathbf{x} - \zeta) d\zeta; \quad \text{with } W_1(\mathbf{x}) = W(\mathbf{x}, t) \tag{3.6}$$

$$I_2(\mathbf{x}, t) = I(\mathbf{x}, t + \Delta t) = \int W_2(\zeta) I_{part}(\mathbf{x} - \zeta) d\zeta; \quad \text{with } W_2(\mathbf{x}) = W(\mathbf{x}, t + \Delta t) \tag{3.7}$$

3.1.2 Cross-Correlation Function - General Definition

The instantaneous cross-correlation function $R(\mathbf{x}, \mathbf{r}, t)$ of two consecutive images, $I_1(\mathbf{x}, t)$ and $I_2(\mathbf{x}, t)$, is defined by the following equation:

$$R(\mathbf{x}, \mathbf{r}, t) = \int I_1(\mathbf{x}, t) I_2(\mathbf{x} + \mathbf{r}, t) d\mathbf{x} \tag{3.8}$$

with $\mathbf{r}$ the displacement between the spatial positions in the first and second image. As introduced in Section 2.2.1, not the images as a whole, but subregions, interrogation areas, at different spatial position $\mathbf{x}$, are correlated, thus the correlation function $R(\mathbf{r}, t)$ also depends on the spatial position $\mathbf{x}$ of the interrogation area. In the following, the correlation function of only one interrogation area at a fixed position $\mathbf{x}$ will be considered, such that $R(\mathbf{x}, \mathbf{r}, t) = R(\mathbf{r}, t)$. The resulting velocity vector of this correlation function then represents the spatial average of all particle velocities in this investigated subregion. Assuming that the flow field is stationary and homogeneous across the interrogation area, this spatial average is equivalent to an ensemble averaged two-point correlation (Adrian and Westerweel, 2010). So Eq. (3.8) can as well be written as:

$$R(\mathbf{r}) = \langle I_1(\mathbf{x}, t) I_2(\mathbf{x} + \mathbf{r}, t) \rangle. \tag{3.9}$$

The $\langle \cdot \rangle$ brackets symbolize the ensemble average in time, defined as:

$$\langle I(\mathbf{x}, t) \rangle = \frac{1}{N_{timesteps}} \sum_{i=1}^{N_{timesteps}} I(x, t_i). \tag{3.10}$$

Therefore, the time-dependence of the correlation function in Eq. (3.8) can be relaxed. Furthermore, one can introduce a simplified notation for cross-correlation, marking this operation by a $\star$. This leads to the following expression for the correlation function:

$$R(\mathbf{r}) = (I_1 \star I_2)(\mathbf{r}). \tag{3.11}$$

Any cross-correlation can be transferred into a convolution, marked by $*$, since the cross-correlation of two arbitrary functions $h(x)$ and $g(x)$ is equivalent to the convolution of function $h(x)$ with the complex conjugate of function $g^\star(x)$. Hence, Eq. (3.11) can also be written as

$$R(\mathbf{r}) = (I_1 * I_2^\star)(\mathbf{r}). \tag{3.12}$$

The complex conjugate of a real function is the function itself, thus, $I_2^\star = I_2$. Therefore, the cross-correlation can be expressed as the convolution of image one and image two:

$$R(\mathbf{r}) = (I_1 * I_2)(\mathbf{r}) \tag{3.13}$$

3.1.3 The Different Components of the Correlation Function

A common principle, following the introduction of ensemble averaging, is to decompose an instantaneous variable into a mean and a fluctuating part, as it is well known from the Reynolds decomposition. Adrian (1994) applied this principle onto PIV images, assuming that only the particle positions will change within an ensemble of images, but not the seeding density, the illumination intensity or any other parameter that would further influence the image intensities. So the image intensity is decomposed into a mean $\langle I(\mathbf{x},t)\rangle$ and a fluctuating part $I'(\mathbf{x},t)$.

$$I(\mathbf{x},t) = \langle I(\mathbf{x},t)\rangle + I'(\mathbf{x},t) \tag{3.14}$$

Inserting Eq. (3.14) into Eq. (3.8) leads to the decomposed correlation function, consisting of three parts:

$$\begin{aligned} R(\mathbf{r},t) = & \underbrace{\int \langle I_1(\mathbf{x},t)\rangle\langle I_2(\mathbf{x}+\mathbf{r},t)\rangle d\mathbf{x}}_{R_C} + \\ & \underbrace{\int \langle I_1(\mathbf{x},t)\rangle I_2'(\mathbf{x}+\mathbf{r},t)d\mathbf{x} + \int \langle I_2(\mathbf{x},t)\rangle I_1'(\mathbf{x}+\mathbf{r},t)d\mathbf{x}}_{R_F} + \\ & \underbrace{\int I_1'(\mathbf{x},t)I_2'(\mathbf{x}+\mathbf{r},t)d\mathbf{x}}_{R_D} \end{aligned} \tag{3.15}$$

1. $R_C(\mathbf{r},t)$: the correlation of the mean intensities;
2. $R_F(\mathbf{r},t)$: the correlation of the fluctuating part of one image by the mean of the other;
3. $R_D(\mathbf{r},t)$: the correlation of the fluctuations of both images.

While the first two correspond to the noise surrounding the correlation peak, the last contains the actual particle displacement (Keane and Adrian, 1992, Adrian, 1994, Westerweel, 2000). Ensemble averaging of the decomposed correlation function, Eq. (3.15), in time, removes the term R_F as time-averaged fluctuations of a statistically random function are zero, $\langle I'(\mathbf{x},t)\rangle = 0$.

$$R(\mathbf{r}) = \langle I_1(\mathbf{x},t)\rangle\langle I_2(\mathbf{x}+\mathbf{r},t)\rangle + \langle I_1'(\mathbf{x},t)I_2'(\mathbf{x}+\mathbf{r},t)\rangle = R_C(\mathbf{r}) + R_D(\mathbf{r}) \tag{3.16}$$

Consequently, noise generated by correlating mean intensities can be removed from the correlation function:

$$R_D(\mathbf{r}) = R(\mathbf{r}) - R_C(\mathbf{r}) = \langle I_1(\mathbf{x},t)I_2(\mathbf{x}+\mathbf{r},t)\rangle - \langle I_1(\mathbf{x},t)\rangle\langle I_2(\mathbf{x}+\mathbf{r},t)\rangle \tag{3.17}$$

3.1.4 Correlation Function of Two Consecutive Images and the Velocity JPDF

Comparing two images, $I_1(\mathbf{x},t)$ and $I_2(\mathbf{x},t)$, recorded at a time difference of Δt, one can assume that the particle pattern observed in the second image, is the same as the pattern of the first image, but shifted by a displacement vector $\mathbf{d}(\mathbf{x},t)$. Thus, the intensity field of the second image can be described as the intensity fields of the first image shifted by the velocity vector $\mathbf{v} = \frac{\mathbf{d(x,t)}}{\mathbf{\Delta t}}$. This shifting is mathematically represented by the Dirac delta function, $\delta(a-b)$, which has the following sifting property (Chakraborty, 2008):

$$h(a) = \int h(x)\delta(x-a)dx = \int h(x)\delta(a-x)dx = \int h(x)\delta(a-g(x))dx \tag{3.18}$$

with $g(x)$ being an arbitrary function. Using this property, one can express the intensity field of the second image as a function of the first image:

$$I_2(\mathbf{x}') = \int I_1(\mathbf{x})\delta(\mathbf{x}' - d_v(\mathbf{x},t))d\mathbf{x} = (I_1 * \delta_{d_v})(\mathbf{x}',t) \tag{3.19}$$

with $d_v(\mathbf{x},t) = \mathbf{x} + \mathbf{d}(\mathbf{x},t)$. This property can be used to show that the correlation function contains the JPDF of the velocity. Since only R_D contains information on the displacement of the particles in this section only the fluctuations of the intensities will be considered, thus Eq. (3.19) reads

$$I_2'(\mathbf{x}') = \int I_1'(\mathbf{x})\delta(\mathbf{x}' - d_v(\mathbf{x},t))d\mathbf{x} = (I_1' * \delta_{d_v})(\mathbf{x}',t). \tag{3.20}$$

Entering this into R_D (cf. Eq. (3.15)) leads to

$$R_D(\mathbf{r},t) = (I_1' * (I_1' * \delta_{d_v}))(\mathbf{r},t). \tag{3.21}$$

Because convolution is an associative operation, Eq. (3.21) can be reorganized as follows:

$$R_D(\mathbf{r},t) = ((I_1' * I_1') * \delta_v)(\mathbf{r},t) = (I_1'^2 * \delta_v)(\mathbf{r},t) = \int I_1'^2(\mathbf{x}'',t)\delta(\mathbf{r} - d_v(\mathbf{x}'',t))d\mathbf{x}'' \tag{3.22}$$

with $I_1'^2(\mathbf{x}'',t) = \int I_1'(\mathbf{x},t)I_1'(\mathbf{x}''-\mathbf{x},t)d\mathbf{x}$ being the autocorrelation function of the fluctuations of the first image. Thus, Eq. (3.22) can also be expressed by

$$R_D(\mathbf{r},t) = \int\int I_1'(\mathbf{x},t)I_1'(\mathbf{x}''-\mathbf{x},t)\delta(\mathbf{r} - d_v(\mathbf{x}'',t))d\mathbf{x}d\mathbf{x}''. \tag{3.23}$$

Since the instantaneous spatial correlation of two interrogation windows is an estimator of the two-point ensemble averaged correlation assuming a homogeneous and statistically

stationary flow within the interrogation area (cf. Section 3.1.2), Eq. (3.23) can also be written as:

$$\begin{aligned} R_D(\mathbf{r}) &= \int \langle I_1'(\mathbf{x},t) I_1'(\mathbf{x}''-\mathbf{x},t)\delta(\mathbf{r}-d_v(\mathbf{x}'',t))\rangle d\mathbf{x}'' \\ &= \int \langle I_1'(\mathbf{x},t) I_1'(\mathbf{x}''-\mathbf{x},t)\delta(\mathbf{r}-\mathbf{x}''-\mathbf{d}(\mathbf{x}'',t))\rangle d\mathbf{x}'' \end{aligned} \tag{3.24}$$

Further the variables within the Dirac delta function can be changed from $\mathbf{r}-\mathbf{x}''-\mathbf{d}(\mathbf{x}'',t)$ to $\frac{\mathbf{d}(\mathbf{r}-\mathbf{x}'',t)}{\Delta t}-\mathbf{v}$, as the particle pattern of the second image will only be equivalent to the pattern of the first image if it is shifted by a displacement vector $\mathbf{d}(\mathbf{x},t)$, which corresponds to the flow velocity $\mathbf{v}$ and the time delay between the two images Δt.

$$R_D(\mathbf{r}) = \int \langle I_1'(\mathbf{x},t) I_1'(\mathbf{x}''-\mathbf{x},t)\delta(\frac{\mathbf{d}(\mathbf{r}-\mathbf{x}'',t)}{\Delta t}-\mathbf{v})\rangle d\mathbf{x}'' \tag{3.25}$$

Inserting the definition of the fine grained JPDF[2], $f'(\mathbf{v};\mathbf{x},t) \equiv \delta(\frac{\mathbf{d}(\mathbf{x},t)}{\Delta t}-\mathbf{v})$, into Eq. (3.25), the following expression results:

$$R_D(\mathbf{r}) = \int \langle I_1'(\mathbf{x},t) I_1'(\mathbf{x}''-\mathbf{x},t) f'(\mathbf{v};\mathbf{r}-\mathbf{x}'',t)\rangle d\mathbf{x}'' \tag{3.26}$$

After a further set of mathematical manipulations as described by Pope (2001), the final result can be achieved:

$$R_D(\mathbf{r}) = \langle I_1'(\mathbf{x},t) I_1'(\mathbf{x}''-\mathbf{x},t)|\frac{\mathbf{d}(\mathbf{x},t)}{\Delta t}=\mathbf{v}\rangle f(\mathbf{v};\mathbf{r}-\mathbf{x}'')d\mathbf{x}''. \tag{3.27}$$

Eq. (3.27) shows that the velocity JPDF, $f(\mathbf{v})$, is stored in the correlation function as a convolution with the autocorrelation function.

3.1.5 Normalizing the Correlation Function

Before the correlation function, Eq. (3.17), is further processed, it is often normalized to reduce the influence of inhomogeneities within the ensemble evaluated. These inhomogeneities can for example be different mean intensities across the image or the image series, which will, if correlated, add additional noise to the correlation function. The best result is reached if the correlation function is normalized by the product of the standard deviations of the autocorrelations of the first and second image (Fincham and Spedding, 1997, Burt et al., 1982). This is often referred to as the *variance normalized correlation function.* It is the same as the Pearson product-moment correlation coefficient r_{XY}, which is commonly used in statistics to determine the correlation of two variables X and Y (cf. Section 2.2). In case of PIV it is written the following:

[2]For further details on the fine grained PDF see e.g. Pope (2001)

$$r_{I_1 I_2} = \frac{\langle I_1 I_2 \rangle - \langle I_1 \rangle \langle I_2 \rangle}{\sqrt{\langle I_1^2 \rangle - \langle I_1 \rangle \langle I_1 \rangle} \sqrt{\langle I_2^2 \rangle - \langle I_2 \rangle \langle I_2 \rangle}}. \tag{3.28}$$

This function is the correlation function evaluated in the algorithms used in this work.

3.2 Recovering the Statistical Moments of the Velocity JPDF

As the standard evaluation of time-averaged correlation functions only recovers mean velocity values, additional information on the flow can only be found if Eq. (**??**) can be solved for the velocity JPDF. In the following sections a method is developed, which determines the moments of the velocity JPDF solely by a combination of the statistical moments of the correlation and the autocorrelation functions. As the statistical moments of the correlation and autocorrelation function can be determined directly, the method is independent of the shape and size of the JPDF. This derivation can also be found in Strobl et al. (2016). First definitions of statistical moments are recalled and their physical meaning in fluid mechanics is discussed. Then the representation of the correlation function in Fourier space and the calculation of statistical moments in Fourier space are discussed. Finally formulas to determine the mean, the variance, the skewness and the kurtosis of the velocity PDF as a combination of these statistical parameters of the correlation and autocorrelation function are derived.

3.2.1 Statistical Moments - Definition

To recall the definition of the statistical parameters of a PDF, three different example PDFs are depicted in Fig. 3.2. The first PDF, Fig. 3.2 (a) is a normal distribution function. It is characterized by its mean value, μ, and its variance, σ^2, which define the position of the maximum and the width of the function.
Comparing this function to Fig. 3.2 (b), the curve of (b) is not symmetric around the maximum and leans to the left-hand side. This characteristic is called skewness ν. In Fig. 3.2 (c) a third distribution function is shown. The mean of this functions is at the same position as the mean of the normal distribution, Fig. 3.2 (a), but the peak is flattened. This characteristic is described by the kurtosis or flatness κ.

These four main characteristic parameters of any PDF can also be quantified by the statistical moments of the PDF. The mean value corresponds to the first *raw moment*, the variance to the second *central moment* and the skewness and the kurtosis to the third and fourth *normalized central moment*. In the next paragraphs mathematical definitions of these three types of moments are given and their physical meaning is briefly explained.

Raw Moments The raw moment describes the characteristic of the distribution function $f(x)$ with respect to the origin of a given coordinate system, Eq. (3.29). The centroid of the

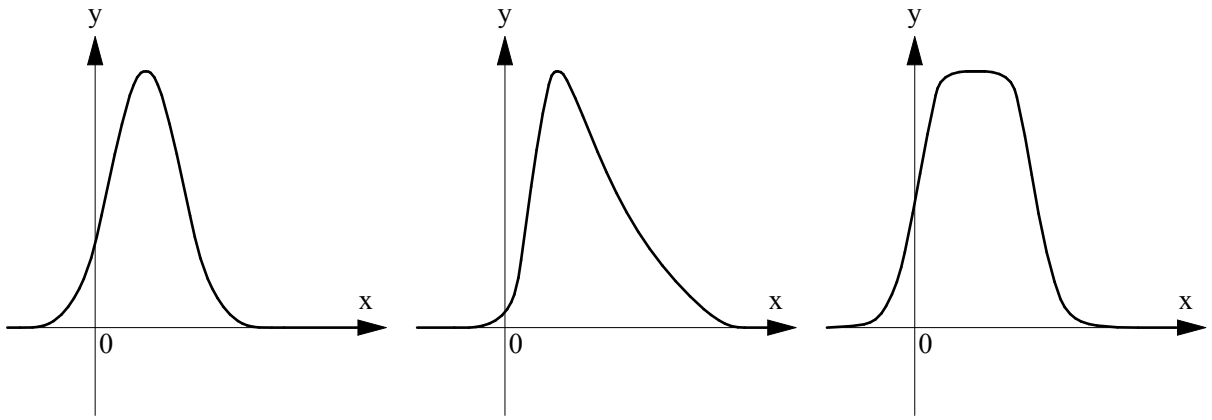

(a) Normal Distribution (b) Skewed Distribution (c) Flattened Distribution

Figure 3.2: PDFs of different shapes

function, the mean value μ, is therefore the first raw moment, M^1.

$$M^k = \int x^k f(x) dx \tag{3.29}$$

Central Moments The central moment, Eq. (3.30), is determined with respect to the centroid of the distribution function $f(x)$.

$$m^k = \int (x - M^1)^k f(x) dx = \int (x - \mu)^k f(x) dx \tag{3.30}$$

An example is the variance, σ^2, which describes the fluctuation of the distribution function around the mean value. In statistics often the square root of the variance, i.e. the standard deviation σ, is considered. This simplifies the comparison as the unit of the standard deviation is the same unit as of the mean value.

Normalized Central Moments The kth-normalized central moment is a dimensionless number. It is defined as the central moment, Eq. (3.30), but normalized by the standard deviation to the power of k, such that the result will be dimensionless, compare Eq. (3.31).

$$\mathring{m}^k = \int \left(\frac{x - M^1}{\sqrt{m^2}} \right)^k f(x) dx = \int \left(\frac{x - \mu}{\sigma} \right)^k f(x) dx \tag{3.31}$$

While the skewness ν ($k = 3$) measures the symmetry of the distribution function with respect to the perfectly symmetric normal distribution, the kurtosis κ ($k = 4$) is a measure of the shape of the distribution, taking into account the tails. For a normal distribution the skewness is zero, $\nu = 0$, and the kurtosis is equal to three, $\kappa = 3$. A skewness to the

left will be positive and a skewness to the right negative. The distribution of Fig. 3.2 (b) is therefore positively skewed. A kurtosis higher than 3 results in a peak smaller than the standard normal distribution and wider tales, while a value lower than 3 results in a more compact distribution function as it can be seen in Fig. 3.2 (c).

Due to their definition, the different types of moments can be converted into each other. While the normalized central moments only need to be multiplied by the standard deviation to the power of the moment's order to determine the central moment, the transfer between central and raw moments is slightly more laborious. Tab. 3.1 contains the conversion between central and raw moments up to fourth order.

k	m^k
1	0
2	$M^2 - (M^1)^2$
3	$M^3 + 2(M^1)^3 - 3M^1M^2$
4	$M^4 - 3(M^1)^4 + 6(M^1)^2M^2 - 4M^3M^1$

Table 3.1: Central moments expressed as a combination of raw moments

3.2.2 Physical Meaning of Statistical Moments of Velocity PDFs

Each of the four discussed parameters: mean, variance, skewness and kurtosis symbolize certain specifics of a flow field.

Mean values In the description of turbulent flows one generally defines three different types of mean values (cf. Pope (2001), Kundu and Cohen (2004)):

- Time Average
  Considering a flow stationary in time, the time-averaged velocity $\langle v(\mathbf{x})\rangle_{time}$ is determined as follows,

$$\langle v(\mathbf{x})\rangle_{time} = \frac{1}{T}\int v\left(\mathbf{x},t\right)dt \tag{3.32}$$

  resulting in a mean value independent in time.
- Spatial Average
  Considering a flow homogeneous in space, the mean value will be independent of the spatial location. Therefore, the spatial mean velocity $\langle v\left(t\right)\rangle_{space}$ is defined as:

$$\langle v\left(t\right)\rangle_{space} = \frac{1}{V}\int v\left(\mathbf{x},t\right)dV \tag{3.33}$$

  with V being the volume (3D) or the area (2D) of the spatial region averaged.
- Ensemble Average
  Determines the average of a set of N measured velocity values v_i, which may have been

recorded at different times and/or spatial positions.

$$\langle v \rangle = \frac{1}{N} \sum_{i=1}^{N} v_i \left(\mathbf{x}, t \right) \tag{3.34}$$

Depending on the assumptions made and conditions set, one average can be considered equivalent to the other. Assuming a flow field stationary in time and homogeneous in space, there will be no difference if the mean value is computed with respect to time or space, such that the average of 100 measurement values in time is equal to the average of a window of 10×10 measurement positions, as the number of samples used computing the average is equivalent.

Variances and Reynolds stresses The variances $\langle u'u' \rangle$, $\langle v'v' \rangle$ describe the fluctuation of the velocity components u, v about their mean, while the covariance $\langle u'v' \rangle$ describes the relation between the fluctuations of both velocity components u' and v'. Interpreted in a fluid mechanical sense, the variance as well as the covariance multiplied by the density of the fluid ρ represent the turbulent momentum fluxes (Frisch, 1995). The covariance for example then reads $\rho \langle u'v' \rangle$ and v' can be considered the advective term, which transports the momentum $\rho u'$. The covariance is therefore a description of the vertical mean flux of the streamwise momentum.

This exchange of momentum can also be interpreted as an additional stress, therefore the variance and covariance are usually referred to as Reynolds stresses to honor Osborne Reynolds, who was the first introducing the decomposition of an instantaneous value into a mean and a fluctuating part (Reynolds, 1895). The variances are the normal Reynolds stresses, while the covariance is the Reynolds shear stress. Due to their derivation, the Reynolds stresses are usually defined as $-\rho \langle u_i' u_j' \rangle$.

Skewness and Kurtosis The higher order moments, the skewness and kurtosis, identify how the distribution function deviates from the ideal Gaussian distribution. The skewness describes the symmetry of the distribution function with respect to the mean value. Considering for example the third moment of the streamwise velocity component u,

$$\langle u'^3 \rangle = \int (u - \langle u \rangle)^3 f(u) du \tag{3.35}$$

due to its exponent, $k = 3$, the term $u - \langle u \rangle$ defines the sign of the moment. A positively skewed distribution function, like in Fig. 3.2 (b), follows from a few velocities significantly larger than the mean value (Flierl and Ferrari, 2007). Similarly to the descriptions made for the covariance, the cross third central moments can as well be interpreted as the transport of the Reynolds stresses, such that $\langle u'u'v' \rangle$ describes the vertical transport of the normal streamwise Reynolds stress.

The kurtosis indicates the compactness of the distribution function. Small fluctuations around the mean in the range of the standard deviation result in small values of the kurtosis, like the distribution function shown in Fig. 3.2 (c), while the occurrence of rare extreme events, $|u'/\sqrt{u'^2}| > 10$ will result in large values of the kurtosis (Xu et al., 1996).

3.2.3 Correlation in Fourier Space

Considering the calculations in Section 3.1 and the description of several authors like Olsen and Adrian (2000), Adrian (1994) and Westerweel (1993), the correlation function $R(\mathbf{r})$ can be expressed as the convolution of the autocorrelation function of the fluctuations $I'^2_1(\mathbf{x})$ with the PDF of the velocity $f(\mathbf{v};\mathbf{x})$ under the condition, that all particles of the first image are contained in the second and that they are displaced by $\mathbf{d}$, which is equivalent to the flow velocity $\mathbf{v}$ times the time delay between the two images Δt.

$$R_D(\mathbf{r}) = \int I'^2_1(\mathbf{x}) f(\mathbf{v};\mathbf{r}-\mathbf{x}) d\mathbf{x} \tag{3.36}$$

Transforming Eq. (3.36) into Fourier space results in a simple multiplication of the Fourier transformed of the autocorrelation function, $\alpha(\mathbf{s})$, and the velocity JPDF, $\phi(\mathbf{s})$:

$$\tilde{R}(\mathbf{s}) = \alpha(\mathbf{s})\,\phi(\mathbf{s})\,. \tag{3.37}$$

3.2.4 Calculation of Moments in Fourier Space

The PDF of any variable a, $f(a;\mathbf{x})$, and the characteristic function of a probability distribution, $\xi(\mathbf{s})$, form a Fourier transform pair, see Eq. (3.38) and (3.39).

$$\xi(\mathbf{s}) = \int f(a;\mathbf{x})\, e^{i\mathbf{x}\mathbf{s}} d\mathbf{x} \tag{3.38}$$

$$f(a;\mathbf{x}) = \frac{1}{2\pi} \int \xi(\mathbf{s})\, e^{-i\mathbf{x}\mathbf{s}} d\mathbf{s} \tag{3.39}$$

Since the k-th raw moment of any PDF is defined as the k-th derivative of its characteristic function, $\xi(s)$, at position $\mathbf{s}=0$ (cf. e.g. Pope (2001)) it is possible to determine the moments of any PDF in real as well as in Fourier space.

$$M^k = \left.\frac{d^k \xi(s)}{ds^k}\right|_{\mathbf{s}=0} (-i)^k \tag{3.40}$$

3.2.5 Moments of the JPDF

Entering Eq. (3.37) into Eq. (3.40), it can be seen that the raw moments of the correlation function M^k_R are the k-th derivatives of the product of the Fourier transformed autocorrelation and the JPDF at position $\mathbf{s}=0$, Eq. (3.41). The derivative of a product of two functions can, according to the chain rule, be split into several terms, such that at the end a combination of raw moments of the JPDF and the autocorrelation function remains.

$$M_R^k = \left.\frac{d^k \tilde{R}(s)}{ds^k}\right|_{\mathbf{s}=0} (-i)^k = \left.\frac{d^k \phi(s)\,\alpha(s)}{ds^k}\right|_{\mathbf{s}=0} (-i)^k \tag{3.41}$$

As an example the calculation of the second raw moment, M_R^2, of the correlation function, using Eq. (3.41) with $k = 2$, is shown below.

$$\begin{aligned} M_R^2 &= \left.\frac{d^2\phi(s)\alpha(s)}{ds^2}\right|_{\mathbf{s}=0} (-i)^2 \\ &= \underbrace{\phi(0)}_{=1} \underbrace{\left.\frac{\partial^2\alpha}{\partial s^2}\right|_{\mathbf{s}=0} (-i)^2}_{=M_{auto}^2} + \underbrace{\alpha(0)}_{=1} \underbrace{\left.\frac{\partial^2\phi}{\partial s^2}\right|_{\mathbf{s}=0} (-i)^2}_{=M_{pdf}^2} + 2 \underbrace{\left.\frac{\partial\phi}{\partial s}\right|_{\mathbf{s}=0} (-i)^1}_{=M_{pdf}^1} \underbrace{\left.\frac{\partial\alpha}{\partial s}\right|_{\mathbf{s}=0} (-i)^1}_{=M_{auto}^1} \\ &= M_{pdf}^2 + M_{auto}^2 \end{aligned} \tag{3.42}$$

Since the first raw moment of the autocorrelation M_{auto}^1, the mean value, is equal to zero, the term $\frac{\partial\phi}{\partial s}\frac{\partial\alpha}{\partial s}$ vanishes, such that only the sum of the second raw moments remains. This sum can easily be transformed into the sum of the second central moments, using the relations listed in Tab. 3.1. The result of Eq. (3.42) is not any different to the already stated result for the convolution of two Gaussian shaped curves (a) and (b), where the resulting diameter is $d_{conv} = \sqrt{d_{gauss,a}^2 + d_{gauss,b}^2}$, except that it was achieved using arbitrary functions.

The calculation procedure for moments of higher order is similar. The results of the first four raw moments are collected in Tab. 3.2. Setting up these relations, it was assumed that the autocorrelation function is Gaussian shaped and positioned at the origin. Due to the symmetry of the Gaussian function, all odd moments, e.g. $M_{auto}^1 = 0$ and $M_{auto}^3 = 0$, are zero.

	R
M^1	M_{pdf}^1
M^2	$M_{pdf}^2 + M_{auto}^2$
M^3	$M_{pdf}^3 + 3M_{pdf}^1 M_{auto}^2$
M^4	$M_{pdf}^4 + M_{auto}^4 + 6M_{pdf}^2 M_{auto}^2$

Table 3.2: Raw moments of the correlation function R, the JPDF of the velocity and the autocorrelation function.

It is straight forward to solve the equations of Tab. 3.2 for the raw moments of the velocity JPDF and transform them into central or even normalized central moments using the relations of Tab. 3.1. Below the formulas for the mean, Eq. (3.43), the variance, Eq. (3.44), the skewness, Eq. (3.45), and the kurtosis, Eq. (3.46) of the velocity JPDF can be found.

$$\mu_{pdf} = M_R^1 = \mu_R \tag{3.43}$$

$$\sigma_{pdf}^2 = M_R^2 - (M_R^1)^2 - M_{auto}^2 = \sigma_R^2 - \sigma_{auto}^2 \tag{3.44}$$

$$\nu_{pdf} = \frac{M_R^3 + 2(M_R^1)^3 - 3M_R^1 M_R^2}{\left(M_R^2 - {M_R^1}^2 - M_{auto}^2\right)^{3/2}} = \frac{\nu_R \sigma_R^3}{\left(\sigma_R^2 - \sigma_{auto}^2\right)^{3/2}} \tag{3.45}$$

$$\begin{aligned} \kappa_{pdf} &= \frac{M_R^4 - M_{auto}^4 - 6M_R^2 M_{auto}^2 - 6(M_{auto}^2)^2}{\left(M_R^2 - M_{auto}^2 - M_R^1\right)^2} \\ &= \frac{\kappa_R \sigma_R^4 - \kappa_{auto}\sigma_{auto}^4 - 6\sigma_R^2\sigma_{auto}^2 + 6\left(\sigma_{auto}^2\right)^2}{\left(\sigma_R^2 - \sigma_{auto}^2\right)^2} \end{aligned} \tag{3.46}$$

3.3 Reducing the Influence of Noise

A correlation function determined using standard PIV or ensemble averaging will in general not result in a perfectly smooth function. It always contains noise, which is induced by the measurement devices, the optics of the camera, the pixel sensors, and so on. The noise also strongly depends on the amount of particles illuminated in flow, as they not only contribute to the correlation function but also to the background noise of the image. The method introduced in the previous section relies on the moments of the correlation and the autocorrelation function, which can only be determined by integration. Therefore, any noise contained directly contributes to the moments calculated. To reduce the influence of noise in the integration process one either has to lower the noise level by pre-processing the images or remove the noise surrounding the correlation functions by pre-processing the correlation functions themselves ahead of the integration process.

In the next sections several methods to reduce the noise level of the correlation function by pre-processing the images are addressed. Then the focus lies on correlation functions, and four methods to pre-process the correlation functions ahead of the integration process are discussed.

3.3.1 Image Pre-Processing

Besides others, the noise surrounding the correlation peak originates mainly from the recording process, strong reflections, air bubbles and other non-particle images within the recording, non-homogeneous illumination, and the seeding density. While the influence of random noise originating from the recording process and single errors in the time series are removed by ensemble averaging, noise caused by reflections and inhomogeneous illumination is not removed. A possibility to decrease their influence is to pre-process the images ahead of the correlation process.

Background Removal

A common pre-processing method is the removal of the image background. This lowers the noise level of the correlation functions as any particle image is then only correlated with other particle images but not with background noise. The background noise level, usually called the reference image, can be obtained in several ways: the most common method is to compute a time average of the gray levels at each pixel. Further methods to obtain the reference image can be found in Honkanen and Nobach (2005). For SPE Billy et al. (2004) introduced a local background removal technique, which is combined with a top threshold filter to reduce the influence of outliers on the ensemble averaged correlation function. Their filter rejects all pixels with a gray level that is either lower than the local mean or four times larger.

Intensity Normalization

SPE is also sensible to intensity differences within the time series. Since time-averaged correlation functions are evaluated, correlation functions determined from a brighter image pair than another contribute stronger to the final, time-averaged correlation function. This variation of the light intensity within a time series occurs for example if the seeding density is not constant and/or if the intensity of the laser changes during the image recording. To lower this influence each image can be normalized by its mean intensity. This leads to an equalization of the image intensities within the dataset and therefore to equally weighted correlation functions of the ensemble.

Reflections

An additional source of noise and erroneous correlation functions are reflections at boundaries. Although their influence can be lowered by coating either the boundary or the particles with fluorescent color (Adrian and Westerweel, 2010), or equalizing the refractive indexes of the fluid an the boundary (Hassan and Dominguez-Ontiveros, 2008), in many cases they can not be removed perfectly. To resolve the flow field close to the wall it can be useful to cover the boundary by a mask, as shown e.g. by Theunissen et al. (2008). There, all pixels within the boundary are set to a fixed value, e.g. the mean intensity value, such that they do not contribute to the correlation function.

Particle density

The seeding density also influences the noise level of the correlation function. Usually a combination of particle size and magnification is chosen, such that a single particle image covers about three by three pixels (Adrian and Westerweel, 2010). If the seeding density is large, then the background noise level increases, as many particles are illuminated and diffusely scatter light. This can fairly be solved by background removal. If the number of particles is low on the other hand, also less particles will contribute to the correlation peak, such that a larger amount of images pairs is needed to gain a well defined correlation peak. Chuang et al. (2012) studied the influence of the particle density on the mean bias error and the correlation coefficient. As a result of tests using synthetic images, they suggest for

SPE a seeding density larger than 4.88 % to reduce the influence of background noise on the correlation function.

3.3.2 Correlation Function Pre-Processing

The calculation of the statistical moments of the PDF is very sensitive to the smoothness of the evaluated function, especially if higher order moments are determined. Since these moments depend not only on the maximum position of the correlation peak, but also on the tails of the evaluated function.

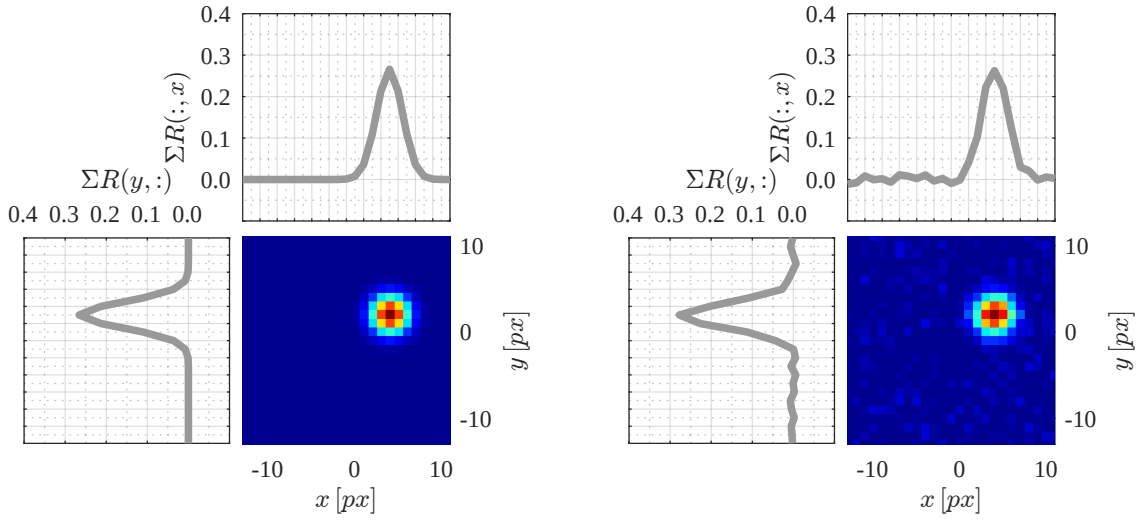

a: correlation function without noise

b: correlation function with artificially added noise

Figure 3.3: Exemplary correlation function and the sums of the function in x- and y-direction which are used to determine the statistics; (a) without noise, (b) with artificially added noise.

In Fig. 3.3 two correlation functions are depicted: the function on the left is a perfectly smooth Gaussian curve, the function on the right is slightly rougher as artificial noise is added. Comparing the sum of all rows, $\Sigma R(:,x)$, two properties can be observed: (1) the correlation peak is positioned at $x = 4\,px$, which leads to a long tail to the left and a very short distance to the right border of the correlation plane; (2) in the noisy correlation function, there are small fluctuations in the tails on both sides of the peak. The same, but with a different position of the peak, can be observed for the sum of all columns $\Sigma R(y,:)$.

If the statistical moments of the smooth and the noisy function, Fig. 3.3 (a) and (b), are determined by integrating either the sum of all rows for moments in the x-direction, or the sum of all columns for the y-direction, the moments of the noisy function will contain an error. The mean values will be underestimated, as the noise on the left of the correlation peak contributes more to the integration function, than the noise on the short right-hand

side of the peak. The variances are also estimated slightly wrongly and an artificial skewness is introduced due to the noise. Therefore, in general not the whole correlation plane is used to determine the centroid of the correlation peak but an extracted region around the peak. Since the result of the integration then strongly depends on the chosen extraction, in standard PIV usually a Gaussian curve is fitted into the peak to determine the position of the maximum in sub-pixel accuracy (Lourenco and Krothapalli, 1995, Fincham and Spedding, 1997).

The new method introduced to determine the moments of the velocity PDF depends on the integration of the correlation and the autocorrelation function. Therefore, one has to consider and lower the influence of noise surrounding the correlation peak. Several methods to extract the peak from the surrounding noise have been tested to check which technique is the best in retrieving the correlation function without changing its characteristics. The basic principle of these methods is described in the following.

Rectangle Filter

As the position of the correlation peak is off the center of the correlation plane according to the displacement of the particles within the time delay Δt between the two recordings, the noise surrounding the peak on the opponent side of the displacement has a stronger contribution, than the noise in the direction of the displacement. Therefore, all values determined by integration are biased in the adjacent direction of the displacement. To overcome this problem, the simplest solution is to extract the correlation peak from the plane by centering a rectangle around its maximum. The size of the rectangle may either be chosen individually with respect to the estimated diameter of the correlation peak or using the shortest distance of the peak to the boundary as side length of the cut-out rectangle. Fig. 3.4 (a) shows the result of the application of this filter on the noisy correlation function of Fig. 3.3. Here the side length of the rectangle was set to be the shortest distance of the correlation peak to the boundary. If the function evaluated contains several maxima, this filter introduces a bias as it draws the rectangle around the absolute maximum. A fact one has to consider, especially for multi modal JPDFs.

Rectangle Filter Including Gaussian Fit

The rectangle filter can be further improved if a two-dimensional Gaussian curve is fitted into the correlation function and the parameters of the Gaussian curve are used to set the size and position of the cut-off rectangle; as used by Scharnowski et al. (2012) to determine the Reynolds stresses and similar to the Gaussian curve fit applied in standard PIV to determine the sub-pixel accuracy. On the one hand this improves the rectangle filter, as it cuts out the correlation peak according to its individual size, on the other hand it can only estimate Gaussian shaped curves and has a high computational effort, due to the iterative fitting process. Fig. 3.4 (b) depicts the noisy correlation function of Fig. 3.3 after the filter was applied. In comparison to the rectangle filter, Fig. 3.4 (a), the cut-out region is smaller, such that not the whole extend of the correlation peak is covered, which will result in a wrong estimation especially of the higher order statistical moments.

Threshold Filter

Another method to reduce the influence of noise is the extraction of the correlation peak applying a cut-off threshold. It is similar to the method of Otsu (1979), which was developed to define a threshold when gray-scale images are transformed into binary images. This is for example used to extract objects from their surroundings. Here, the resulting binary matrix is used to extract the correlation peak. The transformation of the correlation function into a binary matrix using a threshold leads to a matrix with often two to three areas of ones, of which the largest usually contains the correlation peak. Therefore, all smaller areas are rejected and the resulting binary matrix is used to extract the correlation peak by an entry-wise multiplication of the binary matrix and the correlation function (Strobl et al., 2015). In Fig. 3.4 (c) the result of the application of this filter onto the noisy correlation function of Fig. 3.3 is shown. It can be seen that it extracts the correlation peak in an almost circular shape. All values off the correlation peak have been set to zero by the binary matrix applied. The threshold level of this method has to be determined iteratively, as otherwise too much/ too little of the correlation function would be removed. The iteration process ends, when the mean and standard deviation of the correlation function converge. This method is independent of the correlation function's shape but time consuming due to the iteration.

Standard Deviation Filter

This filter determines the standard deviation of one pixel of the correlation function to its neighboring pixels, e.g. $3 \times 3\,px$. The resulting standard deviation will be the largest at the position of the correlation peak, where strong gradients occur; while the standard deviations at the pixels farther away from the maximum are lower and similar to each other. This characteristic can be used to extract the correlation peak, when the standard deviation matrix is transformed into a binary matrix: all positions of a standard deviation lower than the mean of all standard deviations are set to zero and all positions with standard deviations larger than the mean are set to one. An entry-wise multiplication of this binary matrix and the correlation function extracts the correlation peak independently of its shape and is not as time consuming as the methods before as no iteration process is needed. In Fig. 3.4 (d) the noisy correlation function of Fig. 3.3 pre-processed using the standard deviation filter is depicted. In order to further improve the accuracy, the correlation peak was first extracted by a rectangle filter before the standard deviations were determined.

3.4 Summary

In this chapter PIV was described in a mathematical sense, such that a new method to estimate the statistical moments of the velocity JPDF from SPE results could be introduced. This method, which uses the moments of the correlation and the autocorrelation function to determine the moments of the JPDF, depends on the integration of the former two functions. As any image and thus any correlation and autocorrelation function contains noise, the last section of this chapter concentrated on reducing the influence of this noise on the integration process and therefore, on the final result. In the next chapter the new method is tested

on synthetic data. There, also a comparison of the effectiveness of the different correlation function pre-processing methods will be made and it will be shown how this pre-processing reduces the number of image pairs needed to determine the moments of the velocity JPDF at a sufficient accuracy (cf. Section 4.2.3).

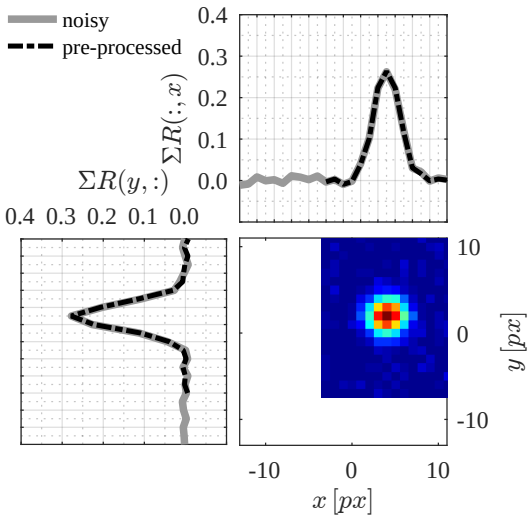

a: Rectangle Filter

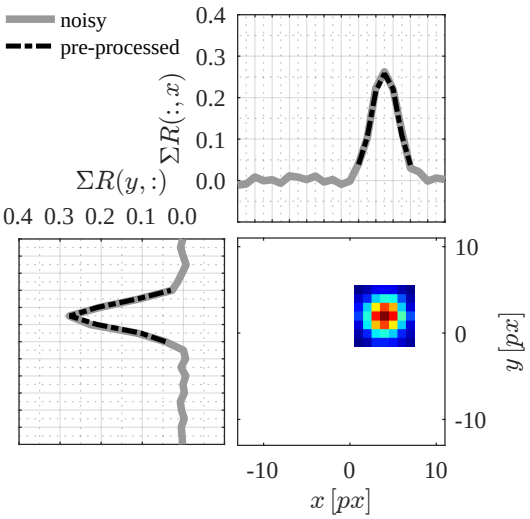

b: Gaussian Fit

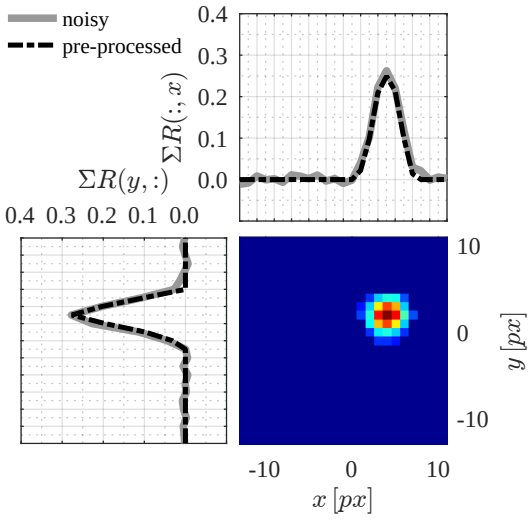

c: Threshold Filter

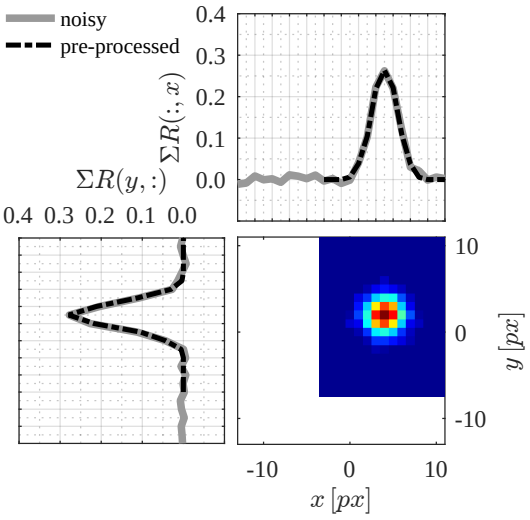

d: Standard Deviation Filter

Figure 3.4: Pre-processed correlation functions and the sums of the function in x- and y-direction in comparison to the sums of the original noisy correlation function.

4 Synthetic Tests

Synthetic images are a good starting point when testing a new method or evaluation routine, as all parameters can be controlled manually. This chapter tests the capacity of the new routine using synthetic datasets. Two different types of synthetic tests were performed: (1) using generic one- and two-dimensional functions and (2) using synthetic image datasets. In the following, both tests are used to show that the new method estimates the statistical moments of any velocity JPDF, independent of its sub-pixel position, diameter and shape.

The chapter starts with one-dimensional tests, where the problems occurring due to the mapping of a continuous function onto a fixed pixel grid are explained. Then it is shown - using generic functions - that the proposed method is able to overcome the shortcomings of the methods published so far. After this, the new method is tested on synthetic images. First the properties of the synthetic images are introduced, then the focus is on the influence of noise on the accuracy of the reconstructed moments, and it is shown how correlation function pre-processing (cf. Section 3.3.2) leads to a significant improvement in accuracy. Finally, the capacity of the new method to estimate the moments of arbitrarily shaped velocity JPDFs is demonstrated and compared to the results of deconvolution. Parts of both sections can also be found in Strobl et al. (2016).

4.1 Generic Functions

Besides first synthetic tests, this section explains errors that might occur when sampling a continuous function on a discrete grid, as it occurs e.g. during the pixelization process, when the continuous particle images are stored on the pixel array of the camera sensor. Furthermore, this section explains how the synthetic functions - correlation, autocorrelation and probability density function - were created and the evaluation routines that were used to reconstruct the moments of the velocity PDF. The section ends with basic tests of the new method, evaluating the capacity of the new method to estimate the statistical moments of PDFs of different widths, sub-pixel positions and shapes in contrast to the result of deconvolution and Gaussian fit.

4.1.1 Errors due to Pixelization

A well-known problem, when sampling a continuous function on a discrete grid, is that the accuracy of the representation depends on the sampling grid spacing. Large grid spacings are unable to represent a function in great detail, while very fine spacings are often impossible. In PIV grid spacing is restricted by pixel size. Fig. 4.1 shows two continuous functions of different widths and their representations when sampled on a grid of identical spacing.

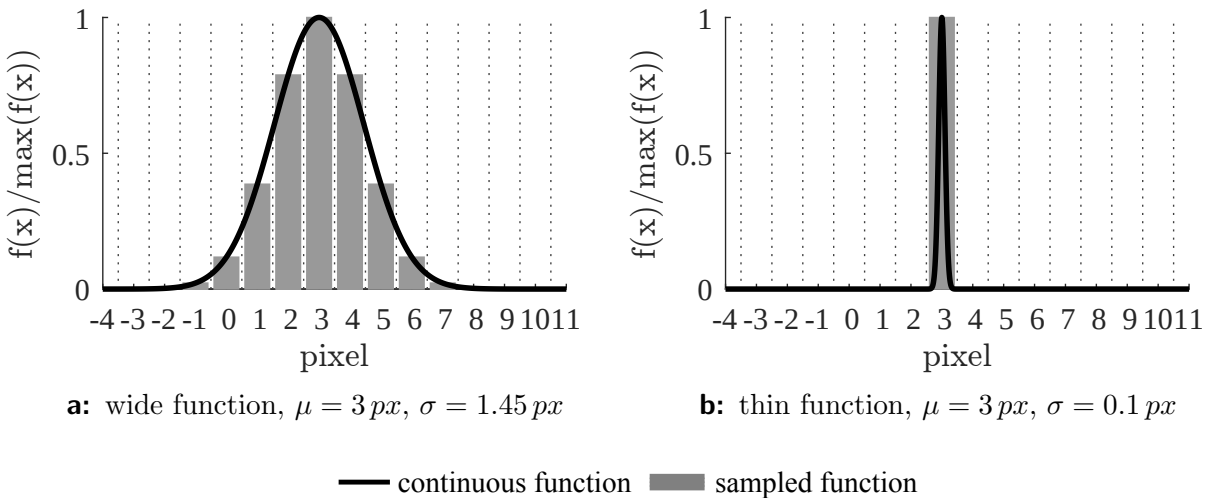

a: wide function, $\mu = 3\,px$, $\sigma = 1.45\,px$

b: thin function, $\mu = 3\,px$, $\sigma = 0.1\,px$

Figure 4.1: Effect of pixel sampling on functions of different widths.

Comparing the left and the right graph, the wider function on the left is represented very well by several bars meeting the continuous function, while the thinner function on the right is represented by a single bar, which is wider than the continuous function plotted on top. If the second moment, i.e. the variance, of both functions is determined and compared to the variance of the continuous function, the wider function meets the continuous function, while the thin function over-predicts the variance. Due to the pixelization, a function thinner than a pixel and still recognized by the sampling process will always cover a whole pixel. A function represented on a fixed grid can, therefore, never be represented narrower than the grid spacing.

An additional problem occurs, when sampling a continuous function not centered with respect to the grid, as can be seen by comparing the functions in Fig. 4.2 to the function in Fig. 4.1(a). First, the mean of both functions in Fig. 4.2 is shifted to $\mu = 3.25\,px$, which is at three-quarters of pixel three, Fig. 4.2(a). Then the position of the mean is shifted to $\mu = 3.5\,px$, the edge between pixel three and four Fig. 4.2(b). Compared to Fig. 4.1(a), where the mean is positioned in the center of pixel three, the discretized function in Fig. 4.2 (a) is slightly skewed, while the function in Fig. 4.2 (b) is symmetric about the mean. An evaluation of the slightly skewed function of Fig. 4.2 (a) would reveal that an artificial skewness is introduced by the sub-pixel position of the mean although the originating continuous function is a non-skewed Gaussian curve. Effects of this behavior for various synthetic correlation functions are assessed in Section 4.1.3.

4.1.2 Generic PDF Creation and Methods Used to Determine the Moments

The correlation functions evaluated were created convolving a given autocorrelation function $A(\mathbf{x})$ and a velocity JPDF. While the autocorrelation function $A(\mathbf{x})$ was always represented by a Gaussian curve centered around the origin, the velocity JPDFs were of various shapes:

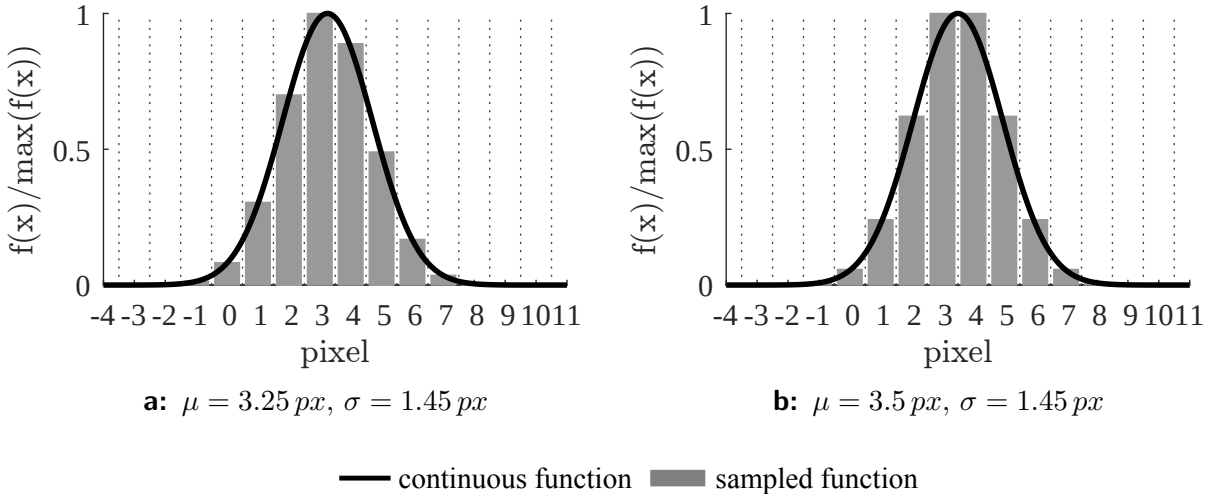

Figure 4.2: Effect of pixel sampling functions with different mean positions.

Gaussian, bimodal and skewed. Note that the functions were sampled on a discrete grid corresponding to the pixel grid of an image, such that instead of continuous functions their spatial counterparts sampled on the pixel grid were convolved and evaluated. The statistical parameters of the functions induced are provided in Section 4.1.3.

Computation of the Moments

The moments compared in the following sections were calculated using Eq. (4.1) for the mean and Eq. (4.2) for all central moments: k corresponds to the order of the moment, e.g. $k = 2$ is equal to the calculation of the variance. All functions $g(x)$ were normalized, such that $\sum g(x) = 1$.

$$M_g^1 = \frac{1}{N} \sum_{i=1}^{N} (x_i \, g(x_i)) \tag{4.1}$$

$$m_g^k = \frac{1}{N} \sum_{i=1}^{N} ((x_i - M_g^1)^k \, g(x_i)). \tag{4.2}$$

Methods Applied to Reconstruct the Moments of the Velocity PDF

In what follows, the capacities of three methods to reconstruct the moments of the induced velocity JPDFs will be compared. These three methods are:

1. Gaussian Fit
   By iteratively fitting a Gaussian curve into the correlation and the autocorrelation function the statistical parameters of the fitted curves were determined. The statistical

moments were then entered into Eq. (3.43) and (3.44) to estimate the moments of the velocity JPDF.

2. Deconvolution
   For this method the correlation function was deconvolved by the autocorrelation function using a common iterative deconvolution method, the Richardson-Lucy algorithm (Richardson, 1972, Lucy, 1974). The implementation provided by Matlab, applying a maximum of 500 iteration steps, was used. The resulting JPDF was then evaluated for its statistical moments using Eqs. (4.1) and (4.2).
3. The method introduced in section 3.2 - referred to in the following as 'Integration'
   Here, the moments of the correlation function as well as of the autocorrelation function were determined using Eqs.(4.1) and (4.2). After that, the moments of the velocity JPDF were calculated using Eqs. (3.43) to (3.46).

4.1.3 Comparison - Capacities of the Reconstruction Methods

The accuracy to compute the statistical moments of the velocity JPDF depends on three factors:

- the width of the JPDFs measured in pixels;
- the position of the mean within a pixel;
- the shape of the JPDF.

Effect of the Spatial Resolution of the JPDF

Considering the errors occurring when sampling a continuous function on a discrete grid (cf. Section 4.1.1), there are two limits for any method reconstructing the statistical properties of the velocity JPDF from the correlation and the autocorrelation functions: A lower limit if the resolution is not sufficient to represent the details of the function, and an upper limit if the discrete domain is too small to cover the whole function. The upper limit can be influenced by using appropriate particles and applying a correlation plane size that covers the whole correlation peak. Whereas, the lower limit is restricted by the maximum possible magnification. Applying this concept to correlation functions and including the fact that these functions are the convolution of the velocity JPDF with the autocorrelation function of the particle image (cf. Section 3.1.4), it can be concluded that the correct reconstruction of the statistical moments of the velocity JPDF must depend on the spatial discretization of the correlation and autocorrelation functions.

Figs. 4.3 (a) and (b) show induced continuous PDFs, the reconstructed PDFs by deconvolution as well as the correlation and autocorrelation functions. The difference between both plots lies in the width of the imposed velocity distributions: On the left the distribution function is wide, $\sigma = 1.75\,px$, on the right the PDF is narrower than a pixel, $\sigma = 0.10\,px$. In order to simplify the comparison the position of the autocorrelation function's maximum was shifted to the position of the mean displacement and all functions were normalized by their maximum.
Focusing on Fig. 4.3 (a), note that all functions cover several pixels and that the correlation

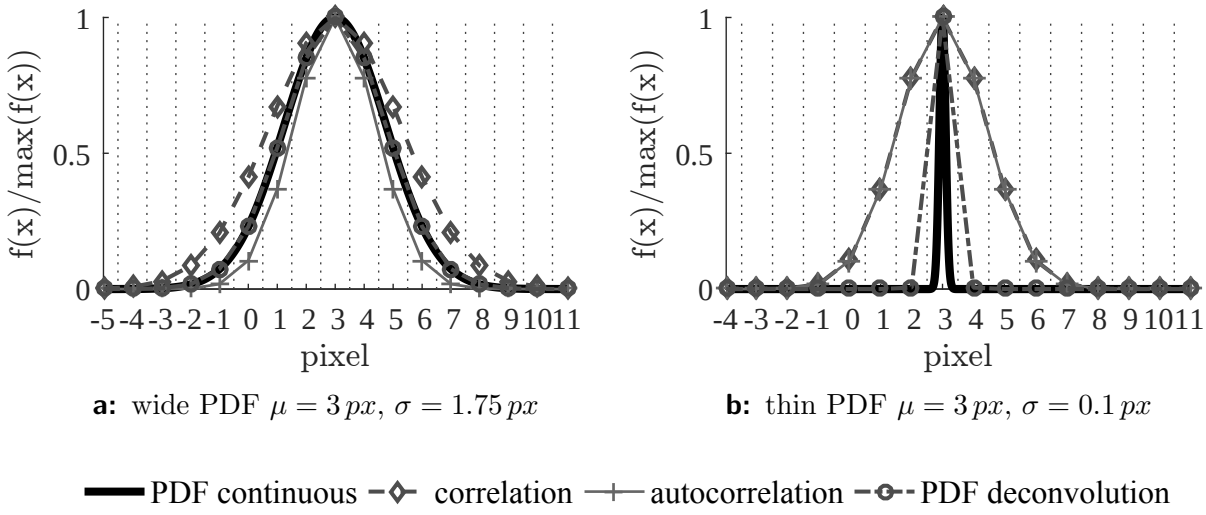

a: wide PDF $\mu = 3\,px$, $\sigma = 1.75\,px$ **b:** thin PDF $\mu = 3\,px$, $\sigma = 0.1\,px$

Figure 4.3: Reconstruction of a wide (a) and a thin (b) PDF by deconvolution.

function is the widest of all curves. This result is in agreement with Eq. (3.44), since the variance of the correlation function is the square root of the sum of the variances of the PDF and the autocorrelation function. Moreover, the PDF reconstructed by deconvolution matches the induced velocity PDF.

Analyzing Fig. 4.3 (b), a different behavior can be observed: the correlation function and the autocorrelation function lie on top of each other, while the velocity PDF reconstructed by deconvolution is wider than the induced distribution function. Zooming in, a small difference between the correlation and the autocorrelation function could be seen. This small deviation is not resolved by the deconvolution algorithm, as the final result of the deconvolution is restricted to the given bin size. Hence, the deconvolution method is not able to recover the statistical parameters of a velocity PDF narrower than a single pixel: deconvolution will always result in a PDF of the size of one pixel, a simple delta peak (cf. Fig. 4.4). The other two methods, fitting a Gaussian curve or determining the moments by integration are on the other hand able to restore this information, as long as they are capable of detecting a difference between the correlation and the autocorrelation function.

Effect of the Sub-Pixel Locations of the Mean Value

As introduced in Section 4.1.1, a function not centered at a pixel or at the border between two pixels will be represented in a skewed way if sampled on the pixel grid. This paragraph examines how each of the three methods performs in reconstructing velocity PDFs located at different sub-pixel positions. There not only the location of the mean was changed, but also the width of the induced Gaussian distribution function. In Fig. 4.4 a comparison of the absolute errors, $\epsilon_{abs} = |m^k_{est} - m^k_{ind}|^{\frac{1}{k}}$, between the estimated and the induced moments with respect to a decreasing standard deviation of the induced JPDF is shown. The figure compares only the errors of statistical moments estimated by deconvolution and integration as Gaussian fit would determine the same results as the integration method as long as only

Gaussian functions and enough iteration steps are used for the fitting process.

Focusing on the results of the mean values, M^1_{PDF}, it can be seen that only the deconvolution method produces an error while the others do not. The error takes place if the standard deviation of the induced PDF is smaller than half a pixel and the sub-pixel position of the mean is between the center of the pixel and the edge, $\mu_x = 3.25$. This happens as deconvolution is only able to restore a function in the same grid spacing as the functions entering the deconvolution process. A function with its peak at this intermediate pixel position will be artificially skewed when sampled on a fixed grid and narrower than the grid spacing.

Concentrating on the standard deviations, ${m^2_{PDF}}^{1/2}$, again errors occur in the moments estimated by deconvolution for standard deviations below half a pixel. In this case errors occur if the mean is positioned at the center of the pixel, $\mu_x = 3.0\,px$, and at three quarters, $\mu_x = 3.25\,px$. Here, the errors increase linearly as the standard deviation of the induced PDF also reduces linearly. This is again due to the fact that no deconvolution is able recover a signal smaller than the spacing of the originating signals.

Comparing the third moment, ${m^3_{PDF}}^{1/3}$, the deconvolution method is not able to remove the artificially added skewness if the sub-pixel position of the mean is between the pixel's center and the edge, $\mu_x = 3.25\,px$. Unlike the errors in the first moment, here the deconvolution method appears to always introduce an error for this sub-pixel position independently of the standard deviations of the induced PDF. In the fourth moment, ${m^4_{PDF}}^{1/4}$, deconvolution also results in errors, for standard deviations smaller than about $0.75\,px$. In contrast to the second moment, ${m^2_{PDF}}^{1/2}$, also the position at the edge between the pixels leads to an error.

The method developed in Section 3.2 does not suffer from any of these errors, as the autocorrelation function is well represented on the grid spacing, and thus the correlation function is also well represented.

Capacity to Recover PDFs of Various Shapes

In a final step a test was performed to determine how the described methods are able to estimate the moments of non-Gaussian shaped velocity distributions. Therefore, three two-dimensional velocity JPDFs were created and convolved with a two-dimensional autocorrelation function, with a standard deviation of $\sigma_{auto} = 1.0821\,px$. The distribution functions are a Gaussian bell curve, see Tab. 4.1, a skewed distribution, see Tab. 4.2 and a bimodal distribution, see Tab. 4.3. Tabs. 4.1 to 4.3 contain the moments recovered by the different methods as described in Section 4.1.2. For the Gaussian curve fitting, the third central moment was set to zero and the fourth central moment to three times the standard deviation to the power of four, since a Gaussian curve has zero skewness and a flatness of three.

Comparing the results in Tab. 4.1, the Gaussian curve is reconstructed very well by all three methods. The skewed JPDF, Tab. 4.2, is precisely estimated by deconvolution and the integration method, while the Gaussian fit already suffers larger errors in the skewed direction due to its restriction to a Gaussian shape.

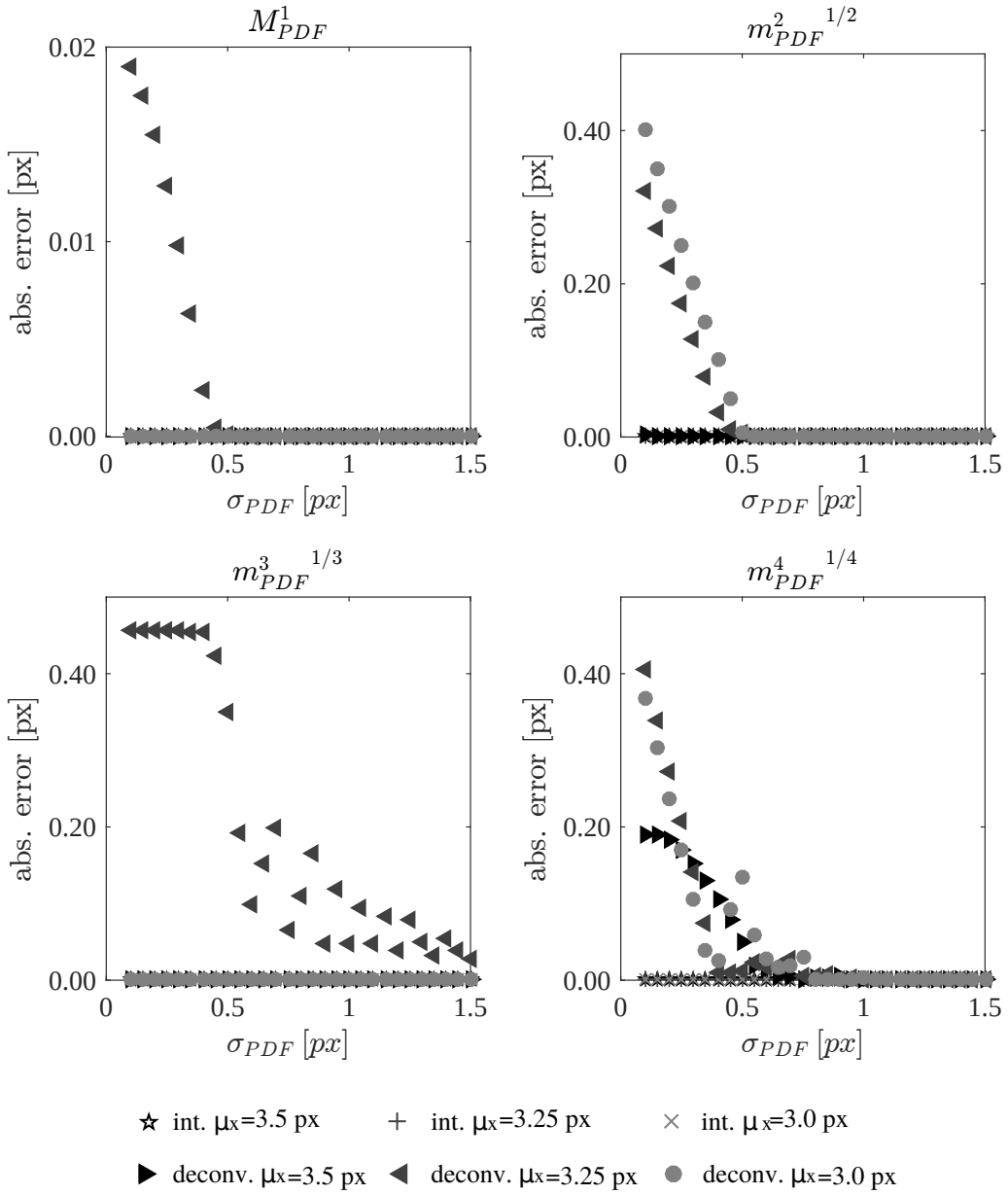

Figure 4.4: Comparison of the absolute errors, when reconstructing velocity distributions using either deconvolution, or the method introduce in section 3.2.

The largest deviations occur for the bimodal distribution, Tab. 4.3. While the integration method is still able to recover all moments up to the fourth digit, errors occur in both the Gaussian fit and the deconvolution. The errors of the Gaussian fit again occur because of the Gaussian shape of the fitted curve, therefore only the mean values are in the range of the induced PDF. The deconvolution method particularly shows errors in the third and fourth central moments, which occur as the means are not positioned at the center or the edge of the pixel grid and thus appear skewed when sampled on the pixel grid.

	Induced	Gaussian - Fit	Deconvolution	Integration
M_x^1	4,3000	4,3000	4,3000	4,3000
M_y^1	4,3000	4,3000	4,3000	4,3000
m_x^2	1,0000	1,0070	1,0000	1,0000
m_y^2	1,0000	1,0070	1,0000	1,0000
m_x^3	0,0000	0,0000	0,0000	0,0000
m_y^3	0,0000	0,0000	0,0000	0,0000
m_x^4	3,0000	3,0000	2,9984	3,0000
m_y^4	3,0000	3,0000	2,9984	3,0000

Table 4.1: Induced and reconstructed parameters of a two-dimensional Gaussian JPDF

	Induced	Gaussian - Fit	Deconvolution	Integration
M_x^1	2,5621	2,4038	2,5621	2,5621
M_y^1	3,0000	3,0000	3,0000	3,0000
m_x^2	1,5599	1,4228	1,5599	1,5599
m_y^2	2,2500	2,2563	2,2500	2,2500
m_x^3	1,6480	0,0000	1,6476	1,6480
m_y^3	0,0000	0,0000	0,0000	0,0000
m_x^4	8,9106	6,0731	8,9079	8,9106
m_y^4	15,1875	15,2727	15,1875	15,1875

Table 4.2: Induced and reconstructed parameters of a two-dimensional skewed JPDF

	Induced	Gaussian - Fit	Deconvolution	Integration
M_x^1	0,6231	0,6187	0,6230	0,6231
M_y^1	1,2483	1,2416	1,2482	1,2483
m_x^2	0,7772	0,8308	0,7758	0,7772
m_y^2	1,9531	2,6211	1,9506	1,9531
m_x^3	0,0123	0,0000	0,0217	0,0123
m_y^3	0,0255	0,0000	0,0287	0,0255
m_x^4	1,5418	2,0707	1,4924	1,5418
m_y^4	6,5614	20,6105	6,4555	6,5614

Table 4.3: Induced and reconstructed parameters of a two-dimensional bimodal JPDF

This comparison of three methods to estimate the statistical moments of three different induced velocity JPDF - Gaussian fit, deconvolution and integration - shows that using generic functions only the integration method is able to determine the statistical moments velocity JPDFs regardlessly or their shape and spatial position. While Gaussian fit is restricted to Gaussian shaped curves and deconvolution adds errors to the third and fourth central moment if the JPDF is sampled artificially skewed on the pixel grid due its spatial position.

4.2 Synthetic Images

In the following synthetic images will be evaluated using the integration and the deconvolution method. In a first step the properties of the images generated are described. The algorithm used to determine the ensemble averaged correlation and the autocorrelation function is explained. The last section discusses the results from synthetic image test cases with respect to the influence of correlation function pre-processing, the image noise level, the number of samples contributing to the correlation function, and differently shaped PDFs.

4.2.1 Image Generation

All synthetic images created have a size of $128 \times 128\,px$. The particles are assumed to be at the same depth of the light sheet and in focus, such that there is no out-off-plane loss and no change in the representation of a particle image due to a different location in depth. The particle images themselves are each approximated by a two-dimensional Gaussian function (cf. Section 3.1.1). To be able to integrate the particle image intensity over pixels, this function is estimated by the error function and integrated along the pixels covered by the particle.

The positions of the particles were randomly distributed in the first image and all shifted by the same displacement vector in the second image. Therefore, variations of the simulated displacements within one image pair only occurred due to the pixelization process, which is represented by the integration of the error function over the pixel bins and the transformation of the initial double precision pixel bin values into eight bit integer values. Randomly varying velocity vectors were used from image pair to image pair produced by a random generator, which gave the desired JPDF. The particle size was held constant at $d_e = 3\,px$ and the seeding density was set to $N_{ppp} = 0.02$. Furthermore, 15 000 image pairs were generated. This results in 1 050 particle samples per pixel using the source density N_s, Eq.(4.3), including a corrected effective particle diameter $d_{e,corrected} = \frac{d_e}{\sqrt{2}}$, as proposed by Avallone et al. (2015).

$$N_s = \frac{\pi d_{e,corrected}^2}{4} N_{ppp} \tag{4.3}$$

Additionally, three different velocity JPDFs were evaluated: Gaussian shaped, bimodal and skewed (cf. Fig. 4.5 (a) to (c)). The properties of the induced velocity JPDFs are provided in Tabs. 4.1 to 4.3. They were determined integrating the imposed JPDFs with a grid spacing

equivalent to the pixel bin size of the synthetic images. Moreover, random Gaussian white noise, with a zero mean and a standard deviation of ten percent of the mean image intensity, was employed on the images if not stated differently.

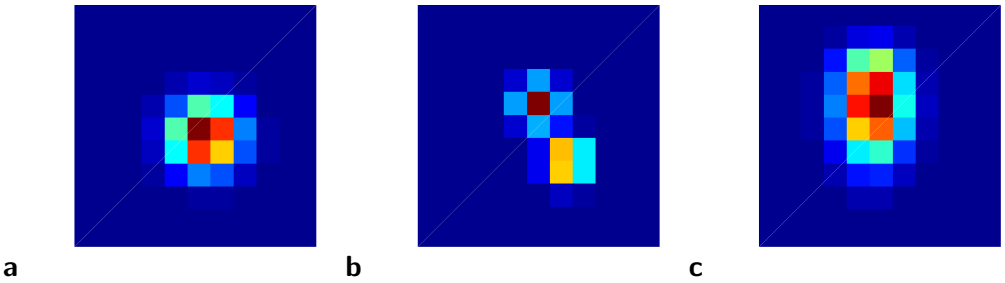

Figure 4.5: Synthetically generated distribution functions sampled on the pixel grid: Gaussian (a); bimodal (b) and skewed (c).

4.2.2 The Algorithm Applied

Fig. 4.6 shows a schematic sketch of the algorithm used to determine the moments of the correlation function. This algorithm can be adopted easily for the autocorrelation functions if the consecutive image, I_2, is replace by I_1. The algorithm consists of two main parts: (1) a loop through the image dataset including the calculation of the instantaneous correlation functions and (2) the evaluation and post-processing of the time-averaged correlation functions.

The correlation functions[1] were computed for a plane sized $25 \times 25\,px$ around each point of correlation, $\mathbf{x}$, using Eq. (4.4). This plane size is large enough to cover all details of the velocity JPDFs induced, and still keeps the computation time low. The two-point correlations at each position $\mathbf{x}$ of the image were performed in two directions: forwards, correlating the first $I_1(\mathbf{x}, i)$ with the second image $I_2(\mathbf{x}', i)$, and backwards, correlating the second image $I_2(\mathbf{x}, i)$ with the first $I_1(\mathbf{x}', i)$, to double the number of samples (Avallone et al., 2015). This was carried out for each of the 15 000 image pairs and then averaged over time, leading to 2 100 samples contributing to the correlation peak.

$$R(\mathbf{x}, \mathbf{x}') = \sum_{i=1}^{N_{images}} I_1(\mathbf{x}, i) I_2(\mathbf{x}', i) \tag{4.4}$$

The correlation functions were then normalized, see Eq. (3.28), to determine the correlation coefficient and to reduce the influence of inhomogeneities of the image series evaluated. After this step, the functions were filtered (cf. Section 3.3.2), and their statistical moments were computed by integration using Eqs. (4.1) and (4.2). These moments of the correlation and autocorrelation functions were then entered into Eqs. (3.43), (3.44), (3.45), (3.46) to determine the moments of the velocity JPDF.

[1]Note that in contrast to Fig. 4.6, no filtering was applied on the synthetic images.

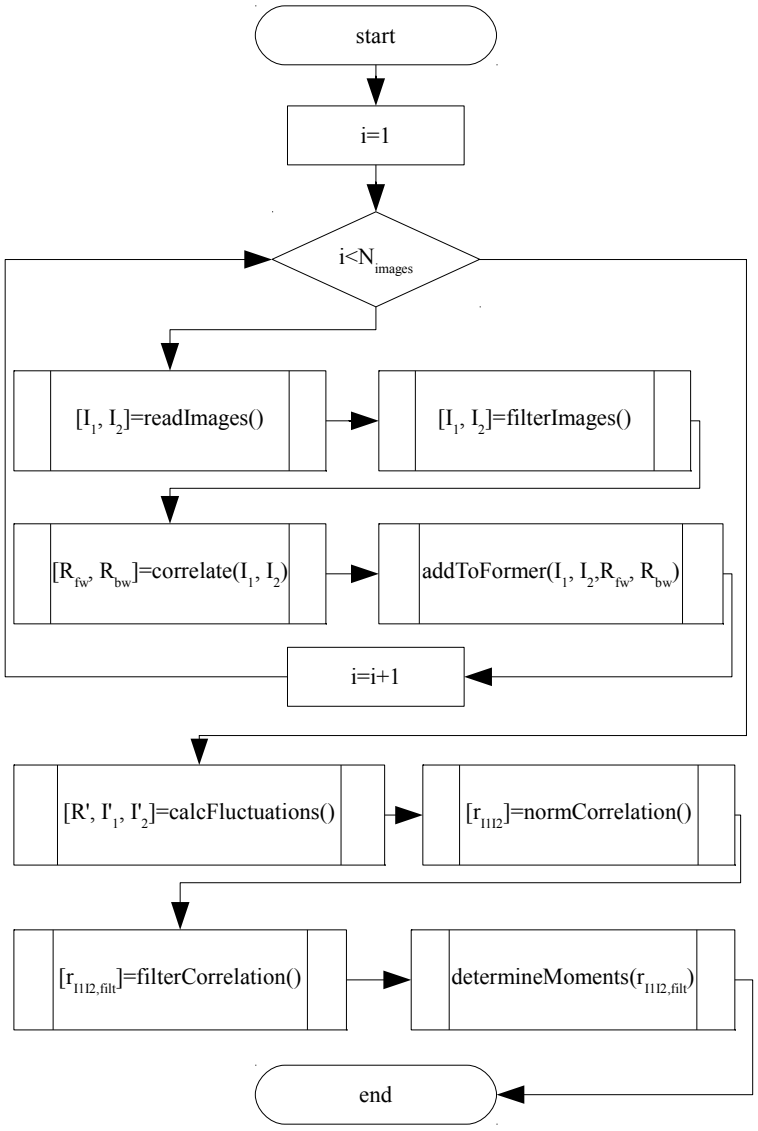

Figure 4.6: Schematic sketch of the algorithm applied to compute the statistical moments of the correlation function. Exchanging the second image by the first, leads to the computation of the statistical moments of the autocorrelation function.

4.2.3 Pre-Processing the Correlation Function

In Section 3.3.2 four different correlation function pre-processing methods to remove the noise surrounding the peak were introduced:

- Rectangle Filter;
- Rectangle Filter including Gaussian Fit;
- Threshold Filter;
- Standard Deviation Filter.

In what follows, these four methods are applied to correlation functions, determined using the skewed velocity JPDF, see Tab. 4.2, to demonstrate how pre-processing improves the accuracy of the reconstructed statistical moments. Therefore, the results of the first four moments determined applying the pre-processing are compared to the results determined without pre-processing. Naturally, the error level increases as the order of the moment increases and decreases as the number of evaluated samples increases. I will compare the development of the Root Mean Square Deviation (RMSD) as the number of images evaluated increases. The calculation of this error is provided in Eq. (4.5).

$$RMSD = \sqrt{\frac{1}{N}\sum_{j=1}^{N}\left(m_{est,i}^{k} - m_{ind}^{k}\right)^{2}} \tag{4.5}$$

$m_{est,i}^{k}$ denotes the k-th moment estimated at position i, m_{ind}^{k} the induced k-th moment and N the number of pixels j evaluated. The induced moments were determined integrating the pixel-sampled induced function (cf. Section 4.1.2).
Fig. 4.7 shows the errors reconstructing the moments of the correlation function for the different pre-processing methods. In all four plots the evaluation without the pre-processing, marked by a '+', contains the largest errors, as the noise surrounding the correlation peak is the largest in this case. The improvement made by centering the correlation peak by cutting a rectangle around the maximum can be seen following the '□'-marked curves in Fig. 4.7. The other three methods all increase the accuracy of the recovered moments. Both time consuming methods, cutting a rectangle with a side length determined by the width of a Gaussian curve fitted into the correlation peak, '◁'-markers, and removing the noise by cutting off everything below a threshold value, '▷'-markers, improve the accuracy of the reconstructed moments. The threshold method is always slightly better than the fitting method. Although both methods lower the error noticeably they also stagnate at a almost constant error level, while the method utilizing the standard deviation filter still shows an improvement as the number of images evaluated increases. It consistently shows the smallest errors of all methods for more than about 8 000 time steps, which corresponds to about $1,150$ samples contributing to the correlation peak. Consequently, the standard deviation filter will be applied in all evaluations presented in the following.

4.2.4 Noise

As shown before, there is a strong influence on the accuracy of the estimated moments by the noise level surrounding the correlation peak. This noise stems from two different sources, the noise contained in the images themselves and the noise caused by insufficient statistics due to a small number of samples contributing to the correlation peak. In the next paragraphs the influence of the image noise level and the number of samples evaluated on the accuracy of the recovered moments is examined.

The synthetic images analyzed so far all contain a random Gaussian white noise with zero mean and a standard deviation of ten percent of the mean image intensity. In Fig. 4.8 the development of the RMSD for three different noise levels, ten percent of the mean intensity,

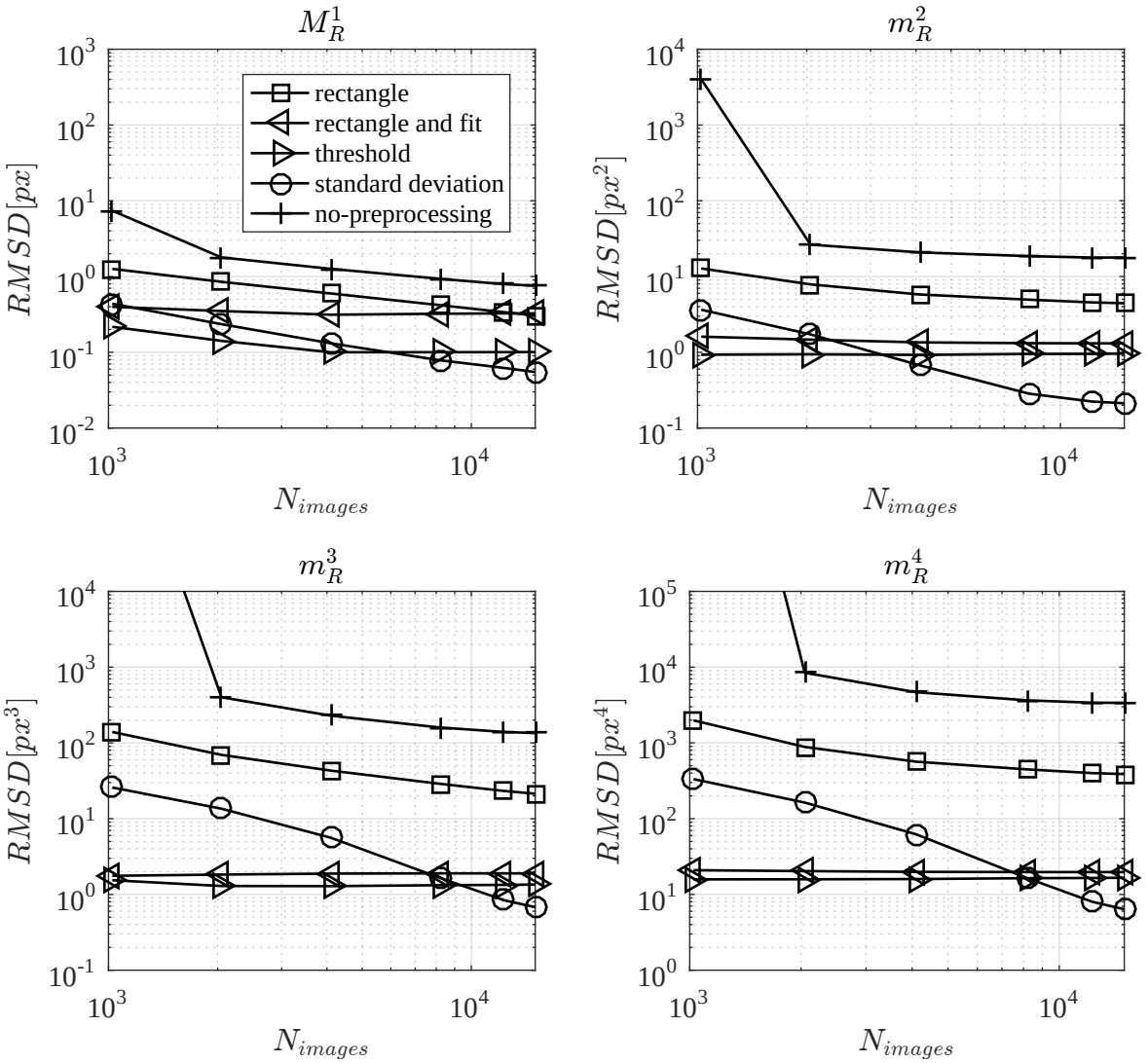

Figure 4.7: Development of the RMSD of the first four moments of the skewed correlation function depending on the different pre-processing techniques applied (cf. Section 3.3).

five percent of the mean intensity and no noise at all is shown. This noise level test was performed for the Gaussian shaped velocity distribution. With an increasing number of evaluated image pairs the error reduces. Comparing the errors of different noise level images, it can be observed moreover that a lower noise level leads to smaller errors if only a few thousand images are evaluated.

For an increasing number of images assessed, it can be seen that the errors approach each other. For the second moment the noisier images even seem to be recovered better than the image without noise. For the fourth moment, very soon a constant error level is reached if there is no artificial image noise present, which is related to the pre-processing of the correlation function. The noisier images meet this error level if a larger number of images is evaluated. As the noise level of the ensemble averaged correlation functions determined using noisy images approaches the noise level of the ensemble averaged correlation functions

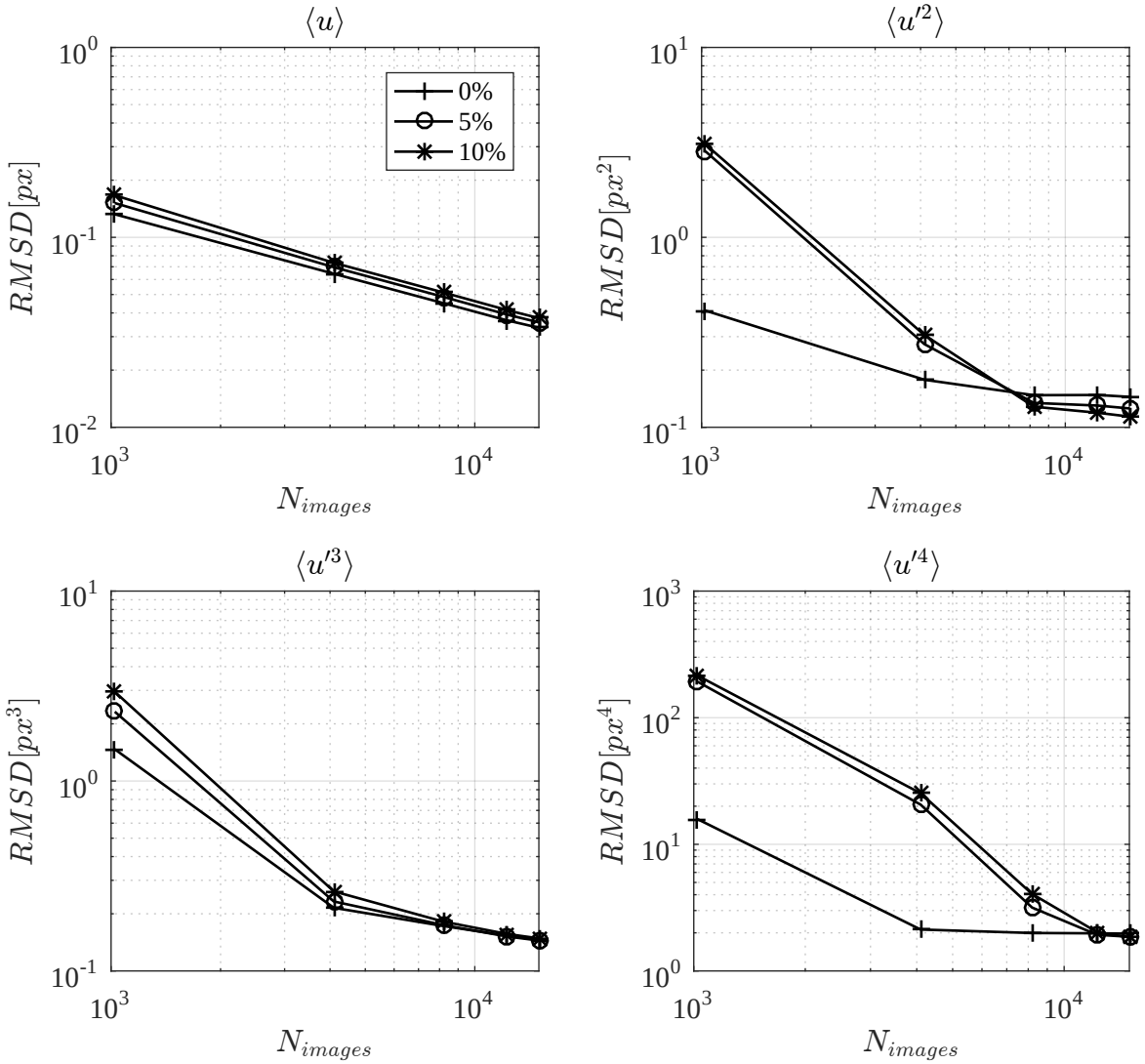

Figure 4.8: Development of the RMSD of the first four moments reconstructing the moments of the induced Gaussian shaped JPDF depending on the different noise levels of the images.

determined using images without noise - but a lower number of samples - the resulting errors also become similar. The second and third moments show the same behavior, which leads to the conclusion that the correlation function pre-processing is only able to remove the error of insufficient statistics or image noise up to a certain extent before it introduces an error itself as parts of the correlation function are falsely considered as noise and are removed.

In a next step the influence of the number of samples contributing to the correlation peak is investigated. Therefore, the number of images analyzed is converted into the corresponding number of samples per pixel. A set of 15 000 image pairs was evaluated, which corresponds to 2 100 samples contributing to the correlation peak at a single pixel. This is a small number if also higher order moments shall be evaluated. On the other hand this number is large if compared to the sample count of real PIV data. The images analyzed in Chapter 5 only include about 195 samples per pixel in a set of 27 000 image pairs. In order to increase

the number of samples contributing to the correlation function, neighboring functions were averaged. Starting with an average of 5×5 correlation functions, up to 15×15 functions were averaged. According to the particle density this would lead to 470 000 samples. As all particles of the synthetic images were moved by the same shift in each image pair, the same sample will be counted twice or even three times due to the size of a particle image. Therefore, the number of samples was lowered for the averaged values, such that they form a straight line, as can be seen in Fig. 4.9. There the development of the RMSD of the first four moments of the skewed velocity JPDF is shown.

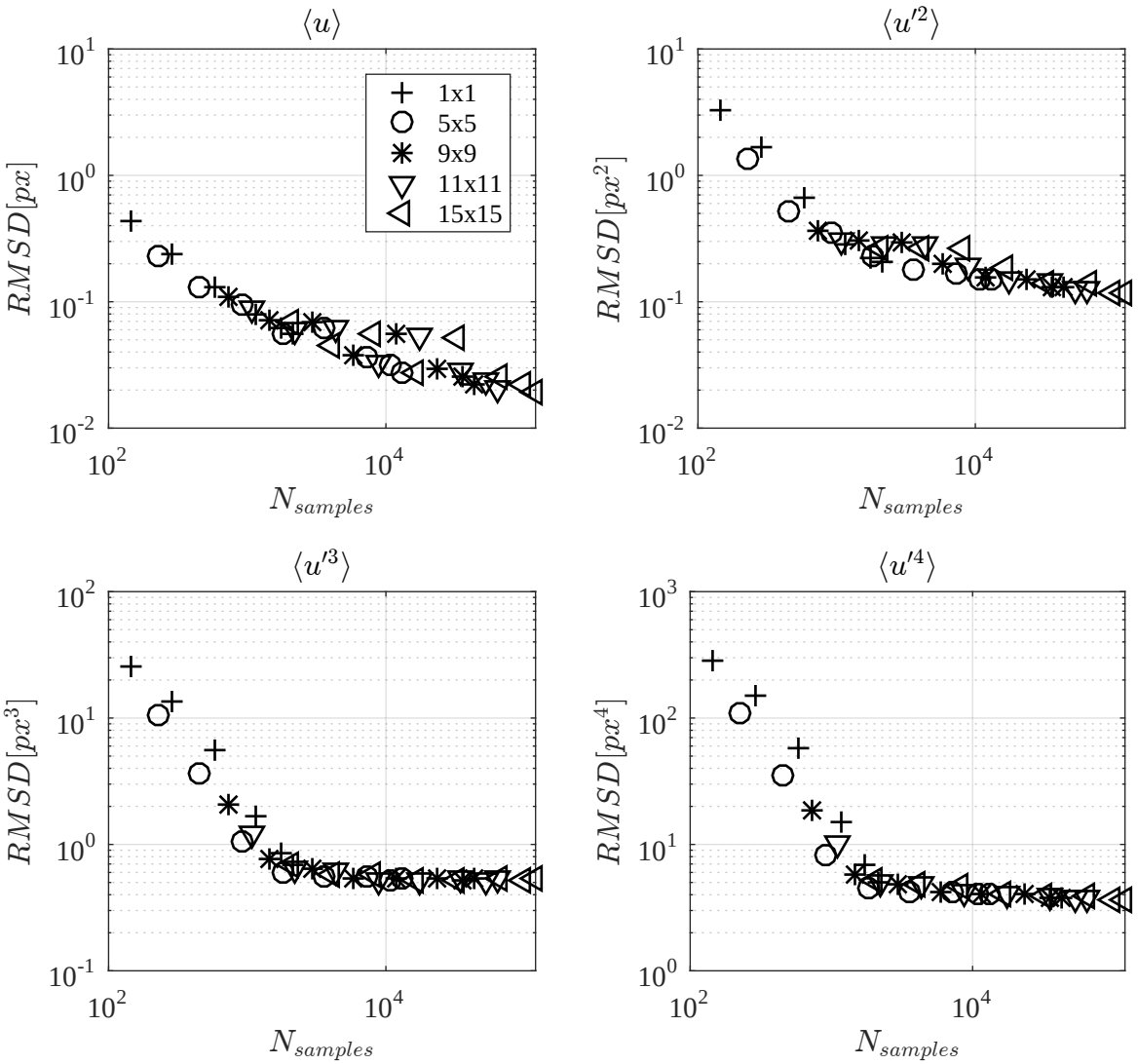

Figure 4.9: RMSD estimating the first four moments of the skewed velocity JPDF for an increasing number of samples due to correlation function averaging.

Note that, as one expects, the error decreases with an increasing number of samples, but that again a saturation takes place at about 2 000 samples, especially for the moments of third and fourth order. This is due to the pre-processing of the correlation functions and can be observed earlier in the higher order moments as they are more sensitive to the pre-processing.

4.2.5 Comparison to Deconvolution

In what follows, the errors occurring when estimating the moments of three different induced velocity JPDFs: Gaussian, bimodal and skewed shaped, are investigated. For that reason two methods: the integration method and the deconvolution method (for details cf. Section 4.1.2) are compared. All functions are filtered by a standard deviation filter (cf. Section 3.3.2) before they are statistically evaluated. The statistical moments of the induced velocity JPDFs can be found in Tabs. 4.1, 4.2, 4.3.

It was shown in the previous section that the method is not only sensitive to image noise but also to noise resulting from insufficient statistics. In Fig. 4.10 the development of the RMSD with respect to an increasing number of samples for a Gaussian, bimodal and skewed shaped velocity distribution is shown. To raise the number of samples, 15×15 correlation functions were averaged before the moments were determined.
The errors decrease with an increase of samples contributing to the correlation peak, although some reach a plateau, especially for the third and fourth moment. Again, this is due to the pre-processing of the correlation and the autocorrelation function. Comparing the results of the deconvolution process, gray curves, to the integration method, black curves, there is no significant difference in accuracy except for the fourth moment of the bimodal distribution. Here, the deconvolution algorithm seems to reconstruct parts of the bimodal distribution that were removed by the correlation function pre-processing, and are not recovered by the integration method. It has to be noted that all functions were pre-processed before the moments were determined, such that the deconvolution method benefits from this pre-processing in the same manner as the integration method (Strobl et al., 2016).

4.3 Summary

Summarizing the results of the synthetic tests it was found that the method introduced in Section 3.2, which estimates the statistical moments of the velocity JPDF using the moments of the correlation and autocorrelation function, is in general applicable. Furthermore, it was shown that in contrast to the other methods found in the literature, Gaussian curve fit (Scharnowski et al., 2012) and iterative deconvolution (Scharnowski and Kähler, 2013), this method is able to recover the moments of arbitrarily shaped velocity JPDFs of any diameter and sub-pixel position as long as the autocorrelation function of the particle image can be represented by the pixel grid spacing.

Moreover, it was demonstrated that pre-processing the correlation function is a useful tool to increase the accuracy, when evaluating noisy correlation functions, independent of the method used. But the pre-processing has to be handled with care as at some point a constant error will occur if too much information of the correlation function is cut-off. Due to the character of the moments this happens earlier for moment of higher order, although the error in the fourth moments has been reduced by a factor of $10^3\,[px^4]$ by the pre-processing.

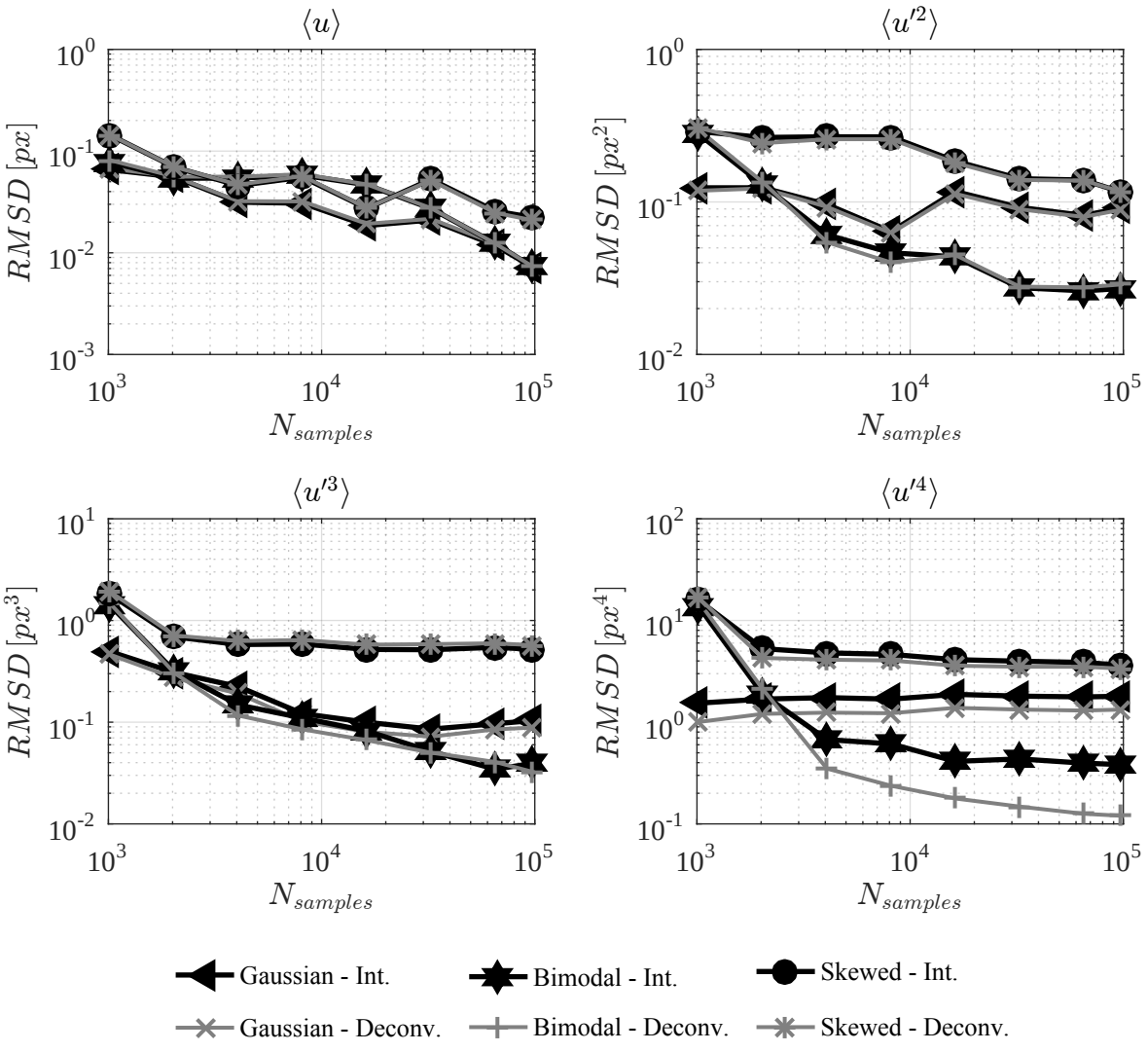

Figure 4.10: A comparison of the RMSD estimating the first four moments of three different velocity JPDFs for an increasing number of samples due to 15×15 correlation function averaging using either deconvolution, grey lines, or the method introduced in section 3.2, black lines.

5 Application to a Dataset of a Flow in Front of a Cylinder Mounted on a Flat Plate

In this chapter the application of SPE on a PIV dataset recorded in front of vertical cylinder mounted on a flat plate is discussed. The first section provides a short introduction to the flow case, addressing the main characteristics and the motivation investigating this case using SPE. Then the experimental set-up and the properties of the dataset are described. In the last section the results are presented and analyzed. The discussions of the mean velocities, Reynolds stresses and higher order moments are mainly taken from Strobl et al. (2016). It is complemented by a comparison of the SPE results to those of a standard $16 \times 16\,px$ PIV evaluation of the same dataset (Jenssen et al., 2016a) and a Large Eddy Simulation (LES) of the same flow case (Schanderl and Manhart, 2016). Furthermore, profiles in the near-wall region and wall shear stresses are discussed and the shape of correlation functions is compared to the shape of velocity PDFs listed in the literature.

5.1 Description of the Flow Case

The configuration of a flow around a vertical cylinder mounted on a flat plate is a common engineering problem. It can be found in mechanical engineering as well as in civil engineering. In the latter this flow case has been studied to gain a deeper understanding of the scouring processes at bridge piers (Melville and Raudkivi, 1977, Dargahi, 1989, Roulund et al., 2005, Pfleger, 2011), which have led to several bridge failures in the past (Imhof, 2004).
In the experiment evaluated here, the focus is on the region upstream of the cylinder, where the horseshoe vortex develops and wraps around the cylinder forming the eponymous horseshoe shape. This upstream region is characterized by:

- a pressure gradient in vertical and streamwise direction caused by the cylinder blocking the cross-section;
- a flow separation zone, in which the horseshoe vortex forms and strong secondary flows occur;
- a bimodal behavior of the vortex system, which periodically moves in streamwise direction (Devenport and Simpson, 1990);
- a large range of scales.

Several studies at various Reynolds numbers investigating this vortex system, especially in the symmetry plane upstream of the obstacle, have been reported in the literature (Dargahi, 1989, Devenport and Simpson, 1990, Paik et al., 2007, Escauriaza and Sotiropoulus, 2011,

Apsilidis et al., 2015, Schanderl and Manhart, 2016). Fig. 5.1 depicts the main structures described in the literature.

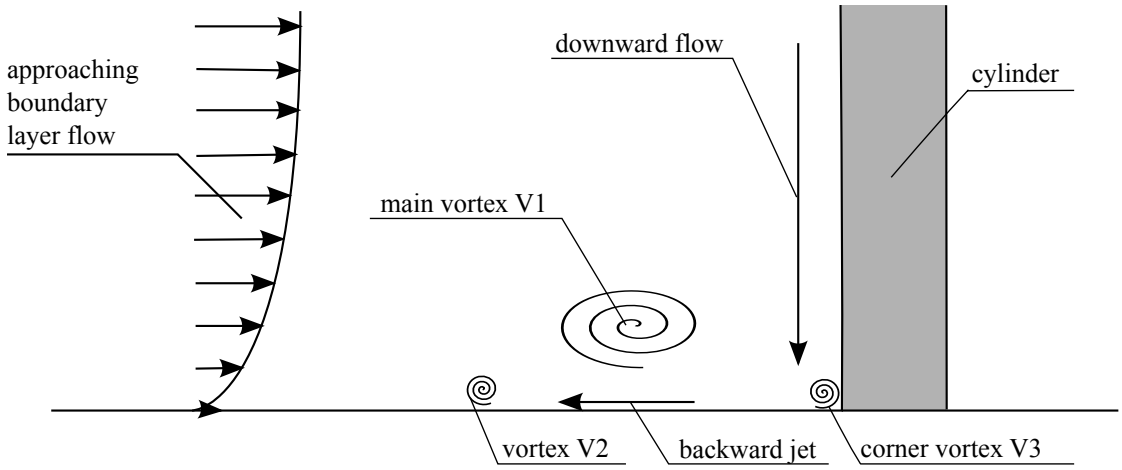

Figure 5.1: Flow structures in the symmetry plane upstream of a vertical cylinder mounted on a flat plate.

In front of the cylinder the incoming flow is deflected downwards parallel to the cylinder. Approaching the bottom plate, main parts of the flow turn backwards and move upstream, while minor parts are pulled towards the cylinder and form the corner vortex V3 at the junction between the cylinder and the bottom plate. Parts of the backward directed flow contribute to the horseshoe vortex V1 upstream of the cylinder, while another part passes this vortex at the bottom plate in form of a backward directed jet. This jet penetrates the incoming flow and forms an additional vortex V2. Flow visualizations of Dargahi (1989) as well as recent time resolved results of Apsilidis et al. (2015) show that the whole vortex system emerges and decays periodically as vortex V1 is moving in streamwise direction.

The vortex system undergoes interesting dynamics, which were first described by Devenport and Simpson (1990), who analyzed the flow around a wing profile at $Re = 115\,000$. They detected two different flow modes in their Laser Doppler Anemometry (LDA) and hot-wire results: the *backflow mode*, which is the same as shown in Fig. 5.1; and the *zero-flow mode*, in which the backward directed jet below vortex V1 is not present, but instead an upward directed jet which directly contributes to vortex V1, such that vortex V1 is positioned closer to the obstacle. This behavior leads to bimodal and/or skewed velocity JPDFs in streamwise and wall-normal direction (Devenport and Simpson, 1990, Paik et al., 2007, Kirkil and Constantinescu, 2015, Apsilidis et al., 2015).

The vortex system also influences the wall shear stress distribution, which is directly connected to the scouring process. To determine the wall shear stress, τ_w, besides the dynamic viscosity of the fluid, μ_{fluid}, the velocity gradient at the wall is needed, Eq. (5.1). Applying

a LES, Schanderl and Manhart (2016) showed that a too coarse spatial resolution leads to an underestimation of the wall shear stresses. They demonstrated that a spatial resolution in wall-normal direction of $\Delta y^+ \lesssim 3$, is needed in order to determine the correct magnitude of the wall shear stress. At the Reynolds number of the dataset evaluated this corresponds to a wall distance of $\frac{D}{1000}$ or $100\,\mu m$

$$\tau_w = \mu_{fluid} \frac{du}{dy}\bigg|_{y=0} \tag{5.1}$$

The discussed flow characteristics, bimodal and skewed velocity distributions, the required high spatial resolution, especially close to the wall, but also the large dynamic range of the overall flow structures in front of the cylinder, make this flow case a challenging test to show the capacities of the new SPE evaluation routine introduced in the previous chapters.

5.2 Experimental Set-Up

The experiment was conducted by Ulrich Jenssen in the Hydromechanics laboratory at the Technische Universität München. A cylinder of diameter $D = 0.1\,m$ was mounted on a flat plate in the symmetry plane of a $1.17\,m$ wide water channel. The water level, y, was $0.15\,m$ at a flow rate $Q = 0.0685\,m^3/s$, which results in a Reynolds number of $Re = 39\,000$ with respect to the bulk velocity of the approaching flow, $u_{bulk} = 0.39\,m/s$, and the diameter of the cylinder D. The water level was controlled by a sluice gate downstream of the measurement area, and the flow rate was measured by a magneto-inductive flow meter. A flow straightener was installed at the inlet of the water channel, such that the turbulent free surface flow developed naturally over a distance of $200\,D$ before it met the cylinder. Additional details on the water channel can be found in Schanderl et al. (2016).

Fig. 5.2 illustrates the measurement set-up in front of the cylinder. A sheet of acrylic glass was positioned on the water surface in front of the cylinder to suppress surface waves introduced by the interaction of the fluid and the cylinder. These waves would change the angle of refraction, and thus the laser beam would not enter the water perpendicular to span the light sheet needed for PIV. Numerical simulations and experiments have shown that there is only marginal influence of this plate on flow structures in the near-wall region examined (Alfaya, 2016).

The light sheet, created by a $532\,nm$ Nd:YAG-Laser, had a thickness of $\Delta z = 2\,mm$ and was positioned in the symmetry plane of the flume. A CCD-camera with a resolution of $2048 \times 2048\,px$ was used to record the images at a sampling rate of $7.25\,Hz$. The magnification factor achieved, using a focal length of $f = 105\,mm$ and a f-number of 2.8, was $47.5964\,\mu m/px$ or $4.8 \cdot 10^{-4} D$. In total 27 000 image pairs were recorded. The recording process was split into 18 recordings of 1 500 image pairs due to limitations of the computer capacity. In between the recordings particles accumulating at the bottom plate were removed to reduce light reflections at the wall. The particles used to resemble the fluid's motion were hollow glass

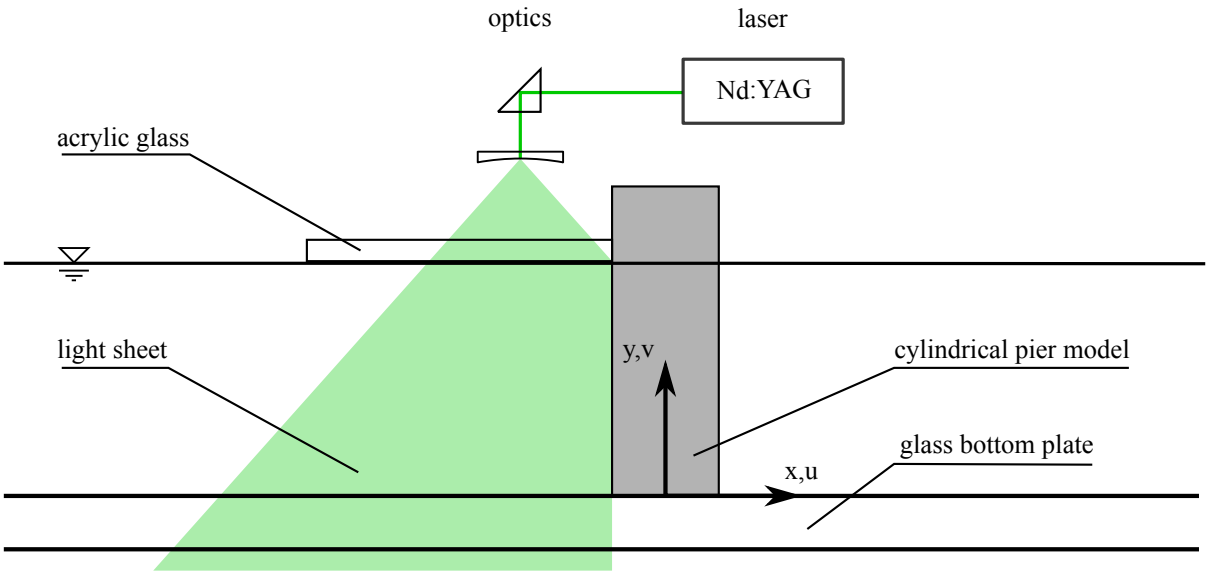

Figure 5.2: Sketch of measurement set-up in the symmetry plane in front of the cylinder adapted from Jenssen et al. (2016a).

spheres with a diameter of $d_{part} = 10\,\mu m$ and a density of $\rho_{part} = 1\,100\,kg/m^3$. This results, using Eq. (2.6), in a particle relaxation time $t_r = 6.11 \cdot 10^{-6}\,s$. To determine if the particles are capable of tracking all scales of the fluid's motion, the relaxation time has to be compared to the Kolmogorov time scale (cf. Section 2.1.1). This time scale depends on the dissipation rate ϵ and the kinematic viscosity of the fluid, which was assumed to $\nu_{fluid} = 1 \cdot 10^{-6} \frac{m^2}{s}$. A macro scale estimation of the dissipation rate can be made using Eq. (5.2) (Pope, 2001). So it can be approximated to $\epsilon = 0.593\,\frac{m^2}{s^3}$. Schanderl et al. (2016) showed in a detailed discussion of the dissipation rate that this estimate is conservative within this context. The corresponding Kolmogorov time scale reads $t_\eta = 1.296 \cdot 10^{-3}\,s$, which results in a Stokes number of $St = 4.715 \cdot 10^{-}3 \ll 1$. Therefore, the used particles are expected to be able to track all predicted scales of motion. Using the characteristics of the ensemble averaged autocorrelation function, the mean particle image diameter was determined to $d_{e,x} = 3.13\,px$ and $d_{e,y} = 3.41\,px$, resulting in slightly elliptic particle images.

$$\epsilon = \frac{u_{bulk}^3}{D} \tag{5.2}$$

5.3 Properties of Image Data Used

The properties of the image dataset strongly influence the signal-to-noise ratio of the correlation function as explained in Section 3.3. Therefore, the next sections concentrate on the image statistics and on the characteristics of the highly resolved near-wall region at the bottom plate.

5.3.1 Image Statistics

Fig. 5.3 shows the development of the mean intensity count of the image pairs with respect to time. The grid spacing in horizontal direction marks the 1 500 image pairs, after which the bottom plate was cleaned before a new set of images was recorded. Comparing the mean intensities of the image pairs, it can be observed that the second image is brighter than the first image. Furthermore, the mean intensities abruptly change at least four times within the first 10 0000 image pairs. The latter is related to a non-constant seeding, which has been improved afterwards.

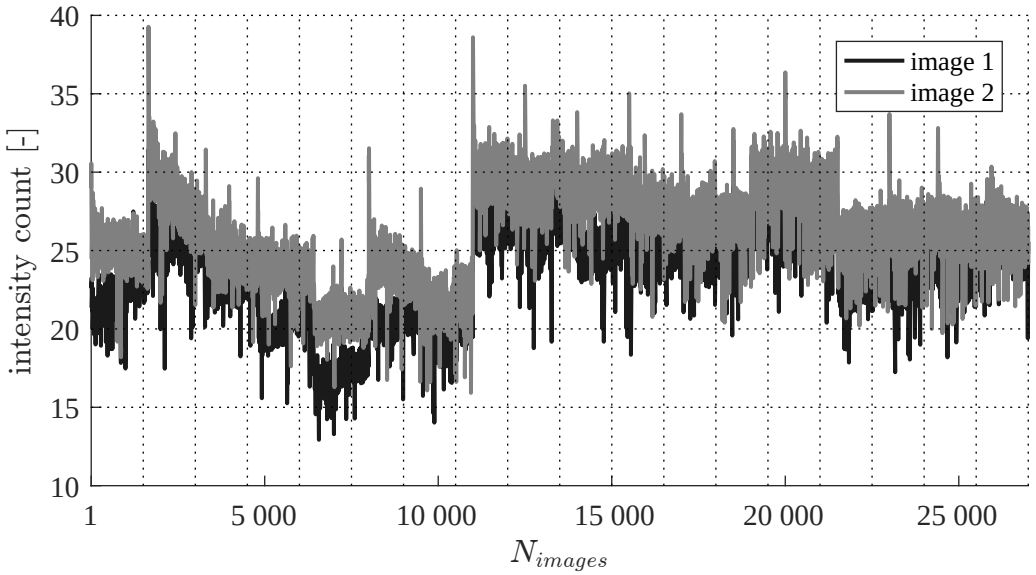

Figure 5.3: Mean image intensity count with respect to the number of images recorded.

Moreover, these intensity values were evaluated to determine the number of particles contained in an image. A particle was assumed to be present if the intensity value was larger than three-times the standard deviation of all intensities collected at this position. This results in 195 particles registered at the center pixel of the image after 27 000 image pairs, which relates to a mean seeding density of $0.007\,ppp$. This number was confirmed by manually counting individual particles in several images.

5.3.2 Near-Wall Region

An exemplary recording is shown in Fig. 5.4. The cylinder is positioned on the right edge of the image. Furthermore, the region evaluated using SPE is marked by a red rectangle. The position of the bottom plate can be seen as a horizontal white line caused by the reflection occurring there.

The magnification of the near-wall region (cf. Fig. 5.5) shows that the reflections cover several pixels in vertical direction. The glass bottom plate also acts as a mirror reflecting the particle images. This property was used to specify the position of the wall. The wall is located in the center between the particle and its mirrored image on the opposite

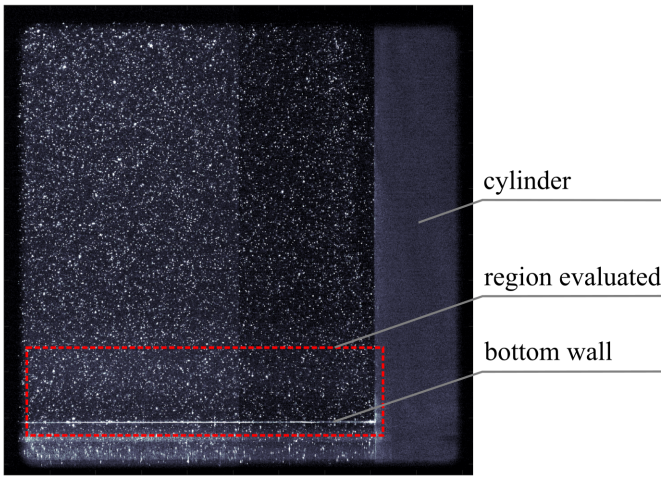

Figure 5.4: Exemplary PIV recording of the evaluated scene; red rectangle marks the area evaluated using SPE.

side. It was found that the camera position is slightly inclined with respect to the wall, such that the wall position increases from the left to the right side of the image by four pixels in vertical direction. Eq. (5.1) describes the determined vertical wall position with respect to the pixel coordinates in x-direction. The resulting double precision vertical coordinates were rounded up to the next integer value, when the wall was positioned in pixel values.

$$y_{wall} = 2.55848 \cdot 10^{-3}\, x + 229.0983 \tag{5.3}$$

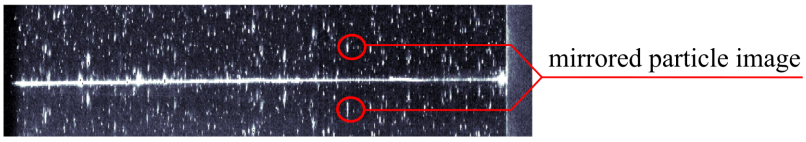

Figure 5.5: Magnification of the near-wall region including mirrored particle images and light reflections at the wall.

5.4 Evaluation Strategy

The dataset was evaluated in the same manner as the synthetic images in Section 4.2. The parameters of the image pre-processing, the correlation function, its pre-processing and the evaluation strategy applied at the wall are presented in the next sections.

5.4.1 Image Pre-Processing

In a first step the background noise was removed from the images by subtracting the time-averaged mean[1] from each individual image (cf. Section 3.3.1). Considering moreover that the light intensity is not constant throughout the time series (cf. Section 5.3.1), the intensity counts have to be equalized, such that all images contribute in the same manner to the ensemble averaged correlation function. For that reason all images were normalized by their individual mean intensity (cf. Section 3.3.1). This secures the same weight for each image in the averaging process.

5.4.2 Correlation Functions

To reduce the computational effort, only the first $280\,px$ above the wall were evaluated (cf. region marked by a red rectangle in Fig. 5.4). The mean velocities and standard deviation of the standard $16 \times 16\,px$ PIV results (Jenssen et al., 2016a) were used to define the size of the correlation plane, $25 \times 25\,px$, such that it fully covers the correlation peaks. Since the particle density is low, the approach introduced by Avallone et al. (2015) to double the number of samples by correlating not only the first with the second image of the consecutive pair, but also vice versa, was applied. This leads to approximately 390 samples contributing to the ensemble averaged correlation function at each pixel. Before the moments of the correlation and autocorrelation function were calculated, the functions were pre-processed using the standard deviation filter, introduced in Section 3.3.2; the maximum side length of the cut-out rectangle was $15 \times 15\,px$. 390 samples contributing to one correlation function is a very low number, especially if higher order moments are to be analyzed. Therefore, the dataset was evaluated a second time averaging five correlation functions in streamwise direction before applying the pre-processing and calculating statistical moments. This increases the number of samples contributing to each evaluated correlation function to 1 950. The effect of this spatial averaging is discussed in Section 5.5.1 and 5.5.2. The averaging was not performed in wall-normal direction as this would have changed the characteristics of the velocity profiles in the near-wall region, due to the strong vertical gradients occurring there.

5.4.3 Near-Wall Region

In order to reduce the influence of reflections at the bottom wall, all pixels below the wall were masked with zeros, such that these regions do not contribute to the correlation function. This procedure makes it possible to recover reasonable measurement values beginning at two pixels above the wall, which is above the physical constraints due to the particle size, $y_{min} = 0.5 \cdot d_{e,y} = 1.7\,px$ (Kähler et al., 2012a). At some positions the first accurate measurement points occur four to five pixels above the wall, due to the strong accumulations of particles at the wall.

[1] the time average of each pixel within the time series

5.5 Results

This section discusses the results of the SPE evaluation. First mean velocities and Reynolds stresses are addressed for the vortex system and a comparison between SPE, standard PIV and LES is made. Then the near-wall region is investigated in detail. Afterwards, the shape of the correlation function is compared to the velocity PDFs reported in the literature and the third and fourth order moments are analyzed.

5.5.1 Mean Velocities and Reynolds Stresses

In what follows, the mean velocities and Reynolds stresses are discussed in detail. First the results of the SPE evaluation are compared to results of a standard PIV evaluation (Jenssen et al., 2016a) of the same dataset with an interrogation window size of $16 \times 16\,px$ and 50% overlap performed with the commercial TSI software, Insight 4G$^{\text{TM}}$ (Version 10.1.0.5). Furthermore, a comparison to an LES evaluation (Schanderl and Manhart, 2016) of the same flow case is performed. Then the mean streamwise and vertical velocity components and the Reynolds normal and shear stresses are addressed. Except for the comparison to PIV and LES in the following all velocities, Reynolds stresses and higher order moments are shown in pixel displacements to emphasize the magnitudes of the displacement. Therefore, in these cases the Reynolds stresses were furthermore divided by the fluid density $\rho = 1000\frac{kg}{m^3}$ to reach the unit px^2.

Comparison to Standard PIV and LES Results

Fig. 5.6 compares streamlines of the time-averaged flow fields in front of the cylinder determined from SPE (a), standard $16 \times 16\,px$ PIV of the same dataset (Jenssen et al., 2016a) (b) and LES (c) (Schanderl and Manhart, 2016). The seeding points to compute the streamlines were equally distributed on a diagonal line from the left bottom corner to the right top corner. Both the standard PIV results as well as the SPE results were median filtered before the streamlines were determined.

The main vortex V1 and the corner vortex V3 are observable in all three evaluations. Vortex V2 can only be guessed in the dense streamline region upstream of the main vortex, $-1.0 \leq x/D \leq -0.9$. The flow structures are similar in all three cases, although the streamlines of the SPE result are not as densely packed at the main vortex as in the PIV and LES results. Focusing on the vortexes, it can be observed that the corner vortex V3 is the largest in the SPE result, which stems from the high spatial resolution of the SPE evaluation. A comparison of the main vortex V1 reveals three main differences: (1) the position of the SPE result is in the center between standard PIV and LES; (2) the extent of the vortex determined by SPE and LES is larger than in standard PIV; (3) the vortex of the standard PIV result is horizontally aligned, while the vortexes of SPE and LES are slightly tilted to the right.

The standard PIV result differs from SPE due the strong velocity gradients occurring in the region of the vortex. On the one hand these gradients cause the correlation function to be skewed and thus lead to wrong estimates of the mean velocity (cf. Section 2.2.1), which can be overcome if window deformation techniques are applied. This techniques deform the interrogation window according to the estimated velocity gradient and, thus, reduce the in-

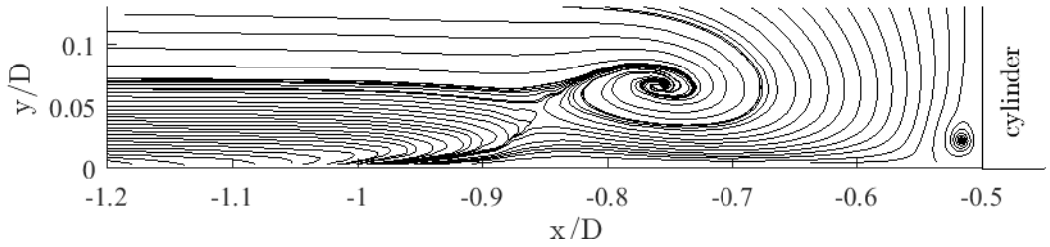

a: SPE

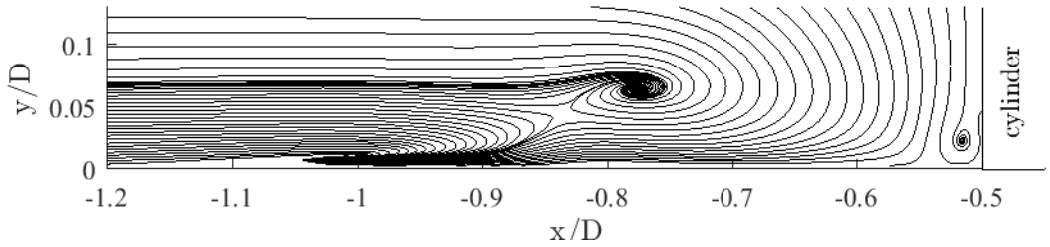

b: Standard PIV

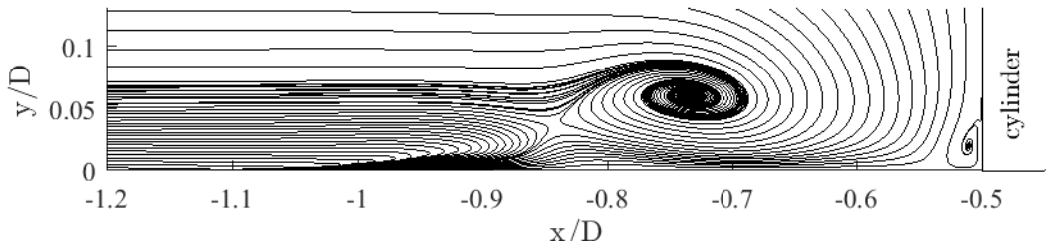

c: LES

Figure 5.6: Streamlines in the symmetry plane in front of the cylinder, (a) SPE median filtered over $16 \times 16\,px$, (b) Standard PIV interrogation window size $16 \times 16\,px$ and 50% overlap, (c) LES; (b) and (c) were computed using the velocity fields of Jenssen et al. (2016a) (PIV) and Schanderl and Manhart (2016) (LES).

plane loss of particle pairs (Adrian and Westerweel, 2010). On the other hand this deviation results from the coarser spatial resolution of the standard evaluation technique, such that the gradient is smeared and averaged across the interrogation window. This decreases the capacity of standard PIV to determine the gradient correctly. Kähler et al. (2012b) showed that in standard PIV this capacity scales with the interrogation window size, such that the

limit of resolvable gradients is several times larger than of SPE.

Figs. 5.7 and 5.8 depict profiles of the mean velocities and Reynolds stresses on a horizontal and a vertical line through the core of the main vortex V1. Its position was determined using the SPE streamline pattern to $x/D = -0.754$ and $y/D = 0.0674$. The profiles match well, although the SPE results are noisier due to the low number of samples contributing to the correlation function. Note, that for the results shown here, five correlation functions were averaged in streamwise direction before the evaluation. Focusing on the mean velocities it can be observed that in regions of strong curvature the magnitude of the SPE result is slightly larger than the standard PIV result (cf. $\langle v \rangle / u_{bulk}$ in Fig. 5.7, $\langle u \rangle / u_{bulk}$ in Fig. 5.8), as standard PIV is not able to resolve strong gradients (Kähler et al., 2012b). Furthermore, SPE covers more details due to the higher spatial resolution and is able to resolve the velocity profiles down to the wall (cf. $\langle u \rangle / u_{bulk}$ and $\langle v \rangle / u_{bulk}$ in Fig. 5.8).

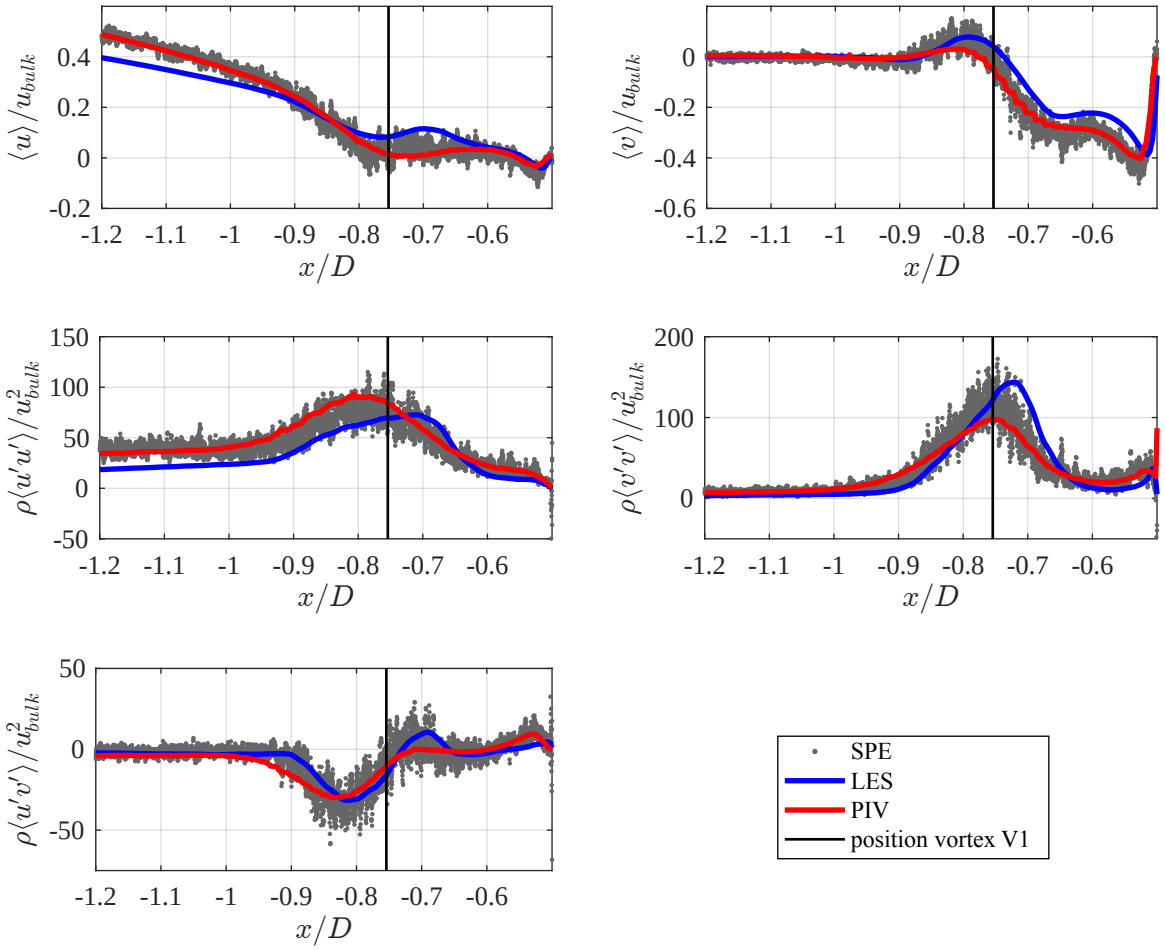

Figure 5.7: Comparison of profiles along a horizontal line through the core of vortex V1 between five neighboring SPE profiles after correlation function averaging, standard PIV (Jenssen et al., 2016a) and LES (Schanderl and Manhart, 2016).

The same effects can be observed for the Reynolds stresses. Close to the wall the streamwise normal stresses $\rho\langle u'u' \rangle / u_{bulk}^2$ coincident with the LES result (cf. Fig. 5.8). Whereas,

standard PIV is unable to resolve the sharp peak at $y/D \sim 0.01$ and even increases as it reaches the wall. In the horizontal profile of the vertical normal stresses $\rho\langle v'v'\rangle/u_{bulk}^2$ (cf. Fig. 5.7) the magnitude of the peak of the SPE result is similar to the LES result, while standard PIV does not reach this amplitude due to the spatial filtering and the strong local gradient occurring there, which also results in an underestimation of the vertical velocities (cf. Fig. 5.8 $\langle v\rangle/u_{bulk}$). Furthermore, the Reynolds shear stresses are comparable to the results of standard PIV and LES. In the horizontal profile, Fig. 5.7, they even recover the positive peak of the LES right downstream of the vortex core.

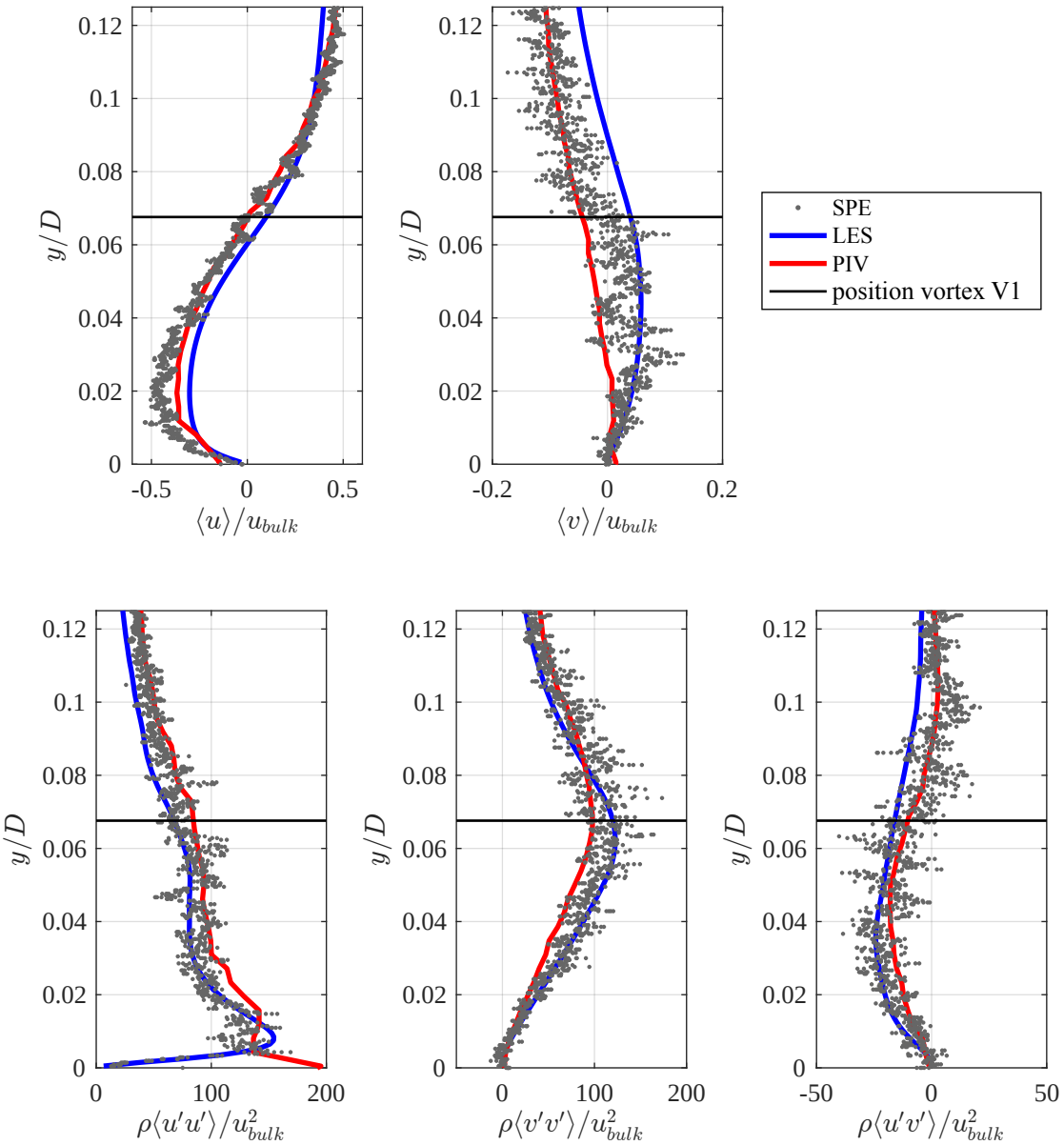

Figure 5.8: Comparison of profiles along a vertical line through the core of vortex V1 between five neighboring SPE profiles after correlation function averaging, standard PIV (Jenssen et al., 2016a) and LES (Schanderl and Manhart, 2016).

Mean Velocities

The mean velocity components in streamwise and vertical direction are depicted in Fig. 5.9. Besides the fine detailed structure, a positive-negative pattern of both velocity components around the vortex cores can be observed. As the main vortex rotates clockwise and the corner-vortex counter-clockwise, also the positive-negative patterns flip. Due to the low number of samples (390 *ppp*) the velocity fields are somewhat noisy, such that the vertical velocity component upstream of the main vortex ($x/D \sim -0.80$) fluctuates around zero. Furthermore, the strong vertical downward directed flow in front of the cylinder with zero or almost zero velocities in the streamwise direction is observable and the separation point at the cylinder front can be identified in the vertical flow field at about $y/D = 0.1$.

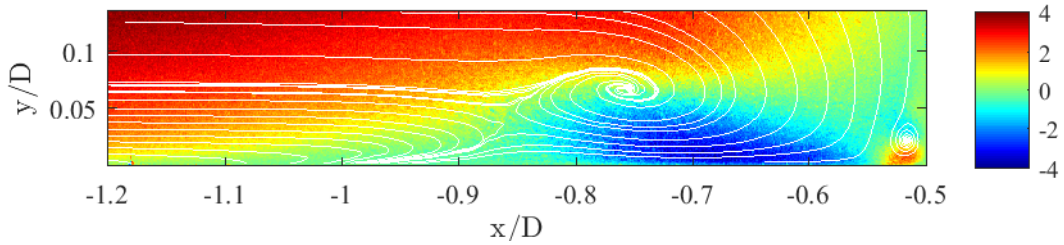

a: streamwise velocity $\langle u \rangle$ $[px]$

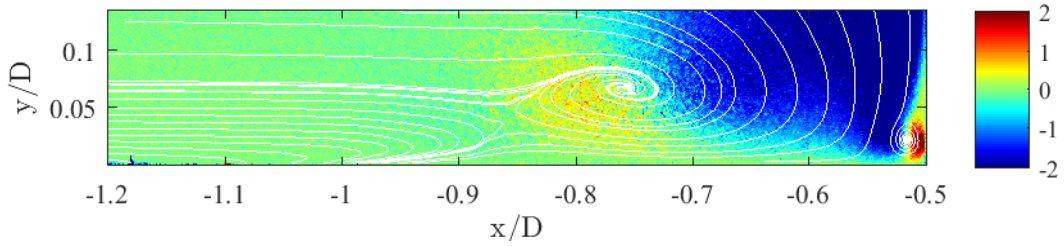

b: vertical velocity $\langle v \rangle$ $[px]$

Figure 5.9: Time-averaged velocity fields in front of the cylinder in (a) streamwise and in (b) vertical direction; on top streamlines as depicted in Fig. 5.6 (a).

Reynolds Stresses

Fig. 5.10 shows the Reynolds stresses determined from the single pixel evaluation. Note, that in order to stick to unit px^2 actually the variances and covariance are shown here, which can easily be transformed into stresses if the magnification factor and the density are included. Their structure is in good accordance to the results of Devenport and Simpson (1990), Apsilidis et al. (2015), Jenssen et al. (2016a) and Schanderl and Manhart (2016). In comparison to the results of the latter two, they agree in the spatial distribution of the maxima and minima and mainly in magnitude as shown before (cf. Figs. 5.7 and 5.8). Due to the high spatial resolution the footprint of the corner vortex V3 in the Reynolds stresses is resolved in this dataset, which is not the case for Apsilidis et al. (2015). The noise level

is rather large due to the low number of samples (390 *ppp*) contributing to the correlation function.

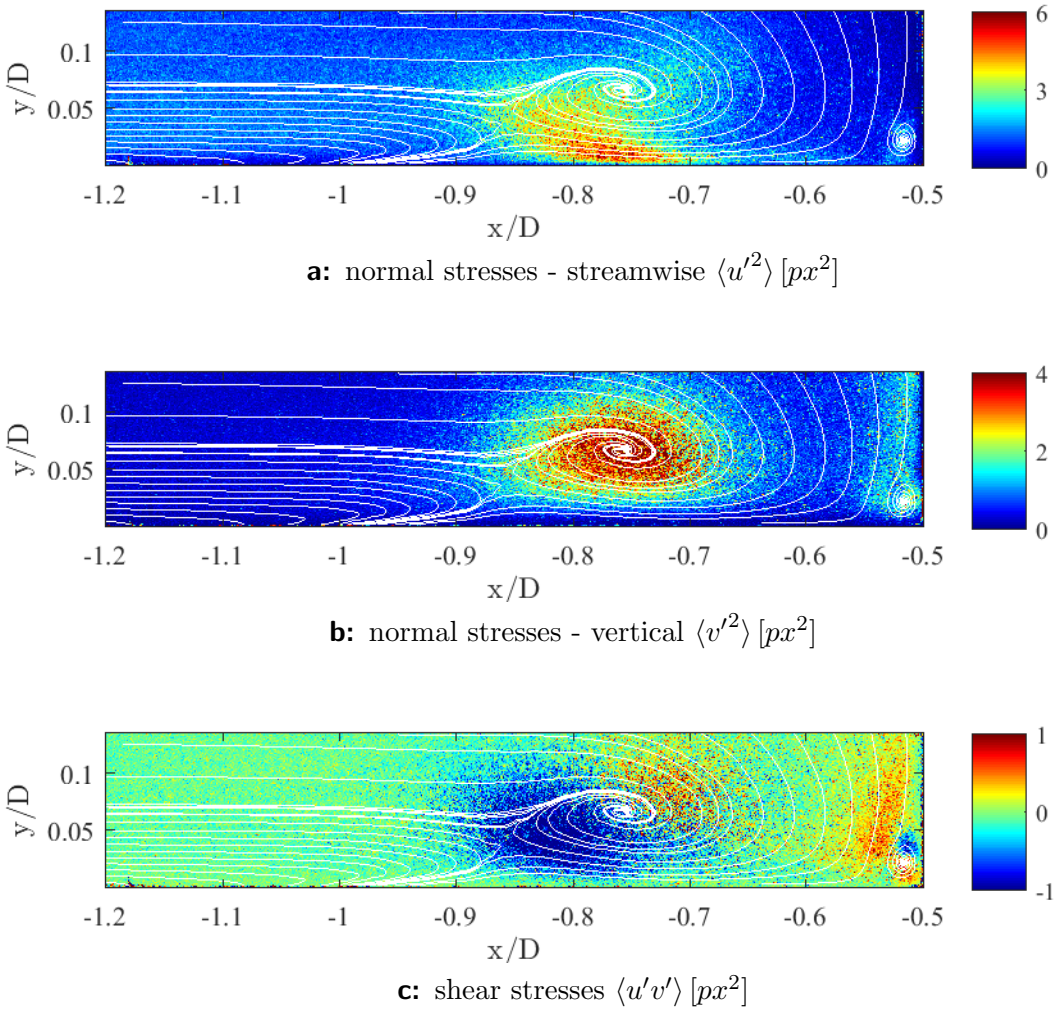

a: normal stresses - streamwise $\langle u'^2 \rangle$ $[px^2]$

b: normal stresses - vertical $\langle v'^2 \rangle$ $[px^2]$

c: shear stresses $\langle u'v' \rangle$ $[px^2]$

Figure 5.10: Time-averaged Reynolds stresses in front of the cylinder; normal stresses (a) streamwise (b) vertical and (c) shear stresses; on top streamlines as depicted in Fig. 5.6 (a).

In Fig. 5.11 the Reynolds stresses evaluated from correlation functions averaged over five pixels (1950 *ppp*) in streamwise direction are presented. The local correlation function averaging reduces the noise level, which can be seen especially in the shear stresses $\langle u'v' \rangle$. The vortexes can be identified in the Reynolds stresses. While the maximum of vertical normal stress is at the same position as the core of the main vortex, the maximum of the streamwise normal stresses can be found at the bottom-wall below the vortex core (cf. Fig. 5.11 (a), (b)). The maximum region of $\langle u'^2 \rangle$ close to the wall is due to fluctuations of the backward directed jet below the main vortex as discussed by Schanderl et al. (2016). At the corner vortex the structure of the normal Reynolds stresses is flipped, while the local maximum of the $\langle u'^2 \rangle$ is at the position of the vortex core, the local maximum of $\langle v'^2 \rangle$ can be found slightly

below the core closer to the wall.The sign of the Reynolds shear stress changes from negative upstream of the core of vortex V1 to positive downstream of the vortex core, Fig. 5.11 (c). For the main vortex the region of negative shear stress is significantly larger than the region of positive shear stress. In contrast to the corner vortex, where the positive and negative region are somewhat similar in size and shape. Furthermore, a vertical stripe of positive shear stress can be observed in front of the cylinder, where the flow splits into an upstream directed part and a downstream directed part, which will contribute to the corner vortex.

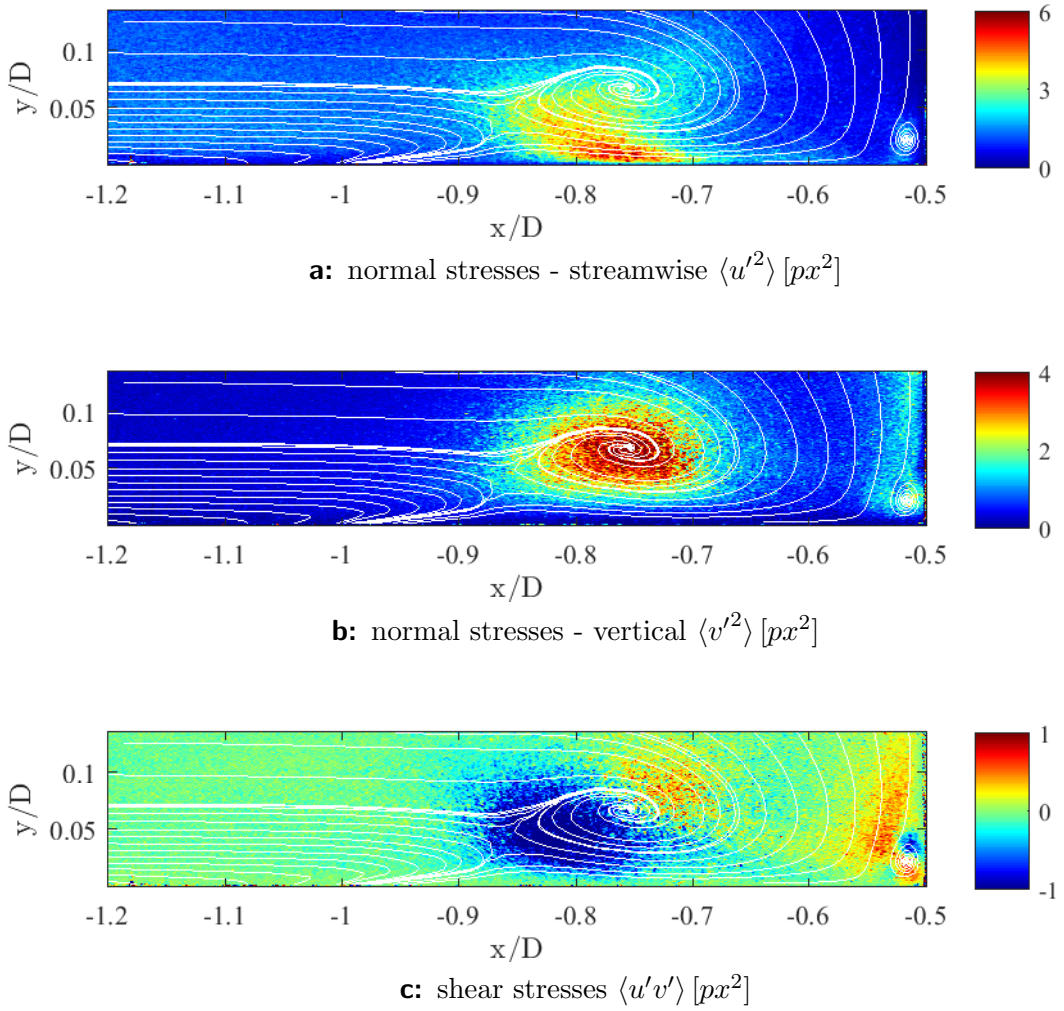

a: normal stresses - streamwise $\langle u'^2 \rangle$ $[px^2]$

b: normal stresses - vertical $\langle v'^2 \rangle$ $[px^2]$

c: shear stresses $\langle u'v' \rangle$ $[px^2]$

Figure 5.11: Time-averaged Reynolds stresses in front of the cylinder determined after five correlation functions were averaged in streamwise direction; normal stresses (a) streamwise (b) vertical and (c) shear stresses; on top streamlines as depicted in Fig. 5.6 (a).

5.5.2 Near-Wall Region

At non-moving boundaries, like the cylinder or the bottom wall, the velocity is zero. This so-called limiting behavior of the wall influences the near-wall profiles of mean velocities and

Reynolds stresses (Pope, 2001). In what follows, the ability of the SPE evaluation method to resolve this limiting behavior is discussed. First, near-wall profiles of mean velocities and Reynolds stresses are compared to theoretical estimates and the effect of streamwise correlation function averaging ahead of the evaluation is illustrated. Then the focus is on the linear region of the streamwise velocity profile, and profiles at different x-positions are compared. In the last paragraph velocity measures in the inner region are used to determine the wall shear stress distribution, which is compared to results from standard PIV of the same dataset (Jenssen et al., 2016b) and a LES of the same flow case (Schanderl and Manhart, 2016).

First and Second Order Statistics

The near-wall behavior of velocity and Reynolds stress profiles can be determined by a Taylor approximation. This leads to a near-wall linear profile of $\langle u \rangle$ and a quadratic profile of $\langle v \rangle$ and $\langle u'^2 \rangle$. The wall-normal Reynolds stresses approach the wall with respect to y^3 and the shear stresses with respect to y^4 (cf. Pope (2001)). Figs. 5.12 to 5.16 depict the near-wall profiles at five neighboring positions around $x/D = -0.652$ including the theoretical limiting curves fitted to the dataset. Single pixel results without smoothing are plotted on the left side (a) and results determined after averaging five correlation functions in streamwise directions are plotted on the right side (b). While the characteristics of the profiles stay unchanged, the scattering is strongly removed by averaging the correlation functions.

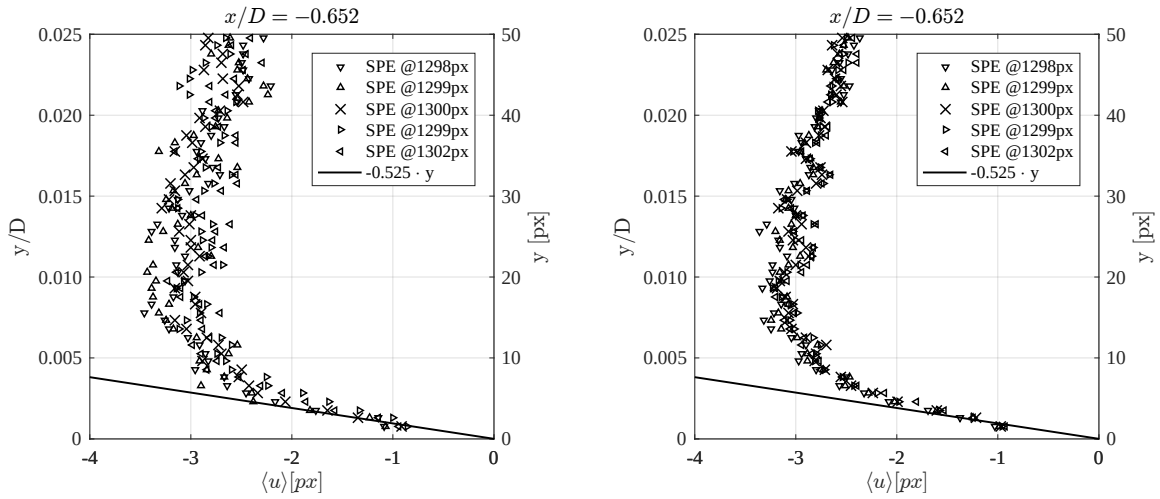

a: single pixel **b:** streamwise average of 5 pixels

Figure 5.12: Five neighboring near-wall streamwise velocity profiles at $x/D = -0.652$

In the near-wall region of $\langle u \rangle$ as well as of $\langle u'^2 \rangle$, Fig. 5.12 (b) and Fig. 5.14 (b), the five neighboring profiles collapse onto one curve and approach the wall on a linear or quadratic curve, respectively. There is an error in the first four pixels of $\langle u'^2 \rangle$, which is related to strong reflections occurring there, which smear the correlation peak in streamwise direction. The vertical velocity profiles as well as their corresponding Reynolds stresses, Fig. 5.13 (b) and Fig. 5.15 (b), also follow the theoretical profile and approach zero. Also the very small

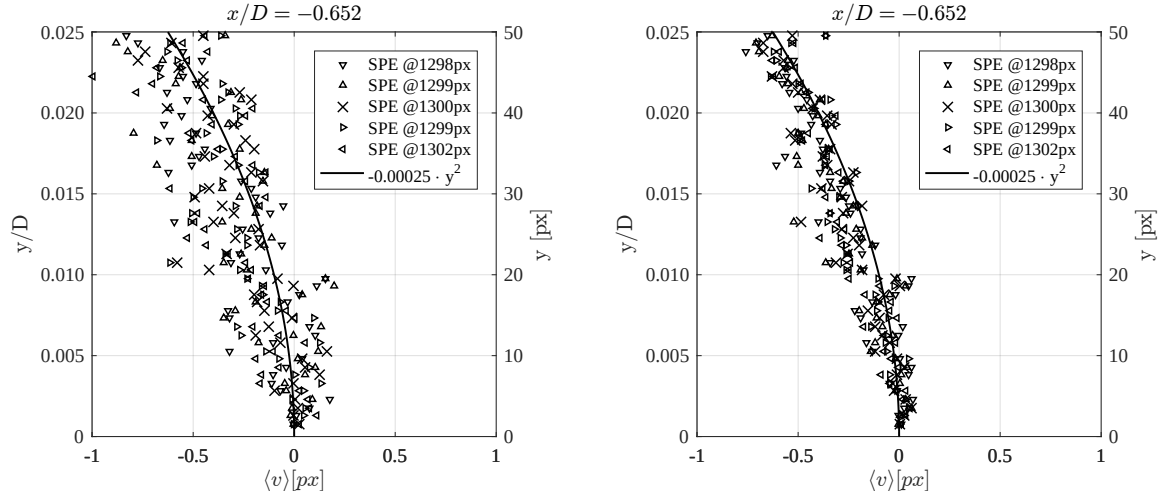

a: single pixel **b:** streamwise average of 5 pixels

Figure 5.13: Five neighboring near-wall wall-normal velocity profiles at $x/D = -0.652$

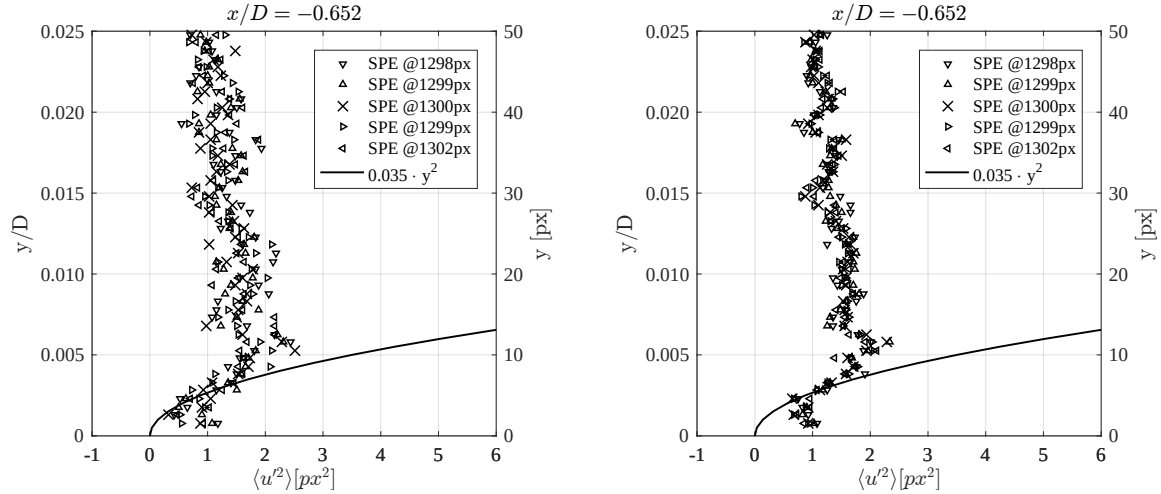

a: single pixel **b:** streamwise average of 5 pixels

Figure 5.14: Five neighboring near-wall streamwise Reynolds normal stresses at $x/D = -0.652$

Reynolds shear stresses benefit from the streamwise averaging (cf. Fig. 5.16) and are without any further scatter.

Linear Region

To determine the wall shear stress, velocities measurements within the linear region of the profile are needed to determine the near-wall gradient correctly. Schanderl and Manhart (2015) demonstrated that the linear region in this flow configuration is thinner $y^+_{cyl} \lesssim 3$ than in a non-disturbed turbulent boundary layer $y^+ \approx 5$. In this section two velocity profiles in inner scaling will be compared. The first profile is located at $x/D = -0.652$ downstream of the main vortex in a region of strong acceleration and the second profile at $x/D = -0.754$

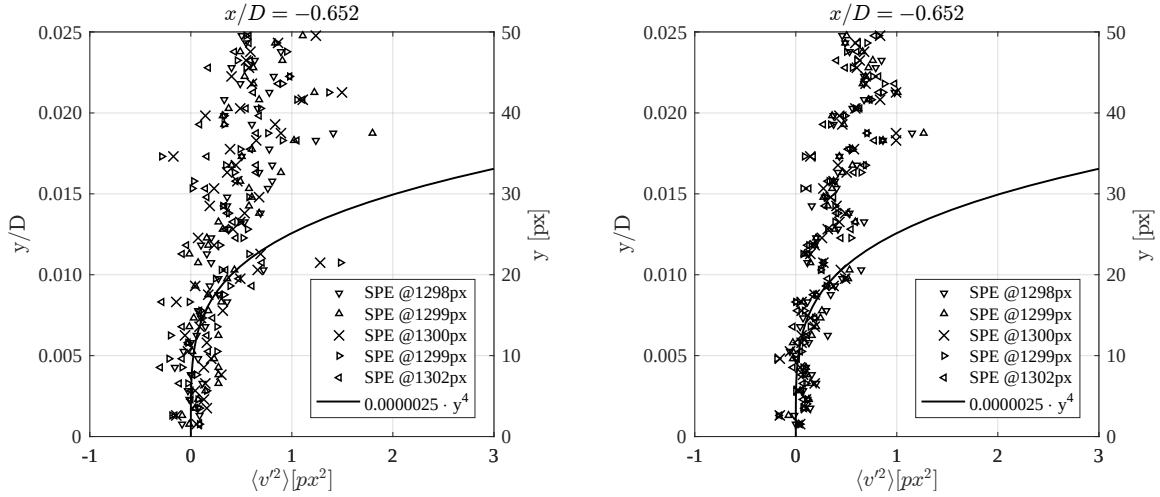

a: single pixel **b:** streamwise average of 5 pixels

Figure 5.15: Five neighboring near-wall wall-normal Reynolds normal stresses at $x/D = -0.652$

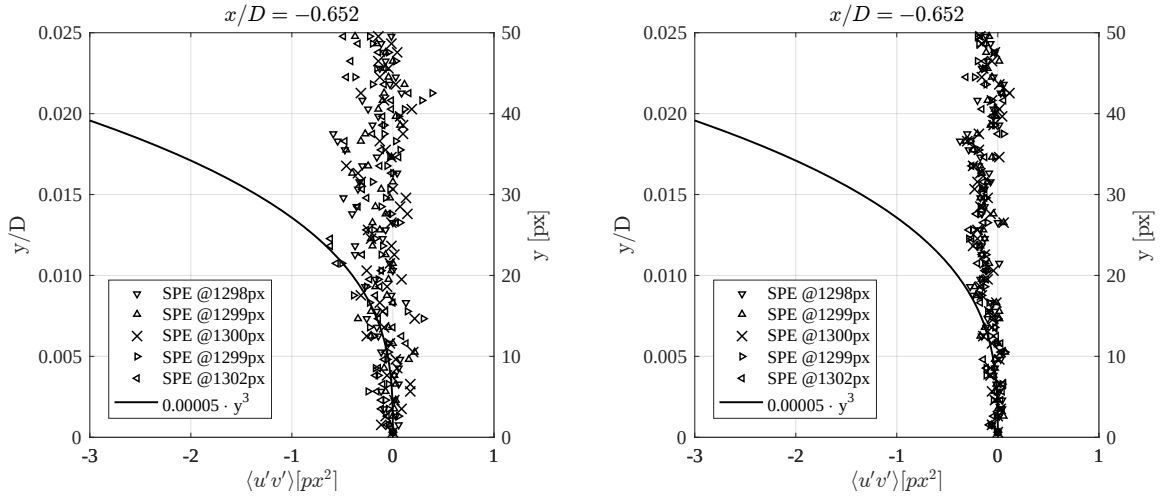

a: single pixel **b:** streamwise average of 5 pixels

Figure 5.16: Five neighboring near-wall Reynolds shear stresses at $x/D = -0.652$

below the core of the main vortex.

The upper limit of the linear region ($y^+ = 3$) as observed by Schanderl and Manhart (2015) is marked as linear limit. Furthermore, the physical limit of half a particle image diameter is indicated. This limit stems from the fact that the particle image is larger than one pixel. However, particles cannot pass the wall, such that velocity measurements closer to the wall than half the particle image diameter will be biased (Kähler et al., 2012a). This can be observed in Fig. 5.17, were the first measurement point above the wall is larger as expected by the linear flow profile. Going back to Fig. 5.12 this can also be observed there, where the wall nearest measurement point of each profile does not follow the linear curve that passes

the origin.

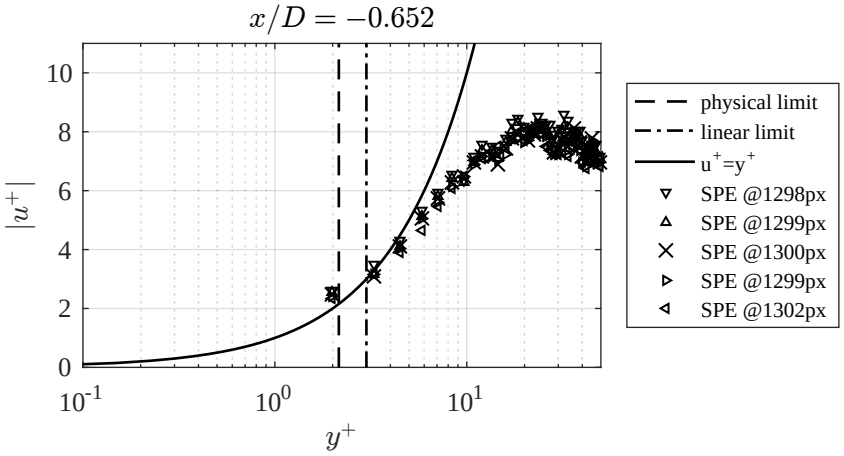

Figure 5.17: Near-wall streamwise velocity profiles in inner scaling close to the negative maximum of the wall shear stress; mean velocities were determined after five correlation functions were averaged in streamwise direction.

To determine the inner coordinates, the wall shear stress, τ_w, was estimated by the gradient of the second measurement point above the wall to $\tau_w = -0.7092\,N/m^2$, resulting in a friction velocity $u_\tau = \sqrt{\frac{\tau_w}{\rho}} = 0.0266\,m/s$ and an inner length scale $\delta_\nu = \frac{\nu_{fluid}}{u_\tau} = 37.55\,\mu m = 0.789\,px$. The inner length scale is very thin, such that the first reliable measurement point is already above the linear limit defined by Schanderl et al. (2016). Still it can be seen that the velocity profile begins to deviate from the linear profile quite early, in contrast to Fig. 5.18, where the velocity profile at the position of the main vortex is depicted in inner scaling. There the inner length scale is almost twice as large $\delta_\nu = 60.27\,\mu m = 1.266\,px$ and the velocity values follow the $u^+ = y^+$ profile up to $y^+ = 8$. This can be connected to the pressure gradient on the bottom plate which while being very large at the cylinder front is smaller at $x/D = -0.7$ (Dargahi, 1989, Schanderl and Manhart, 2016). In this region the vertical streamlines have turned into horizontal streamlines flushing backwards underneath the main vortex or contributing to the main vortex, such that the near-wall region is less compressed by the downward directed flow component and the inner layer starts to expand. This can also be seen in the wall stress distribution in the next section.

Wall Shear Stress

According to the previous section the thickness of the linear region varies strongly in streamwise direction. In what follows, the wall shear stress and the corresponding friction coefficient $c_f = \langle\tau_w\rangle/0.5\rho u_{bulk}^2$ are discussed and compared to the results of standard PIV (Jenssen et al., 2016b) and LES (Schanderl and Manhart, 2016). Since streamwise correlation function averaging improves the smoothness of the velocity profiles, these results were used to determine the wall shear stress. It was calculated as the gradient of a near-wall velocity measurement with respect to zero velocity at the wall. As not every measurement point located in the first pixel above the wall is also further than half the particle image

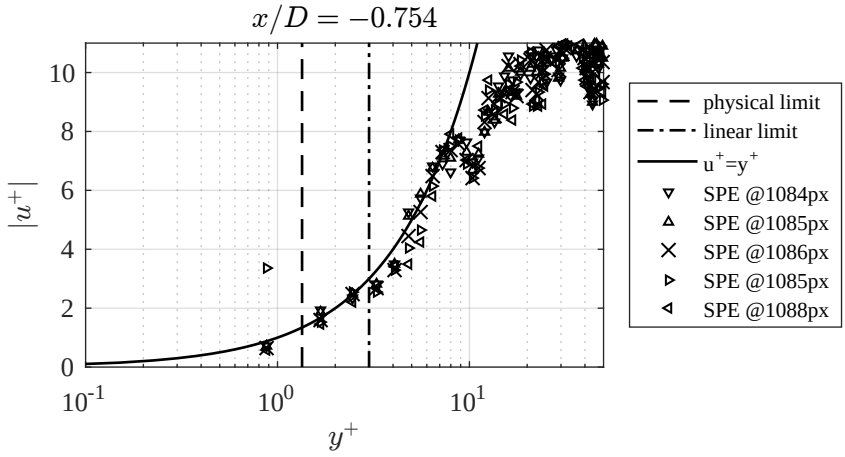

Figure 5.18: Near-wall streamwise velocity profiles in inner scaling below the core of main vortex V1; mean velocities were determined after five correlation functions were averaged in streamwise direction.

diameter[2] above the wall due to the slightly rotated camera, three evaluations were performed:

1. at the wall nearest measurement point, $4.76 \cdot 10^{-4} \leq y/D \leq 9.52 \cdot 10^{-4}$, biased for $y/D \leq 8.09 \cdot 10^{-4}$;
2. at the measurement point two pixels above the wall, $9.52 \cdot 10^{-4} \leq y/D \leq 1.4 \cdot 10^{-3}$;
3. at the measurement point six pixels above the wall, $2.9 \cdot 10^{-3} \leq y/D \leq 3.3 \cdot 10^{-3}$.

The first two evaluations are close to the first measurement point of the LES, which is located at $y/D = 5.0 \cdot 10^{-4}$ (Schanderl and Manhart, 2016), while the last evaluation is in the range of the wall nearest standard PIV interrogation window (Jenssen et al., 2016a). Fig. 5.19 compares the three different evaluations to the results of LES and PIV.
Focusing first on the three different evaluation positions it can be observed that as the distance to the wall increases the vertical scatter reduces. While the magnitudes of the friction coefficient determined using the first and second pixel above the wall are very similar and only small difference can be seen around $x/D = -0.6$ and at the positive peak right in front of the cylinder, the magnitude of the friction coefficient determined using the velocity measurements six pixels above the wall is significantly smaller at these positions. This can be explained by the fact, that the linear region is very thin in these areas, such that the measurement points six pixels above the wall are not within the inner sublayer (cf. Fig. 5.17).

In Fig. 5.19 it can be seen that the SPE results a very similar to the results of LES, while the standard PIV results differ. Upstream of the cylinder, first a positive peak occurs at the position of the corner vortex, then the wall shear stress turns negative and forms a plateau in the region of the wall-parallel jet. Then the friction coefficient and, thus, the wall shear stress reduces until it remains at almost zero upstream of the main vortex. Standard PIV is also able to represent this behavior in general but does not resolve the strong positive peak and the plateau of negative friction coefficient at $-0.65 \leq x/D \leq -0.55$, due to the lower spatial resolution and the thin inner layer in this area (cf. previous section). In contrast to

[2] $0.5\, d_e = 1.7\, px = 8.09 \cdot 10^{-4} y/D$

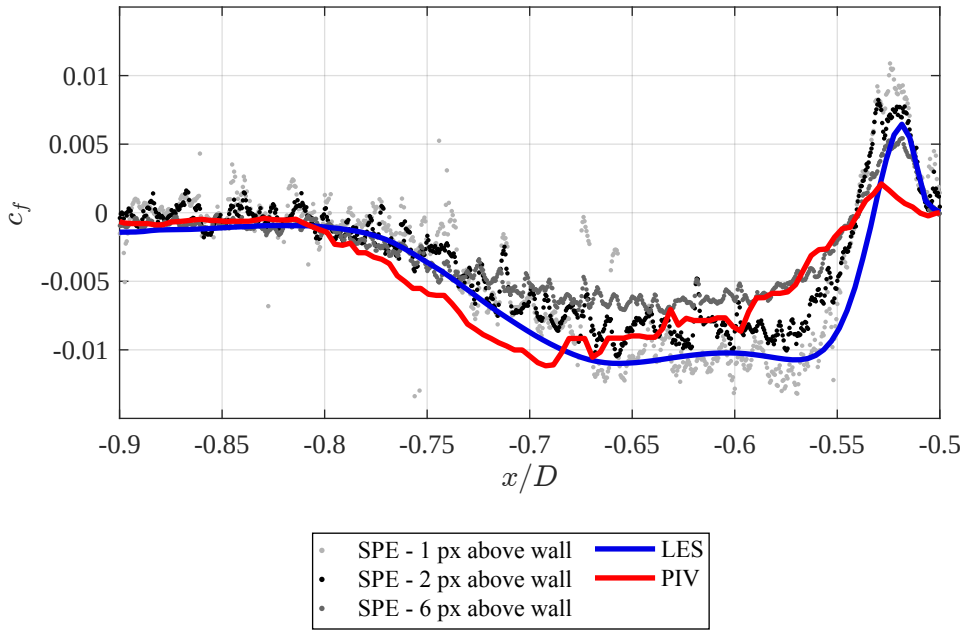

Figure 5.19: Friction coefficient c_f determined using different vertical positions in contrast to results from standard PIV (Jenssen et al., 2016b) and LES (Schanderl and Manhart, 2016).

the friction coefficient determined from the gradient of the sixth measurement point above the wall, standard PIV does not resolve the positive peak, neither in magnitude nor in width and appears to overestimate the wall shear stress for $-0.8 \leq x/D \leq -0.7$. Whereas, the different SPE evaluations converge to the same values upstream of $x/D = -0.7$, which is in accordance to the observations made before as the inner layer begins to expand in this region, such that more than the first few measurement points are recorded within the linear layer.

5.5.3 Probability Density Functions of Velocity

Devenport and Simpson (1990) as well as Paik et al. (2007) and Kirkil and Constantinescu (2015) report bimodal velocity PDFs in a region between $-0.86 \leq x/D \leq -0.62$ and $0.0 \leq y/D \leq 0.09$. Since the PDF of the velocity is contained in the correlation function (cf. 3.1.4), this section evaluates if this behavior can be found in the ensemble averaged correlation functions as well.

Fig. 5.20 depicts the sum of all rows of the correlation and autocorrelation functions as well as of the velocity PDF at several vertical positions below the core of the main vortex V1. The velocity PDF was determined using an iterative deconvolution of the correlation function by the autocorrelation function (cf. 4.1.2). Focusing first on the autocorrelation functions it can be seen that they barely differ as the vertical position increases. This meets the expectations as the autocorrelation function represents the mean particle image, and the particles do not change across the measurement area.

The correlation functions and the PDFs show a different behavior as the vertical position increases: close to the wall, $0.0015 \leq y/D \leq 0.0031$ the functions form a sharp peak at approximately zero. Raising further from the wall, they widen in x-direction and become negatively skewed, until two peaks - a bimodal distribution - can be observed at $y/D = 0.0106$. Moving even further away from wall the second peak lowers again and the functions are positively skewed until a smeared Gaussian peak remains. This behavior is in accordance to Devenport and Simpson (1990), although the bi-modality is not as well resolved as in their study. Comparing the correlation functions and the PDFs it can be seen how deconvolution removes the particle image from the correlation function and, thus, narrows the function. Therefore, the bi-modality can be observed better than in the correlation functions, however deconvolution also adds some roughness to the functions as can e.g. be observe at $y/D = 0.0527$.

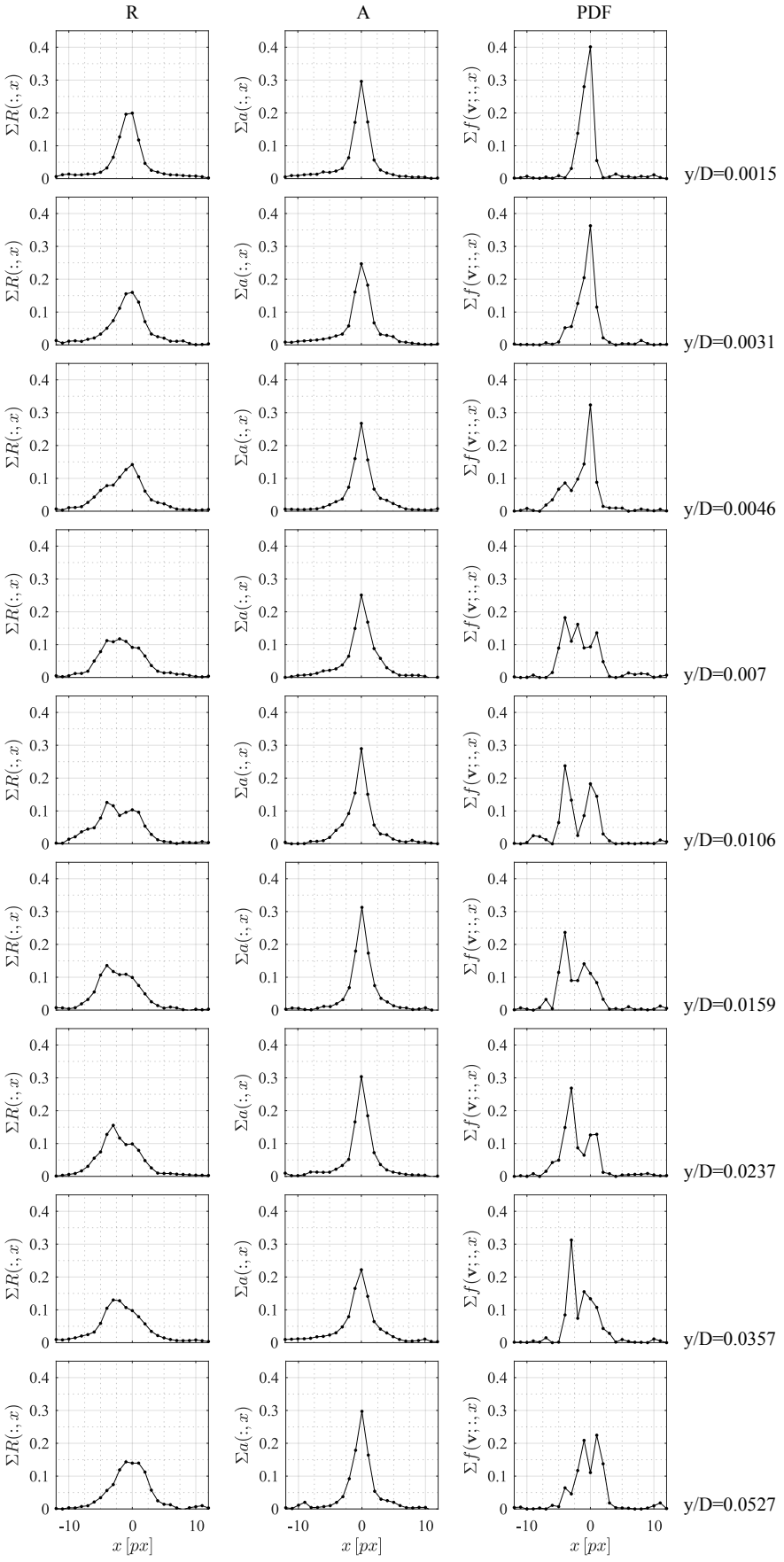

Figure 5.20: Streamwise component of correlation functions R, autocorrelation functions A and PDFs at 3, 7, 10, 15, 22, 33, 50, 75 and 135 pixels above the bottom wall below the core of vortex V1.

5.5.4 Higher Order Moments

The third and fourth moments reveal the deviation of the velocity JPDF from a Gaussian shaped distribution function. While the third moment describes the symmetry property, the fourth moment indicates the compactness of a function. Due to the large noise levels of both moments and the second moment, which would introduce further noise, if the central moments would be normalized by the standard deviations, this section is restricted to the discussion of the central moments instead of the skewness and kurtosis.

Third Central Moment

Recalling Section 3.2, a positively skewed distribution leans in negative direction, while a negatively skewed distribution leans in positive direction. Considering velocities, a positive third moment results from sporadic velocities significantly larger than the mean velocity, while the opposite happens if a negative third moment is recorded.

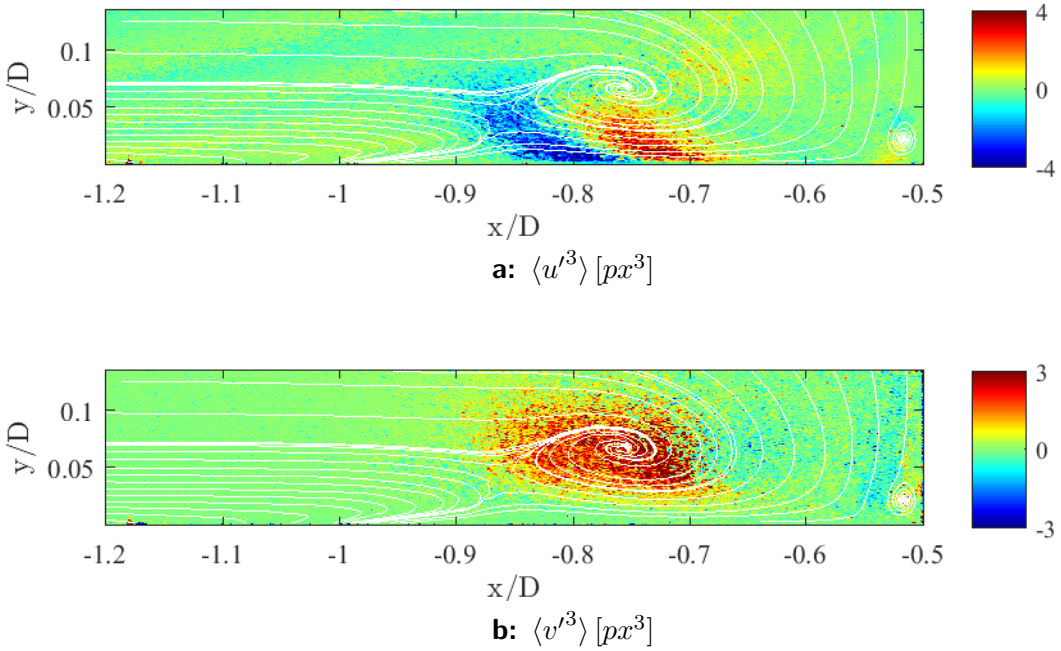

Figure 5.21: Third central moments in front of the cylinder determined after five correlation functions were averaged in streamwise direction; (a) and (b) normal in streamwise and vertical direction; on top streamlines as depicted in Fig. 5.6 (a).

Keeping this in mind, and comparing the mean streamwise velocity, Fig. 5.9 (a), to the third central moment, Fig. 5.21 (a), it can be seen that the mean velocity in front and below the core of the main vortex V1 is strongly negative, however due to the positive sign of the third moment, sporadic strong positive fluctuations u' and thus velocity events less negative must occur. The opposite can be observed upstream of the vortex core, where third moment turns negative. Here, the mean velocities are either small negative or close to zero, but, according

to the skewness, rare strong negative velocity events must occur.

Considering the two flow modes introduced by Devenport and Simpson (1990), back flow and zero-flow mode, this pattern represents the region in which the vortex moves during the transition between the two modes. Due to the definition of u', $u' = u - \langle u \rangle$, a positive u' occurs if $u > \langle u \rangle$ and a negative u' occurs if $u < \langle u \rangle$, with u being an instantaneous velocity value. Therefore, the position of the main vortex in the backflow mode must be located in the region of negative third moment ($-0.85 \leq x/D \leq -0.75$), while the position of the upward directed jet must be located in the area of positive third moment ($-0.75 \leq x/D \leq -0.70$). The locations of these back and zero-flow mode zones are in good agreement to the observations of Devenport and Simpson (1990).

The vertical third central moment, Fig. 5.21 (b), shows a main zone of positive moment in the region of the main vortex V1. The maximum of this region is located slightly downstream of the vortex core, but at the same vertical distance to the bottom wall. This is in accordance to the two flow modes: if an upward directed jet occurs in the region of $-0.75 \leq x/D \leq -0.70$, as discussed in the previous paragraph, then also sporadic strong positive fluctuations v' must occur, as the mean velocity points towards the wall in this region.

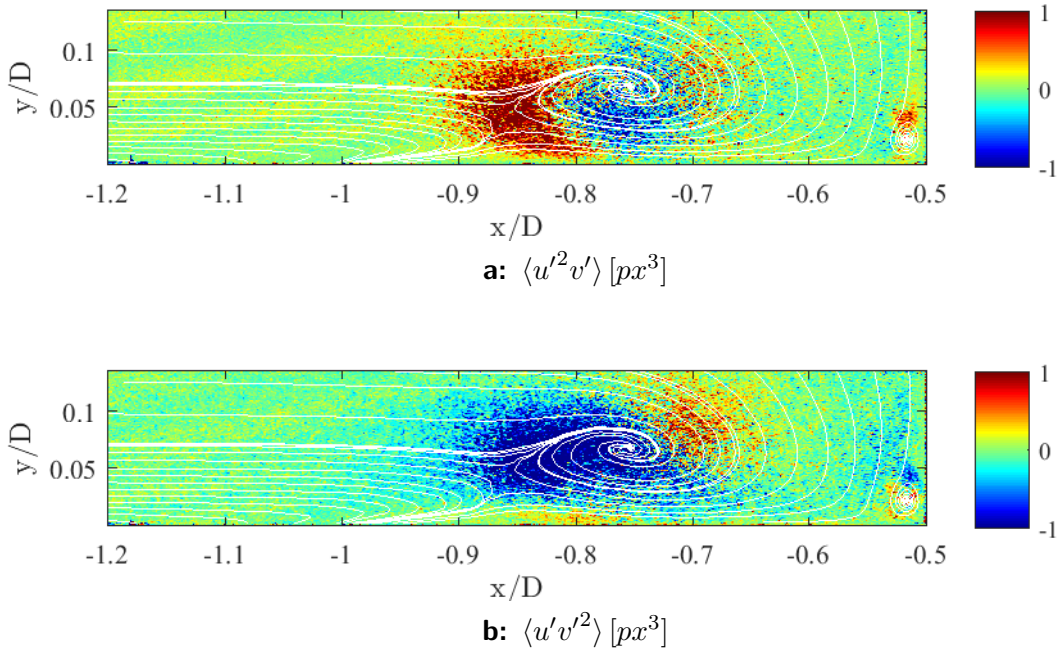

Figure 5.22: Third central cross-moments in front of the cylinder determined after five correlation functions were averaged in streamwise direction; (a) in streamwise cross wall-normal and (b) in wall-normal cross streamwise direction; on top streamlines as depicted in Fig. 5.6 (a).

Although the moments were determined after five correlation functions were averaged in streamwise direction the fields of the third cross-moments, Fig. 5.22 (a) and (b), are very noisy due to the low number of samples and the high order of the moment. However,

a distinctive positive/negative pattern around each vortex can be discovered. The third cross-moments, e.g. $\langle u'^2 v' \rangle$ describe the transport of $\langle u'^2 \rangle$ by the fluctuations v'. Thus, considering $\langle u'^2 v' \rangle$ (cf. Fig. 5.22 (a)) the region of positive moment represents a transport of $\langle u'^2 \rangle$ in upward direction, while the region of negative moment at the vortex core represents a downward directed transport of $\langle u'^2 \rangle$. Focusing on $\langle u' v'^2 \rangle$ (cf. Fig. 5.22 (b)) it can be observed that in the range of $-0.9 \leq x/D \leq -0.75$ $\langle v'^2 \rangle$ is transported in upstream direction, while downstream of the vortex core at $x/D \sim 0.7$ a maximum occurs indicating a transport of $\langle v'^2 \rangle$ towards the cylinder, which again is an indication of the spatial fluctuation of the vortex position.

Fourth Central Moment

The fourth central moment is a measure for the compactness of the distribution function. Larger values are a result of wide tails, while small values resemble a more compact distribution function. Very similarly to $\langle u'^2 \rangle$ and $\langle v'^2 \rangle$ (cf. Fig. 5.11 (a) and (b)), the fourth central moment of the streamwise velocity maximizes at the bottom-wall below the main vortex V1 (cf. Fig. 5.23(a)), while the fourth moment of the wall-normal velocity component has its maximum in the region of the vortex core (cf. Fig. 5.23(b)). Thus, the largest fluctuations in streamwise direction therefore occur in the region of the backward directed jet, while in vertical direction they occur at the core of the main vortex V1.

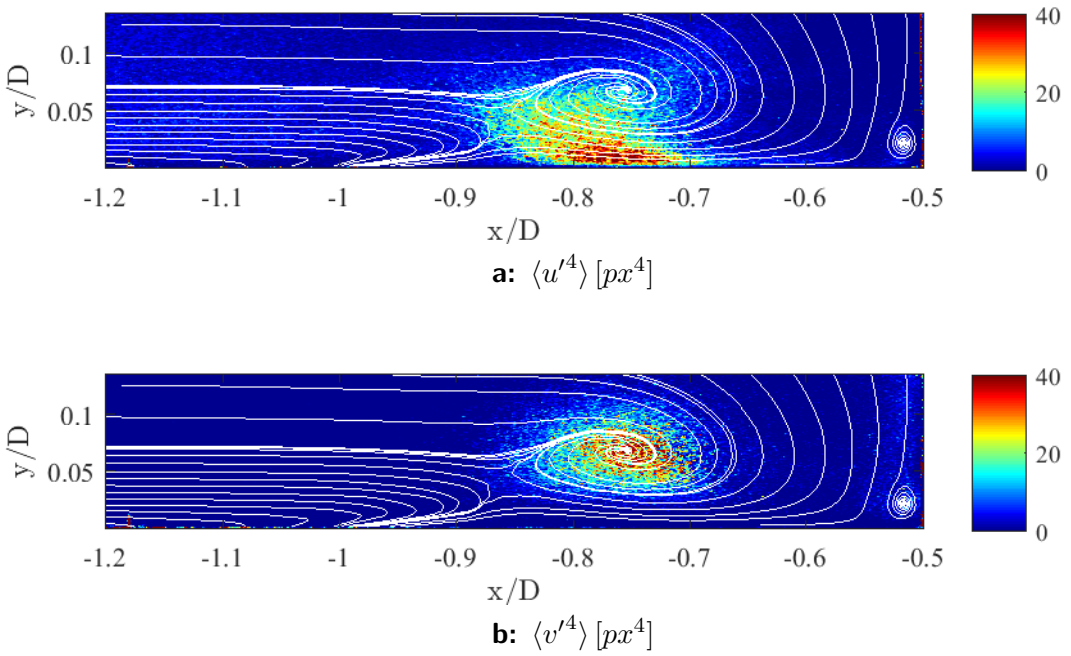

Figure 5.23: Fourth central moments in front of the cylinder in streamwise (a) and vertical (b) direction, determined after five correlation functions were averaged in streamwise direction; on top streamlines as depicted in Fig. 5.6 (a).

5.6 Summary

Concluding this chapter, it can be stated that the newly introduced method is able to determine mean velocities as well as higher order moments from a real PIV dataset. A comparison to a standard PIV evaluation of the same data showed the improvements possible in spatial resolution. Due to this, SPE was able to resolve the limiting behavior of the wall for the mean velocities and Reynolds stresses and to achieve wall shear stresses of a similar magnitude and structure as determined by a LES simulation of the same flow (Schanderl and Manhart, 2016). Furthermore, the bimodal and skewed characteristics of the velocity JPDF were resolved. This was not only presented inspecting correlation functions but also by discussing the third and fourth order moments.

Still, the noise level of the SPE results was quite high, even after five correlation functions were averaged in streamwise direction before the evaluation. Particularly in the higher order moments, this noise was problematic and made it impossible to determine the skewness and flatness of the velocity field as noise occurring in the variances would have led to additional noise in these already noisy parameters. Thus, to determine also higher order moments of high accuracy either larger image datasets have to be recorded, more particles have to be added to increase the number of samples contributing to the correlation peak or methods to smoothen the results in a different way have to be developed.

6 Conclusion

In this work a method has been developed to estimate the statistical moments of the velocity JPDF entrapped in SPE correlation functions, regardless of its shape and size. It was shown that a statistical moment of the velocity JPDF can be determined by a combination of the statistical moments of the correlation and the autocorrelation function, since the correlation function can be considered the convolution of the velocity JPDF and autocorrelation functions (Adrian, 1994, Soria and Willert, 2012). In contrast to methods proposed in the literature so far, which reconstruct the velocity JPDF either by Gaussian curve fitting (Scharnowski et al., 2012) or deconvolution (Scharnowski and Kähler, 2013), the new method has no need in fully restoring the JPDF and, thus, does not suffer from the restriction of either method: Gaussian curve fitting is restricted to the Gaussian shape of the fitted curves and deconvolution has to be performed iteratively and is not able to restore distribution functions narrower than the pixel grid spacing.

Applying the developed method to synthetic datasets, it was not only shown that the method is capable of determining the statistics of velocity JPDFs of various shapes and sizes but also that the result strongly depends on the noise level contained in the correlation and autocorrelation function. This noise level is influenced by the noise of the images recorded, but also by the number of samples contributing to the correlation peak, such that a larger number of image pairs always improves the signal-to-noise ratio of the correlation functions. Since noise can never be avoided and the number of image pairs recorded is restricted, correlation function pre-processing techniques were tested, which efficiently reduce the influence of noise on the final result. From these pre-processing methods, not only the method developed here profits, but also other methods that depend on the smoothness of the correlation and the autocorrelation functions, such as the deconvolution method.

Furthermore, the method was applied to a PIV dataset recorded in front of a vertical cylinder mounted on a flat plate at a cylinder diameter based Reynolds number $Re = 39\,000$. There, the advantages of the proposed SPE evaluation routine in contrast to the standard $16 \times 16\,px$ PIV evaluation by Jenssen et al. (2016a) were evident. While the overall structures and magnitudes of the velocity and Reynolds stress profiles were in good accordance, the SPE evaluation was far more detailed and able to resolve strong velocity gradients and fine flow details. So it was possible, to resolve the flow and stress profiles up to about $100\,\mu m$ above the wall, which refers to approximately $1.5 - 3$ inner length scales. This high spatial resolution made the results also comparable to a numerical LES study performed by Schanderl and Manhart (2016), and their findings - the magnitude of the wall shear stress depends on the spatial resolution of the velocity measurement close to the wall - were confirmed. Furthermore, bimodal and skewed velocity distributions in the region of the main vortex V1, as reported by Devenport and Simpson (1990), Kirkil and Constantinescu (2015), Paik et al.

(2007), could be resolved and their footprints in the third and fourth order central moments were discussed.

Prospective research on SPE evaluations may lead in several directions. One important issue is the noise level and its reduction. Therefore, spatial correlation function averaging might be a solution. In this work it was shown that averaging five correlation functions in streamwise direction already reduces the scatter of the results. Scharnowski et al. (2012) also state that they improved their results in the experimental case by applying a weighted average of correlation functions before the evaluation. So the question arises, how the averaging should be performed to lose as little information as possible.

Considering the transport equation of turbulent kinetic energy, every term except the pressure and viscous transport as well as the dissipation can be estimated by the introduced method up to single pixel resolution. Since PIV determines the average velocity of particles it is in general not able to measure the pressure. But in contrast to SPE the classical PIV approach is able to determine instantaneous values and thus the terms contained in the dissipation $\epsilon = \nu_{fluid} \left(\langle \frac{\partial v_i'}{\partial x_j} \frac{\partial v_i'}{\partial x_j} \rangle + \langle \frac{\partial v_i'}{\partial x_j} \frac{\partial v_j'}{\partial x_i} \rangle \right)$. It has to be reconsidered if there is a possibility to determine these time-averaged gradients of the instantaneous fluctuations, since they somehow will be stored in the velocity JPDFs, which resemble a footprint of the velocities. Then SPE would be able to resolve all terms that the classical PIV approach is able to resolve, but with a higher spatial resolution.

Moreover, the introduced method can be implemented to quickly provide information on the flow and thus support the user in choosing the best settings, as the main influencing factor on the accuracy of the determined result is the user, *who selects the evaluation parameters based on the knowledge, experience and intuition* (Kähler et al., 2016, §10). Since every window correlation function determined in the standard PIV approach can be considered the ensemble averaged correlation function within the interrogation window, this function or a small ensemble mean of several image pairs can also be evaluated by the proposed method and thus provide information on regions of strong shear and non-Gaussian shaped correlation functions. This information can then help the user to either adapt the settings of the classical PIV evaluation or apply a different method like SPE or PTV if appropriate.

Bibliography

R. Adrian and J. Westerweel. *Particle Image Velocimetry*. Cambridge University Press, 2010. ISBN 0521440084.

R. Adrian and C.-S. Yao. Pulsed laser technique application to liquid and gaseous flows and the scattering power of seed materials. *Applied Optics*, 24(1):44–52, Jan 1985.

R. J. Adrian. Double Exposure, Multiple-Field Particle Image Velocimetry for Turbulent Probability Density. *Optics and Lasers in Engineering*, 9:211–228, 1988.

R. J. Adrian. Particle-imaging techniques for experimental fluid mechanics. *Annual Review of Fluid Mechanics*, 23:261–304, 1991.

R. J. Adrian. Statistical properties of particle image velocimetry measurements in turbulent flow. *SPIE MILESTONE SERIES MS*, 99:191–191, 1994.

P. Alfaya. Influence of a top plate on the flow around a wall-mounted cylinder. Master thesis, Technische Universität München, 2016.

N. Apsilidis, P. Diplas, C. L. Dancey, and P. Bouratsis. Time-resolved flow dynamics and Reynolds number effects at a wall-cylinder junction. *Journal of Fluid Mechanics*, 776: 475–511, 008 2015.

F. Avallone, S. Discetti, T. Astarita, and G. Cardone. Convergence enhancement of single-pixel PIV with symmetric double correlation. *Experiments in Fluids*, 56(4), Mar 2015. ISSN 1432-1114.

F. Billy, L. David, and G. Pineau. Single pixel resolution correlation applied to unsteady flow measurements. *Measurement Science and Technology*, 15(6):1039, 2004.

P. Burt, Y. Chisung, and X. Xinping. Local Correlation Measures for Motion Analysis, A Comparative Study. In *Proceedings IEEE Computer Society: Conference on Pattern Recognition and Image Processing*, pages 269–274. IEEE, 1982.

S. Chakraborty. Some applications of Dirac's Delta function in statistics for more than one random variable. *Applications and Applied Mathematics*, 3(1):42–54, 2008.

H.-S. Chuang, L. Gui, and S. T. Wereley. Nano-resolution flow measurement based on single pixel evaluation PIV. *Microfluidics and Nanofluidics*, 13(1):49–64, 2012.

R. Clift, J. R. Grace, and M. E. Weber. *Bubbles, drops and particles*. Dover Publications Inc., 2005.

B. Dargahi. The turbulent flow field around a circular cylinder. *Experiments in Fluids*, 8 (1):1–12, 1989. ISSN 1432-1114.

E. Delnoij, J. Westerweel, N. Deen, J. Kuipers, and W. van Swaaij. Ensemble correlation PIV applied to bubble plumes rising in a bubble column. *Chemical Engineering Science*, 54(21):5159–5171, 1999.

W. Devenport and R. Simpson. Time-dependent and time-averaged turbulence structure near the nose of a wing-body junction. *Journal of Fluid Mechanics*, 210:23–55, 1990.

C. Escauriaza and F. Sotiropoulus. Reynolds Number EEffect on the Coherent Dynamics of the Turbulent Horseshoe Vortex System. *Flow Turbulence and Combustion*, 86:231–262, 2011.

L. Fahrmeir, R. Künstler, I. Pigeot, and G. Tutz. *Statistik*. Springer, 2004.

A. M. Fincham and G. R. Spedding. Low cost, high resolution DPIV for measurement of turbulent fluid flow. *Experiments in Fluids*, 23(6):449, Dec. 1997. ISSN 1432-1114.

G. Flierl and R. Ferrari. 12.820 Turbulence in the Ocean and Atmosphere. Massachusetts Institute of Technology: MIT OpenCourseWare, https://ocw.mit.edu. License: Creative Commons BY-NC-SA., Spring 2007.

U. Frisch. *Turbulence: The Legacy of A. N. Kolmogorov*. Cambridge Univ Press, 1995.

L. Gui and J. Seiner. An improvement in the nine-point central difference image correction method for digital particle image velocimetry recording evaluation. *Measurement Science and Technology*, 15(10):1958, 2004.

R. Hain, C. J. Kähler, and C. Tropea. Comparison of CCD, CMOS and intensified cameras. *Experiments in Fluids*, 42(3):403, Mar. 2007.

Y. A. Hassan and E. Dominguez-Ontiveros. Flow visualization in a pebble bed reactor experiment using {PIV} and refractive index matching techniques. *Nuclear Engineering and Design*, 238(11):3080–3085, 2008. HTR-2006: 3rd International Topical Meeting on High Temperature Reactor Technology.

V. Hohreiter, S. Wereley, M. Olsen, and J. Chung. Cross-correlation analysis for temperature measurement. *Measurement Science and Technology*, 13(7):1072, 2002.

M. Honkanen and H. Nobach. Background extraction from double-frame PIV images. *Experiments in Fluids*, 38(3):348–362, Feb 2005. ISSN 1432-1114.

S. G. Huisman, S. Scharnowski, C. Cierpka, C. J. Kaehler, D. Lohse, and C. Sun. Logarithmic Boundary Layers in Strong Taylor-Couette Turbulence. *PHYSICAL REVIEW LETTERS*, 110(26), JUN 26 2013.

D. Imhof. *Risk assessment of existing bridge structures*. PhD thesis, University of Cambridge, 2004.

U. Jenssen, W. Schanderl, and M. Manhart. Cylinder wall junction flow: Particle Image Velocimetry and Large Eddy Simulation. In *11th International ERCOFTAC Symposium on Engineering Turbulence Modelling and Measurements*, 2016a.

U. Jenssen, C. Strobl, and M. Manhart. High resolution Particle Image Velocimetry near-wall measurements of non-equilibrium flow at a wall-mounted cylinder. In *11th European Fluid Mechanics Conference*, 2016b.

C. Kähler and U. Scholz. Fernmikroskopische PIV Messungen in makroskopischen Transschallströmungen. In *Fachtagung "Lasermethoden in der Strömungsmesstechnik", 5.-7. September 2006, Braunschweig*, 2006.

C. Kähler, U. Scholz, and J. Ortmanns. Wall-shear-stress and near-wall turbulence measurements up to single pixel resolution by means of long-distance micro-PIV. *Experiments in Fluids*, 41(2):327–341, 2006.

C. Kähler, S. Scharnowski, and C. Cierpka. On the uncertainty of digital PIV and PTV near walls. *Experiments in Fluids*, 52(6):1641–1656, 2012a.

C. J. Kähler, S. Scharnowski, and C. Cierpka. On the resolution limit of digital particle image velocimetry. *Experiments in Fluids*, 52(6):1629, June 2012b.

C. J. Kähler, T. Astarita, P. P. Vlachos, J. Sakakibara, R. Hain, S. Discetti, R. La Foy, and C. Cierpka. Main results of the 4th International PIV Challenge. *Experiments in Fluids*, 57(6):1–71, 2016. ISSN 1432-1114.

M. N. Karchevskiy, M. P. Tokarev, A. A. Yagodnitsyna, and L. A. Kozinkin. Correlation algorithm for computing the velocity fields in microchannel flows with high resolution. *Thermophysics and Aeromechanics*, 22(6):745–754, 2015.

R. D. Keane and R. J. Adrian. Optimization of particle image velocimeters. I. Double pulsed systems. *Measurement Science and Technology*, 1(11):1202, 1990.

R. D. Keane and R. J. Adrian. Theory of cross-correlation analysis of PIV images. *Applied Scientific Research*, 49(3):191–215, 1992.

G. Kirkil and G. Constantinescu. Effect of cylinder Reynolds number on the turbulent horseshoe vortex system and near wake of a surface-mounted circular cylinder. *Physics of Fluids*, 27, 2015.

P. Kundu and I. Cohen. *Fluid Mechanics*. Elsevier, 3 edition, 2004.

M. Löffler-Mang. *Optische Sensorik*. Vieweg+Teubner, 2012.

L. Lourenco and A. Krothapalli. On the accuracy of velocity and vorticity measurements with PIV. *Experiments in Fluids*, 18(6):421–428, 1995.

L. B. Lucy. An iterative technique for the rectification of observed distributions. *The Astronomical Journal*, 79:745–754, 1974. doi: 10.1086/111605.

C. Meinhart, S. Wereley, and J. Santiago. A PIV algorithm for estimating time-averaged velocity fields. *Journal of Fluids Engineering*, 122:285–289, 2000.

C. D. Meinhart, S. T. Wereley, and J. G. Santiago. PIV measurements of a microchannel flow. *Experiments in Fluids*, 27(5):414–419, 1999.

B. Melville and A. Raudkivi. Flow Characteristics in Local Scour at Bridge Piers. *Journal of Hydraulic Research*, 15(4), 1977.

M. G. Olsen and R. J. Adrian. Brownian motion and correlation in particle image velocimetry. *Optics & Laser Technology*, 32(7):621–627, 2000.

N. Otsu. Threshold Selection Method from Gray-Level Histograms. *IEEE Transactions on Systems Man and Cybernetics*, 9(1):62–66, 1979.

J. Paik, C. Escauriaza, and F. Sotiropoulus. On the bimodal dynamics of the turbulent horseshoe vortex system in a wing-body junction. *Physics of Fluids*, 19, 2007.

F. Pfleger. *Experimentelle Untersuchung der Auskolkung um einen zylindrischen Br ückenpfeiler*. PhD thesis, Technische Universtit ät M ünchen, 2011.

S. B. Pope. *Turbulent Flows*. Cambridge University Press, 2001.

A. Prasad, R. J. Adrian, C. Landreth, and P. Offutt. Effect of resolution on the speed and accuracy of particle image velocimetry interrogation. *Experiments in Fluids*, 13(2-3): 105–116, 1992.

M. Raffel, C. Willert, S. Wereley, and J. Kompenhans. *Particle Image Velocimetry*. Springer-Verlag GmbH, 2 edition, 2007.

O. Reynolds. On the dynamical theory of incompressible viscous fluids and the determination of the criterion. *Philosophical T*, 186:123–164, 1895.

W. H. Richardson. Bayesian-Based Iterative Method of Image Restoration∗. *Journal of the Optical Society of America*, 62(1):55–59, Jan 1972.

A. Roulund, B. M. Sumer, J. FredsØe, and J. Michelsen. Numerical and experimental investigation of flow and scour around a circular pile. *Journal of Fluid Mechanics*, 534: 351–401, 07 2005.

J. G. Santiago, S. T. Wereley, C. D. Meinhart, D. Beebe, and R. J. Adrian. A particle image velocimetry system for microfluidics. *Experiments in Fluids*, 25(4):316–319, 1998.

F. Scarano. Iterative image deformation methods in PIV. *Measurement Science and Technology*, 13(1), 2002.

W. Schanderl and M. Manhart. Non-equilibrium near wall velocity profiles in the flow around a cylinder mounted on a flat plate. In *15th European Turbulence Conference*, 2015.

W. Schanderl and M. Manhart. Reliability of wall shear stress estimations of the flow around a wall-mounted cylinder. *Computers and Fluids*, 128:16–29, 2016.

W. Schanderl, U. Jenssen, C. Strobl, and M. Manhart. Turbulence structure in front of a wall-mounted cylinder. Manuscript submitted for publication, 2016.

S. Scharnowski and C. Kähler. Methods for estimating higher order moments from PIV data. In *10th International Symposium on particle image velocimetry - PIV13, Delft, The Netherlands, July 1-3, 2013*, 2013.

S. Scharnowski, R. Hain, and C. J. Kähler. Reynolds stress estimation up to single-pixel resolution using PIV-measurements. *Experiments in Fluids*, 52(4):985–1002, 2012.

J. Soria and C. Willert. On measuring the joint probability density function of three-dimensional velocity components in turbulent flows. *Measurement Science and Technology*, 23(6), 2012.

J. Starck, E. Pantin, and F. Murtagh. Deconvolution in astronomy: A review. *Publications of the Astronomical Society of the Pacific*, 114(800):1051, 2002.

C. Strobl, D. Quosdorf, and M. Manhart. Einflussfaktoren auf PIV Auswertungen mit Single Pixel Ensemble Correlation. In B. Ruck, B. Gromke, K. Klausmann, A. Leder, and D. Dopheide, editors, *Fachtagung "Lasermethoden in der Strömungsmesstechnik", 23. Fachtagung 2015, Dresden*. Deutsche Gesellschaft für Laser-Anemometrie GALA e.V., Deutsche Gesellschaft für Laser-Anemometrie GALA e.V., 2015.

C. Strobl, U. Jenssen, and M. Manhart. Estimating higher order moments from single pixel ensemble correlation PIV. Manuscript submitted for publication, 2016.

R. Theunissen, F. Scarano, and M. L. Riethmuller. On improvement of PIV image interrogation near stationary interfaces. *Experiments in Fluids*, 45:557–572, Oct. 2008.

C. Tropea, A. Yarin, and J. Foss, editors. *Springer Handbook of Experimental Fluid Mechanics*. Springer-Verlag GmbH, 2007.

S. Wereley, C. Meinhart, L. Gui, D. Tretheway, and A. Sud. Single pixel evaluation of microchannel flows. In *ASME. ASME proceedings, Fluids Engineering*, Orlando, Florida, USA, November 5 – 11, 2005 2005a.

S. Wereley, C. Meinhart, D. Tretheway, L. Gui, and A. Sud. Bias and Random Errors in Single Pixel Interrogation. In *6th International Symposium on Particle Image Velocimetry*, pages 1–8, 2005b.

S. T. Wereley and C. D. Meinhart. Second-order accurate particle image velocimetry. *Experiments in Fluids*, 31(3):258–268, 2001.

J. Westerweel. *Particle Image Velocimetry - Theory and Application*. Delft University Press, 1993.

J. Westerweel. Theoretical analysis of the measurement precision in particle image velocimetry. *Experiments in Fluids*, 29(1):S003–S012, 2000.

J. Westerweel, D. Dabiri, and M. Gharib. The effect of a discrete window offset on the accuracy of cross-correlation analysis of digital PIV recordings. *Experiments in fluids*, 23 (1):20–28, 1997.

J. Westerweel, P. F. Geelhoed, and R. Lindken. Single-pixel resolution ensemble correlation for micro-PIV applications. *Experiments in Fluids*, 37(3):375–384, 2004.

C. Willert. Stereoscopic digital particle image velocimetry for application in wind tunnel flows. *Measurement Science and Technology*, 8(12):1465, 1997.

C. Willert. Adaptive PIV processing based on ensemble correlation. In *Proceedings: 14th Intl. Symp. Applic. Laser Techniques to Fluid Mech., Lisbon, Portugal*, pages 07–10, 2008.

C. Xu, Z. Zhang, J. M. den Toonder, and F. Nieuwstadt. Origin of high kurtosis levels in the viscous sublayer. Direct numerical simulation and experiment. *Physics of Fluids (1994-present)*, 8(7):1938–1944, 1996.